The Pennsylvania State University
The Graduate School
College of Engineering

CABLE ACTUATED TENSEGRITY STRUCTURES FOR DEPLOYABLE SPACE BOOMS WITH ENHANCED STIFFNESS

A Dissertation in
Aerospace Engineering
by
Kaan Yildiz

Submitted in Partial Fulfillment
of the Requirements
for the Degree of

Doctor of Philosophy

August 2018

The dissertation of Kaan Yildiz was reviewed and approved[*] by the following:

George A. Lesieutre
Professor of Aerospace Engineering
Associate Dean for Research and Graduate Programs
Dissertation Advisor, Chair of Committee

Joseph P. Cusumano
Professor of Engineering Science and Mechanics

Robert G. Melton
Professor of Aerospace Engineering

Namiko Yamamoto
Assistant Professor of Aerospace Engineering

Amy Pritchett
Professor of Aerospace Engineering
Head of the Department of Aerospace Engineering

[*] Signatures are on file in the Graduate School.

Abstract

Spacecraft having extended configurations must be stowed for launch compactly, with final stiffness adequate to maintain shape and stability under dynamic disturbances. The proposed research focuses on deployable booms, one-dimensional beam-like structures comprising a lightweight, structurally-efficient assemblage of finer-scale structural members. In particular, tensegrity structures are considered for their potential to provide a new kind of deployable boom for space applications.

Tensegrity structures (or “tensegrities”) comprise a self-equilibrating assemblage of 1-D compression members (struts) and tension members (tendons or cables) connected via frictionless ball joints at member ends (nodes). Tensegrities can also carry external loads very efficiently. In a classical tensegrity structure, struts are connected only to cables; however, in a generalization of the concept, struts can meet at nodes, and can be classified based on the maximum number of struts connected at a single node. A classical tensegrity is thus “Class-1”, and one in which two struts meet at a node would be “Class-2”.

Existing approaches to the analysis and design of tensegrity structures are reviewed, including: various methods of form-finding such as numerical and semi-analytical; as well as methods of force finding (from a given geometry). The behavior of tensegrity structures under external loads is studied using a nonlinear finite element model in which unique characteristics such as the effect of pre-stress and cable slackness are taken into account. Effect of pre-stress is observed as stiffening while cable slackness reduces the overall stiffness. Free vibration properties are investigated, and substantial effects of pre-stress levels on vibration modes associated with infinitesimal mechanisms are revealed. Vibration modes associated with infinitesimal mechanisms are governed by pre-stress levels. The results indicate that corresponding natural frequencies increase proportionally with the square root of the pre-stress levels. Furthermore, effective beam stiffness properties are determined for use in preliminary design; these stiffnesses depend on pre-stress levels. Axial and torsional rigidities are found to increase substantially as pre-stress levels are increased; however, bending and shear rigities do not increase as much as the axial and torsional rigidities.

A primary concern regarding the use of classical tensegrity structures for space applications is inferior stiffness, due mainly to the small cross-sectional areas of tendons. Structural stiffness can be increased by allowing strut-to-strut connections, but this decreases packaging efficiency. Two examples of deployable “cylindrical” tensegrity booms are investigated in detail: one, a Class-1 tensegrity, the three-strut Snelson type configuration, which is also known as “SVD” (Saddle-Vertical-Diagonal) configuration; and the other, a Class-2 tensegrity comprising pairs of mirror-image “triplex” configurations. Strut lengths are fixed, and deployment is achieved conceptually via actuation of cable lengths. Generalization to n-strut cylindrical tensegrities is achieved, and example deployments are simulated.

The primary focus of the dissertation is a concept for a deployable cylindrical tensegrity boom that begins as a Class-1 tensegrity having high packaging efficiency and, through a multi-stage deployment process, ends as a Class-2 tensegrity having higher stiffness. Realizing this structural concept requires consistent connectivity, augmented by additional cable actuation to achieve the transition at an appropriate stage of deployment. An initial physical realization of this concept (configuration and deployment process) is demonstrated. As a result, it is found that axial and torsional rigidities are increased by factors of 4.5 and 3 for the selected tensegrity boom example, respectively. Whereas the improvements in bending and shear rigidities are obtained as 36% and 63%, respectively. Another important benefit of the transformation is also identified as the increase in the total height of the boom.

Sizing and prestress optimization of tensegrity booms, with consideration of member buckling and yielding, are achieved by implementing a heuristic optimization algorithm, Particle Swarm Optimization (PSO). A trade-off study was conducted with the number of bays varied, and its influence on several properties including bending and torsional stiffnesses, mass and stiffness-to-mass ratios is discussed. The results show that the bending stiffness-to-mass ratio of the optimized tensegrity booms are greater than the bending stiffness-to-mass ratio of most of state of the art deployable boom concepts. A multi-stage optimal deployment path in terms of stiffness is also obtained for a selected case by evaluating effective beam stiffness parameters.

The proposed deployment strategy involving a transformation between Class-1 to Class-2 tensegrities promises significant improvements in the structural efficiency of deployable tensegrity booms. The final stiffness-to-mass ratio is found to be greater compared to state of the art deployable boom concepts. This deployment strategy has the potential to increase the claims on tensegrity structures to be one of the best candidates for deployable structures. Alongside parallel advances in cable actuation, tensegrity structures can replace the conventional deployable structures in real space missions.

Table of Contents

List of Figures viii

List of Tables xiv

List of Symbols xv

Acknowledgments xviii

Chapter 1
Introduction 1
1.1 Deployable Booms 2
1.1.1 Thin-Walled Tubular Booms 3
1.1.2 Telescopic Boom 4
1.1.3 Coilable Booms 4
1.1.4 Articulated Trusses 5
1.2 Tensegrity Structures for Space Applications 6

Chapter 2
Mechanics of Tensegrity Structures 9
2.1 Equilibrium Equations 10
2.1.1 Rank Deficiency Conditions 14
2.1.2 Static and Kinematic Indeterminacy 15
2.2 Form Finding 16
2.2.1 Numerical Form-Finding 19
2.2.2 Semi-Analytical Form Finding 23
2.3 Force Finding 27

Chapter 3
Static and Dynamic Analyses of Tensegrity Structures 34
3.1 Nonlinear Finite Element Model 37

3.2 Static Analyses Under External Loads 44
3.3 Free Vibration Problem 50
3.4 Effective Stiffness Properties of Tensegrity Booms 52
    3.4.1 Energy Equivalency Method 53
    3.4.2 Modified Energy Equivalency Method 58
    3.4.3 Nonlinear Finite Element Validation 65

Chapter 4
Deployment of Cylindrical Tensegrity Booms **70**
4.1 Deployment of Class-1 Tensegrity Booms 71
    4.1.1 Deployment of n-strut Class-1 Tensegrity Booms 78
4.2 Deployment of Class-2 Tensegrity Booms 84
    4.2.1 Deployment of n-strut Class-2 Tensegrity Booms 92

Chapter 5
A Novel Deployment Strategy Involving Transformation **99**
5.1 Deployment Simulations 101
5.2 Stiffness Comparison 109

Chapter 6
Optimization of Tensegrity Booms **117**
6.1 Particle Swarm Optimization 119
6.2 Sizing and Pre-stress Optimization of Deployed Tensegrity Booms . 122
6.3 Optimization of Deployment/Transformation Path 130

Chapter 7
Conclusions and Future Work **147**
7.1 Future Work 149

Appendix A
Optimization of Deployment Path for 8 bays, R=0.254 m **152**

Appendix B
Optimization Results, R=0.56 m **158**

Appendix C
MATLAB Codes **167**

Bibliography **168**

List of Figures

1.1 Storable Tubular Extendible Member [1] 3
1.2 Collapsible Tubular Mast [1] 4
1.3 Telescopic Boom [3] 4
1.4 Coilable boom [1] 5
1.5 Articulated boom [2] 6
1.6 The first tensegrity structure by Snelson, X-Piece [12] 7

2.1 Force balance at a node 11
2.2 Three-Strut Cylindrical Tensegrity “Triplex” 18
2.3 Triplex Top View 19
2.4 Triplex Side View 19
2.5 First set of force-densities: Top view 26
2.6 First set of force-densities: Side view 26
2.7 Second set of force-densities: Top view 27
2.8 Second set of force-densities: Side view 27
2.9 Two Stage Triplex Boom 30
2.10 Two Stage Triplex Boom: Top View 31
2.11 Two Stage Triplex Boom: Side View 31

3.1 Two Noded Space Truss Element 38
3.2 Four-Strut Tensegrity Unit - Quadruplex 47
3.3 Behavior of the quadruplex unit under traction and compression . . 49
3.4 Triplex Unit 51
3.5 First mode 52
3.6 Second mode 52
3.7 Fourth mode 52
3.8 Sixth mode 52
3.9 Axes shown on a long boom 55
3.10 Two Stage Three-Strut Tensegrity Boom 63
3.11 Two Stage Four-Strut Tensegrity Boom 63

3.12 Two Stage Five-Strut Tensegrity Boom 63
3.13 Two Stage Six-Strut Tensegrity Boom 63
3.14 Variation of axial rigidity 64
3.15 Variation of bending rigidity 64
3.16 Variation of shear rigidity 64
3.17 Variation of torsional rigidity 64
3.18 Comparison of results for axial rigidity 68
3.19 Comparison of results for bending rigidity 68
3.20 Comparison of results for shear rigidity 68
3.21 Comparison of results for torsional rigidity 68

4.1 Three-strut Snelson type tensegrity 72
4.2 SVD Side view 72
4.3 SVD Top view 72
4.4 Equilibrium surface in terms of overlap 75
4.5 Equilibrium surface in terms of total height 76
4.6 Deployment path of SVD 76
4.7 Deployment sequence, 1/4 77
4.8 Deployment sequence, 2/4 77
4.9 Deployment sequence, 3/4 77
4.10 Deployment sequence, 4/4 77
4.11 Variation of the lengths 78
4.12 Variation of the force-densities 78
4.13 Connectivity chart for Class-1 tensregrity booms 80
4.14 Equilibrium surface of four-strut SVD in terms of overlap 82
4.15 Equilibrium surface of four-strut SVD in terms of height 82
4.16 Deployment sequence, 1/4 83
4.17 Deployment sequence, 2/4 83
4.18 Deployment sequence, 3/4 83
4.19 Deployment sequence, 4/4 83
4.20 Variation of the lengths 84
4.21 Variation of the force-densities 84
4.22 Two stage, three-strut Class-2 cylindrical tensegrity boom 85
4.23 Class-2 tensegrity boom, Top view 85
4.24 Class-2 tensegrity boom, Side view 85
4.25 Illustration of α, γ, r_{base} and r 87
4.26 The relationship between α and h 88
4.27 Deployment sequence, 1/4 89
4.28 Deployment sequence, 2/4 89
4.29 Deployment sequence, 3/4 89

4.30 Deployment sequence, 4/4 89
4.31 Variation of the lengths 89
4.32 Variation of the force-densities 89
4.33 Deployment sequence, 1/4 91
4.34 Deployment sequence, 2/4 91
4.35 Deployment sequence, 3/4 91
4.36 Deployment sequence, 4/4 91
4.37 Variation of the lengths 91
4.38 Variation of the force-densities 91
4.39 Connectivity chart for Class-2 tensegrity booms 94
4.40 The relationship between α and h, n=4 95
4.41 Deployment sequence, 1/4 96
4.42 Deployment sequence, 2/4 96
4.43 Deployment sequence, 3/4 96
4.44 Deployment sequence, 4/4 96
4.45 Variation of the lengths 96
4.46 Variation of the force-densities 96
4.47 Deployment sequence, 1/4 97
4.48 Deployment sequence, 2/4 97
4.49 Deployment sequence, 3/4 98
4.50 Deployment sequence, 4/4 98
4.51 Variation of the lengths 98
4.52 Variation of the force-densities 98

5.1 Three-strut SVD tensegrity boom 100
5.2 Three-strut Class-2 tensegrity boom 100
5.3 Equilibrium surface in terms of overlap 101
5.4 Equilibrium surface in terms of total height 101
5.5 Initial deployment path on the equilibrium surface 102
5.6 Initial deployment, 1/4 103
5.7 Initial deployment, 2/4 103
5.8 Initial deployment, 3/4 103
5.9 Initial deployment, 4/4 103
5.10 Variation of the lengths 103
5.11 Variation of the force-densities 103
5.12 Activation of the reinforcing cables 104
5.13 Rotation Phase, 1/4 104
5.14 Rotation Phase, 2/4 104
5.15 Rotation Phase, 3/4 105
5.16 Rotation Phase, 4/4 105

5.17 Variation of the lengths 105
5.18 Variation of the force-densities 105
5.19 Transition Phase, 1/4 106
5.20 Transition Phase, 2/4 106
5.21 Transition Phase, 3/4 106
5.22 Transition Phase, 4/4 106
5.23 Variation of the lengths 107
5.24 Variation of the force-densities 107
5.25 Transformed Class-2 tensegrity boom 108
5.26 Final Deployment, 1/4 108
5.27 Final Deployment, 2/4 108
5.28 Final Deployment, 3/4 108
5.29 Final Deployment, 4/4 108
5.30 Variation of the lengths 109
5.31 Variation of the force-densities 109
5.32 Class-1 Deployment, 1/4 110
5.33 Class-1 Deployment, 2/4 110
5.34 Class-1 Deployment, 3/4 110
5.35 Class-1 Deployment, 4/4 110
5.36 Variation of the lengths 111
5.37 Variation of the force-densities 111
5.38 Top plane of the tensegrity booms showing the loading conditions . 111
5.39 Fully Deployed SVD Initial Configuration 113
5.40 Transformed Class-2 Initial Configuration 113
5.41 Fully Deployed SVD y Bending, 250 N 114
5.42 Transformed Class-2 y Bending, 250 N 114
5.43 Fully Deployed SVD y Bending, 500 N 114
5.44 Transformed Class-2 y Bending, 500 N 114
5.45 Fully Deployed SVD x Bending, 250 N 114
5.46 Transformed Class-2 x Bending, 250 N 114
5.47 Fully Deployed SVD x Bending, 500 N 115
5.48 Transformed Class-2 x Bending, 500 N 115

6.1 Movement of a particle in a two-dimensional search space 120
6.2 45-bar truss bridge 122
6.3 Variation of bending stiffness 126
6.4 Variation of bending stiffness per unit mass 126
6.5 Variation of torsional stiffness 126
6.6 Variation of torsional stiffness per unit mass 126
6.7 Variation of mass 127

6.8 Variation of tip deflection 127
6.9 Variation of length of struts 127
6.10 Equilibrium surface with respect to overlap 133
6.11 Equilibrium surface with respect to height 133
6.12 Feasible points on equilibrium surface with respect to overlap 134
6.13 Feasible points on equilibrium surface with respect to height 134
6.14 Equilibrium surface with respect to axial rigidity 135
6.15 Equilibrium surface with respect to bending rigidity 135
6.16 Equilibrium surface with respect to shear rigidity 136
6.17 Equilibrium surface with respect to torsional rigidity 136
6.18 Optimized deployment path 137
6.19 Initial deployment, 1/4 138
6.20 Initial deployment, 2/4 138
6.21 Initial deployment, 3/4 138
6.22 Initial deployment, 4/4 138
6.23 Variation of the lengths 138
6.24 Variation of the force-densities 138
6.25 Activation of reinforcing cables 139
6.26 Rotation Phase, 1/4 139
6.27 Rotation Phase, 2/4 139
6.28 Rotation Phase, 3/4 140
6.29 Rotation Phase, 4/4 140
6.30 Variation of the lengths 140
6.31 Variation of the force-densities 140
6.32 Transformation Phase, 1/4 141
6.33 Transformation Phase, 2/4 141
6.34 Transformation Phase, 3/4 141
6.35 Transformation Phase, 4/4 141
6.36 Variation of the lengths 141
6.37 Variation of the force-densities 141
6.38 Transformed Class-2 tensegrity boom 142
6.39 Final Deployment, 1/4 143
6.40 Final Deployment, 2/4 143
6.41 Final Deployment, 3/4 143
6.42 Final Deployment, 4/4 143
6.43 Variation of the lengths 143
6.44 Variation of the force-densities 143

A.1 Equilibrium surface with respect to overlap 152
A.2 Equilibrium surface with respect to height 153

A.3 Feasible points on equilibrium surface with respect to overlap 153
A.4 Feasible points on equilibrium surface with respect to height 154
A.5 Equilibrium surface with respect to axial rigidity 154
A.6 Equilibrium surface with respect to bending rigidity 155
A.7 Equilibrium surface with respect to shear rigidity 155
A.8 Equilibrium surface with respect to torsional rigidity 156

B.1 Variation of bending stiffness 158
B.2 Variation of bending stiffness per unit mass 158
B.3 Variation of torsional stiffness 159
B.4 Variation of torsional stiffness per unit mass 159
B.5 Variation of mass 159
B.6 Variation of tip deflection 159
B.7 Variation of length of struts 159
B.8 Equilibrium surface with respect to overlap 162
B.9 Equilibrium surface with respect to height 162
B.10 Feasible points on equilibrium surface with respect to overlap 163
B.11 Feasible points on equilibrium surface with respect to height 163
B.12 Equilibrium surface with respect to axial rigidity 164
B.13 Equilibrium surface with respect to bending rigidity 164
B.14 Equilibrium surface with respect to shear rigidity 165
B.15 Equilibrium surface with respect to torsional rigidity 165

List of Tables

3.1 Node locations 48
3.2 Element Connectivity and Properties 48
3.3 Natural Frequencies of Triplex Unit 51
3.4 Pre-stress values in the elements 63

4.1 Location of the nodes in a two stage cylindrical Class-1 boom . . . 79
4.2 Nodal locations of two stage, three-strut Class-2 cylindrical tensegrity boom 86
4.3 Node locations of a two stage cylindrical Class-2 tensegrity boom . 93

5.1 Pre-stress in each type of element 112
5.2 Deflection comparison of SVD and Class-2 booms 112
5.3 Effective stiffness properties of the tensegrity booms 116

6.1 Optimal cross sectional areas (in^2) for the truss design example . . 123
6.2 Bending and torsional stiffnesses of optimized booms 128
6.3 Optimized design variables for tensegrity booms 129
6.4 Packaging properties of optimized booms 131
6.5 Maximum length, force, stress and total mass data 144
6.6 Comparsion of different deployable boom concepts 145

A.1 Maximum length, force, stress and total mass data 156

B.1 Bending and torsional stiffnesses of optimized booms 160
B.2 Optimized design variables for tensegrity booms 161
B.3 Maximum length, force, stress and total mass data 166

List of Symbols

Symbols

A	Cross-sectional area
$\mathbf{A}$	Equilibrium matrix
c_{ij}	Coupling terms
$\mathbf{C}$	Connectivity matrix
D	Length of diagonal cables
$\mathbf{D}$	Force-density matrix
E	Modulus of elasticity
EA	Axial rigidity
EI	Bending rigidity
$\mathbf{F}$	Internal force vector
GA	Shear rigidity
GJ	Torsional rigidity
h	Overlap between two stages
$\mathbf{K}_L$	Linear stiffness matrix
$\mathbf{K}_{NL}$	Geometric stiffness matrix
$\mathbf{K}_T$	Tangent stiffness matrix

$\mathbf{K}^*$	Stiffness matrix of the equivalent continuum beam
l_b	Length of struts
L	Length of the continuum beam
L_0	Rest length of elements
m	Number of elements
$\mathbf{M}$	Mass matrix
n	Number of nodes
n_s	Number of state of self-stress
n_m	Number of mechanisms
P_{eu}	Euler buckling load
P_s	Pre-stress coefficient
$\mathbf{P}$	External force vector
q	Force-density
$\mathbf{q}$	Force-density vector
r	Radius of circumscribing circles of intermediate plane
r_{base}	Radius of circumscribing circles of bottom and top plane
R	Length of reinforcing cables
S	Length of saddle cables
$\mathbf{T}$	Transformation matrix
U	Strain energy
$\mathbf{U}$	Nodal coordinates
$\Delta\mathbf{U}$	Nodal displacements in each iteration
V	Length of vertical cables
α	Twist angle

α_{ij}	Azimuth angle of the strut between nodes i and j
δ_{ij}	Declination angle of the strut between nodes i and j
ρ	Density
σ_{cr}	Critical stress for wall buckling
ω	Angular frequency

Acronyms

ABC	Artificial Bee Colony
PSO	Particle Swarm Optimization
SVD	Saddle-Vertical-Diagonal Configuration

Acknowledgments

First and foremost, I would like to gratefully thank my advisor, Dr. George A. Lesieutre for his continuous support, guidance and never-ending encouragement during my doctoral studies at Penn State. He introduced me to tensegrity structures, and without his interest, understanding and feedback, this dissertation would not have been possible. The regular meetings we had, broadened my way of thinking and they will be missed.

I also would like to thank my doctoral committee members, Dr. Joseph P. Cusumano, Dr. Robert G. Melton and Dr. Namiko Yamamoto for their valuable suggestions and comments. I also gratefully acknowledge the financial support of TUBITAK - BIDEB 2213 scholarship for my doctoral studies.

During my graduate studies at Penn State, I have experienced many difficulties and I am grateful to have my friends who helped me along the way and cheered me up. Especially, I would like to thank my roommates Evren Yenigelen and Zulkuf Yavuz for always being there for me. I also wish to thank Dr. Seher Eken who encouraged and inspired me.

Most importantly, I would like to thank my parents Fatma and Kamuran Yildiz for everything since the beginning of my life. Their priceless love and continuous support made me who I am. Last but not least, I would like to thank my fiancée Yeliz Saka for believing in, supporting and actually, waiting for me. She was always there for me and helped me get over any difficulties I experienced.

Kaan Yildiz
University Park, Pennsylvania
August, 2018

Dedication

to my parents and fiancée...

Chapter 1 Introduction

One of the most important challenges in launching a spacecraft is to deal with heavy payloads and large volumes. The capability of putting big structures into orbit is highly limited by their weight and shapes due to current rocket technology. In order to address the volume challenge, deployable structures have been used widely in space applications and missions for several decades. However, even though structural systems adapted for launch can be stowed into smaller volumes and then deployed, the payload weight remains limited by current rocket technology. Therefore, development of a new deployable structural system for space applications that is efficient in terms of weight and stiffness could decrease the weight of the structure, resulting in reduced fuel requirements for space missions. In this work, tensegrity structures for space applications as deployable booms are considered.

Tensegrity structures emerged as an architectural concept in the 1950s and over time have found applications and explanatory power within various fields of engineering and science. From an engineering point of view, they can be defined as pre-stressed, pin-jointed structural systems. They are composed solely of axial load-carrying members - each of which carries either tension or compression - connected to each other via ideal ball joints. By definition, the struts are discontinuous, and the structural integrity and stability are maintained by pre-stress introduced in cables. The members do not experience bending loads individually, and the structure bends as a whole.

Tensegrity structures are proposed to be great candidates for deployable structures by many researchers. Therefore, in this dissertation, a method has been proposed to design and deploy tensegrity structures for space applications. The method proposed here develops an innovative and adaptive tensegrity structure that can adjust to different environments by exhibiting high stiffness or high packing density when required.

In this chapter, state-of-the-art of deployable boom concepts are reviewed, and applications of tensegrity structures for space missions are investigated.

1.1 Deployable Booms

One of the oldest known examples of a deployable structure is the umbrella. It is transformed to an operational configuration to provide shelter from rain when desired and stowed into a compact volume for transportation purposes. Retractable roofs, tents, folding chairs, deployable bridges, and portable structures for shelters are other common examples of deployable structures.

The essential feature of a deployable structure is ease of storage for transportation. The requirements may vary based on application; however, deployability and retractibility are typically standard except in some applications in which permanent deployment is acceptable. Regarding space applications, the deployment process should be autonomous and reliable in order to avoid any malfunctions that can threaten the mission.

The first applications of deployable space structures were developed to stabilize spacecraft using long deployable booms (gravity-gradient stabilization). In this way, the orientation of the spacecraft could be controlled passively, and communication between the spacecraft and the ground station located on Earth could be maintained using antennas. As more complex and larger spacecraft were developed, more powerful and reliable deployable structures were needed. Deployable structures find many applications in the aerospace industry; a few examples are large solar arrays, communication reflectors, telescopes, solar sails, etc. [1–3]. Researchers continue to pursue less complex and more reliable deployable space structures.

Deployable booms are structures that deploy in one dimension. They are mostly used to isolate electronic components to reduce interference between the spacecraft and the scientific instruments or to support other structures [1]. Other applications include communication antennas, gravity-gradient stabilization, and actuation of deployment and retraction of solar arrays [3].

Deployable booms are generally classified into four different groups: thin-walled tubular booms, telescopic booms, coilable booms, and articulated trusses [4]. A few review papers on deployable booms can be found in the literature [3–5].

1.1.1 Thin-Walled Tubular Booms

Thin-walled tubular booms were one of the first developed deployable boom concepts that can be deployed and retracted. They take advantage of elastic deformation capabilities of thin-walled shells.

The earliest member of the family of thin-walled tubular booms is the *Storable Tubular Extendible Member* (STEM), which was developed in Canada in the 1960s [6]. It provides a substantial axial stiffness; however, due to its open cross-section, it exhibits low torsional stiffness. The *Collapsible Tubular Mast* (CTM), developed by the German Aerospace Center (DLR), consists of two STEMs bonded at the edges, thus closing the cross-section. As a result, it provides better torsional stiffness than STEMs. They have been used in various space missions [2]. These two deployable boom example concepts are shown in Figures 1.1 and 1.2.

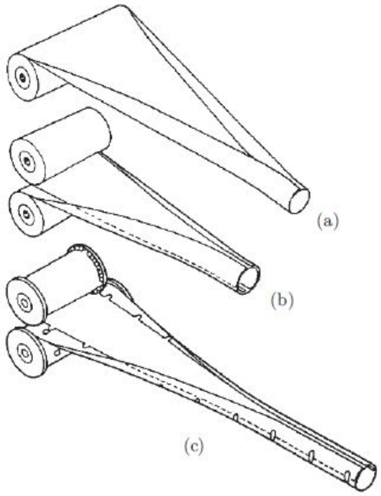

Figure 1.1: Storable Tubular Extendible Member [1]

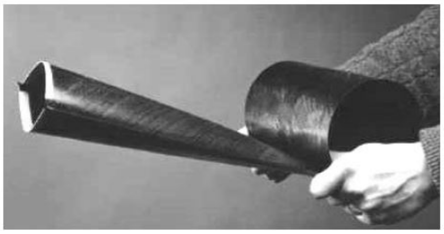

Figure 1.2: Collapsible Tubular Mast [1]

1.1.2 Telescopic Boom

Telescopic booms are made of thin-walled cylindrical tubes by placing one inside another. They can be deployed either sequentially or synchronously. Their limitations are due to tube thickness and overlap length [1].

A motor located at the bottom controls a spindle that drives the deployment of the booms as shown in Figure 1.3. Each nut located in a tube engages with the spindle and is being forced to move outwards until it reaches the end of the spindle.

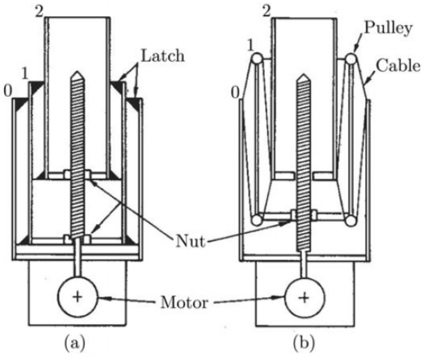

Figure 1.3: Telescopic Boom [3]

1.1.3 Coilable Booms

The first coilable boom was developed in 1967 by H. R. Mauch [7]. The coilable boom is a lattice truss that consists of a number of parallel rods, called longerons, lateral battens and bracing cables [2]. The battens are designed in such a way that they always carry compression, pre-stressing the structure. They are mostly designed to have a triangular cross-section and are stowed by coiling the longerons as shown in Figure 1.4.

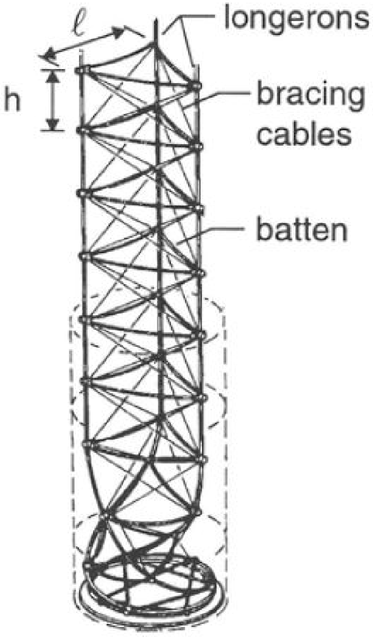

Figure 1.4: Coilable boom [1]

Deployment of coilable booms can be achieved by two distinct strategies. The first option uses an axial cable for restraining the deployment rate where the deployment is driven by the stored elastic energy in the structure. During deployment, the tip of the structure rotates and it does not exhibit full stiffness until the deployment is completely executed. The second option utilizes a canister and a motor for controlling the deployment. As the deployment occurs, the portion of the structure that leaves the canister has already been rotated and therefore its full stiffness is acquired. Coilable deployable booms are very efficient in terms of packing as they can be stowed into 2-3% of their deployed lengths [1].

1.1.4 Articulated Trusses

Articulated trusses have found many applications as deployable space structures. They offer the highest stiffness among the four groups in addition to their efficiency and accuracy. They consist of longerons, battens and diagonals. The longerons are connected to each other with revolute hinges, and pre-stressed diagonal cables are placed at the faces of each bay. The deployment is generally driven by the strain energy stored in the structure during folding. One of the main advantages they have is constant diameter during deployment. As the deployment occurs, each bay maintains its full strength as they leave the protective canister.

The most notable example of articulated trusses that have flown to space is the *Able Deployable Articulated Mast* (ADAM). It has been developed for space missions that require very long and stiff booms. A 60 m long ADAM flew into orbit for NASA's *Shuttle Radar Topography Mission* (SRTM). Figure 1.5 shows an articulated truss example [2].

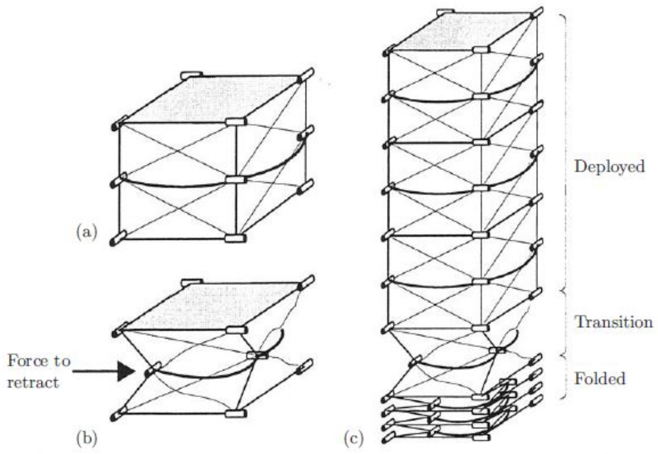

Figure 1.5: Articulated boom [2]

1.2 Tensegrity Structures for Space Applications

Tensegrity structures emerged as an architectural concept in the 1950s as a result of a collaborative work of the artist Kenneth Snelson and the famous architect Buckminster Fuller. The very first definition was made by Fuller [8] as "an assemblage of tension and compression components arranged in a discontinuous compression system". The name tensegrity is a combination of words *tensile* and *integrity*, coined by Buckminster Fuller. A long-continuing debate was settled recently, and credit was given to Kenneth Snelson for his invention [9–11]. Figure 1.6 shows the first tensegrity structure built by Snelson.

Figure 1.6: The first tensegrity structure by Snelson, X-Piece [12]

Over the years tensegrity structures have been considered in many fields besides architecture and art. Mathematics, civil engineering, biology, and science are a few examples of application fields. Motro [13] claims that tensegrity structures are the “structural systems for the future”.

From an engineering perspective, tensegrity structures are pre-stressed, pin-jointed structural systems. They consist of axial load-carrying members, each of which carries either tension or compression, connected to each other with frictionless ball joints. Tension- and compression- carrying members are called cables and struts, respectively, and pretension is applied to these members in order to stabilize the structure and satisfy self-equilibrium. Since the members carry only pure axial loads, none of them experience bending moments, resulting in extremely rigid structures relative to their mass. Additionally, compressive elements are mostly discontinuous, and thus complex joints are avoided. As a result, the structure can be folded and stowed into compact volumes.

Such structures offer potential advantages over alternatives, including light weight and high packing density. These two unique features kindle the idea of using tensegrity structures as deployable structures for space applications. They are also very flexible, and their configuration can be controlled easily. Cables can serve as sensors and actuators while also carrying loads. Therefore, a control system may readily be integrated using cables.

The idea of deployable tensegrity structures for space applications was first proposed by Furuya [14]. He examined deployment of tensegrity structures conceptually and made important contributions. Hanaor [15] considered double-layer tensegrity grids as deployable structures. Sultan and Skelton [16] investigated the deployment of tensegrity structures using cable actuation. Tibert and Pellegrino [17] made contributions to deployment of tensegrity structures in which the deployment rate is controlled by a telescopic strut. A different type of tensegrity boom was investigated by Pinaud et al. [18] using cable actuation with the aim of increased stiffness and reduced number of actuators. More recently, Murata et al. [19] and, Russell and Tibert [20] considered inflatable tensegrity structures for deployable space structures.

In spite of the increasing number of works devoted to deployment of tensegrity booms, not a single tensegrity boom has ever flown into space. This is mainly due to the relatively low stiffness of tensegrity structures. In order to address this problem, a novel deployment strategy is proposed in this dissertation. It involves a transformation between different types of tensegrity configurations in order to increase stiffness without discarding initial high packing capabilities.

This dissertation is organized as follows. The mechanics of tensegrity structures is reviewed, and important problems including form and force finding are addressed in Chapter 2. In Chapter 3, a nonlinear finite element model is described, and static and dynamic analyses of fixed-configuration tensegrity structures are investigated. Deployment of different types of tensegrity booms are described, and deployment simulations are conducted in Chapter 4. Chapter 5 introduces a novel multi-stage deployment strategy for tensegrity booms which yields high packing density and high stiffness, in order to increase their utilization for space applications. In Chapter 6, sizing and pre-stress optimization of tensegrity structures is studied, and the multi-stage deployment strategy is optimized. Many additional references are included in their corresponding chapters.

Chapter 2

Mechanics of Tensegrity Structures

After the invention of tensegrity structures, a considerable amount of attention was paid to them by artists and researchers from different fields including engineering and biology. Over time, systematic methods have been developed to study the mechanics of tensegrities. Due to their unique features of light weight, reconfigurability and flexibility, they have been mostly studied by engineers with a hope to find solutions to problems in various challenging areas.

Tensegrity structures can be classified according to the maximum number of struts connected at a single node [21]. Even though compression members in a classical tensegrity are described as discontinuous, contact between k compression members can be envisioned [22]. Classical Class-1 tensegrity systems have relatively low stiffness, which is their greatest disadvantage in many applications. However, this disadvantage can be overcome in principle by employing Class-k tensegrity concepts. Class-1 tensegrities are superior, however, to Class-k tensegrities in terms of packaging efficiency.

In this chapter, tensegrity structures and their mechanics are investigated from an engineering point of view. Self-equilibrium equations of tensegrity structures are derived, and the relation between static and kinematic indeterminacies and self-equilibrium is explained. Furthermore, two important problems regarding tensegrity equilibrium, namely form and force finding, are addressed, and solution methods are briefly reviewed.

2.1 Equilibrium Equations

Tensegrity structures are self-equilibrated structures due to the presence of pre-stress in the members. This means at each node of the structure, force balance is satisfied in three directions. Therefore, in the absence of external forces, tensegrity structures are also free standing, meaning that a fixed node and external actions such as external forces or constraints are not necessary.

Before discussing and deriving the self-equilibrium equations and the mechanics of tensegrity structures, key terms are defined here. *Nodes* are spatial points located at each end of struts. *Elements* or *Members* represent any of the structural members: tension and compression carrying members, cables or struts. *Connectivity* gives the information about which node is connected to which other node by which element. The *force-density* matrix is a matrix which enables the equilibrium equations to be expressed at each node in matrix form in terms of nodal coordinates. Analogously, the *equilibrium matrix* represents the equilibrium equations in terms of force-densities in each element.

The important assumptions for derivation of the equilibrium equations are as follows:

1. The connectivity of the system is known
2. Members are connected to each other with ideal ball joints
3. The self-weight of the structure is neglected
4. External forces act only at nodes

The method of joints can be used to write down the equilibrium equations for a tensegrity structure at each node. A small part of a two-dimensional tensegrity structure is illustrated in Figure 2.1. Node i is connected to nodes j and k with elements, either cables or struts. The lengths of these elements are represented by l while pre-stress and applied external forces are represented by f and f^e. Furthermore, the nodal coordinates are also indicated by x and y.

Then the self-equilibrium equations at node i can be written as:

$$\begin{aligned}(x_i - x_j)f_{i,j}/l_{i,j} + (x_i - x_k)f_{i,k}/l_{i,k} &= f^e_{i,x} \\ (y_i - y_j)f_{i,j}/l_{i,j} + (y_i - y_k)f_{i,k}/l_{i,k} &= f^e_{i,y}\end{aligned} \tag{2.1}$$

where $\Delta x_{i,j}/l_{i,j}$ and $\Delta y_{i,j}/l_{i,j}$ are direction cosines and $l_{i,j} = \sqrt{\Delta x_{i,j}^2 + \Delta y_{i,j}^2}$.

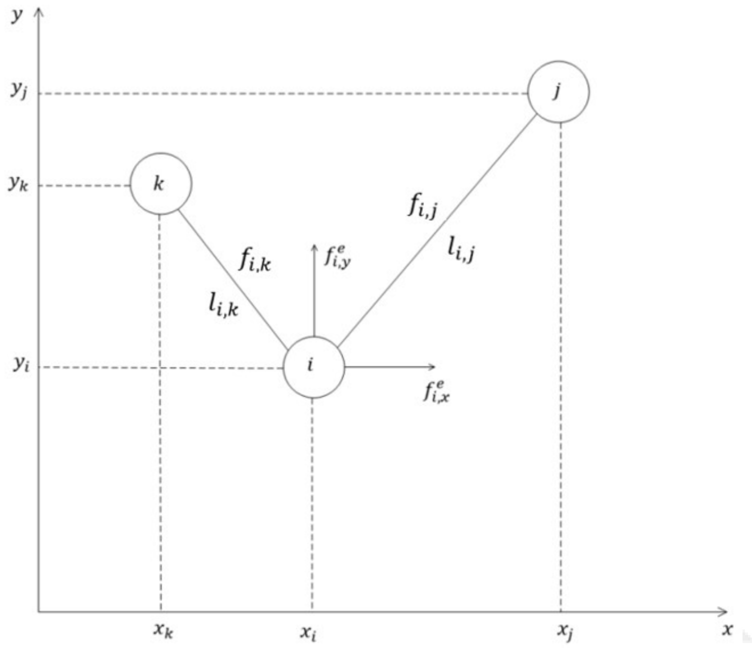

Figure 2.1: Force balance at a node

The equilibrium equations given in Equation 2.1 are nonlinear in the nodal coordinates. Since the length of each member depends on the nodal locations, quadratic terms appear when lengths are represented in terms of nodal coordinates. An attempt was made by Schek [23] to "linearize" the equations by the use of a quantity called, *force density*. In other words, this new term force density is the force carried by members per unit length, i.e. $q_{i,j} = f_{i,j}/l_{i,j}$. By treating the force density terms as a new independent variable, the equilibrium equations are linearized as shown below:

$$\begin{aligned} (x_i - x_j)q_{i,j} + (x_i - x_k)q_{i,k} &= f_{i,x}^e \\ (y_i - y_j)q_{i,j} + (y_i - y_k)q_{i,k} &= f_{i,y}^e \end{aligned} \tag{2.2}$$

Equation 2.2 can be rearranged and put into a form that allows a matrix representation of the equilibrium equations.

$$\begin{aligned} (q_{i,j} + q_{i,k})x_i - q_{i,j}x_j - q_{i,k}x_k &= f_{i,x}^e \\ (q_{i,j} + q_{i,k})y_i - q_{i,j}y_j - q_{i,k}y_k &= f_{i,y}^e \end{aligned} \tag{2.3}$$

In order to represent the equilibrium equations compactly, a connectivity matrix is suggested [23] which carries the information of the links between nodes. The entries in the connectivity matrix, $\mathbf{C}$, $(\in R^{mxn})$ take values of 1, -1 or 0 where m and n are the number of elements and nodes, respectively. Each row represents an element while columns stand for nodes. If an element connects two nodes, one of the entries at a node-column for this element-row takes the value of +1, while the other entry takes the value of -1. All other entries of the matrix in that row take the value of 0.

Assuming element k connects nodes i and j, then, the connectivity matrix can be constructed as follows:

$$\mathbf{C}_{(k,p)} = \begin{cases} 1 & \text{if } p = i \\ -1 & \text{if } p = j \\ 0 & \text{if otherwise} \end{cases} \tag{2.4}$$

The equilibrium equations for tensegrity structures can be compactly written as below using the connectivity matrix [23]

$$\mathbf{C}^{\mathbf{T}}\mathbf{Q}\mathbf{C}\mathbf{x}_i = \mathbf{f}^{e}_{\mathbf{x},i} \tag{2.5}$$

Here $\mathbf{f}^{e}_{\mathbf{x},i}$ and $\mathbf{x}_i$ denote the applied external load vector in the i^{th} direction and nodal coordinates, respectively. $\mathbf{Q}$ is a diagonal square matrix which carries the force-density information as

$$\mathbf{Q} = diag(\mathbf{q}) \tag{2.6}$$

where $\mathbf{q}(\in R^{m})$ is the force-density vector, representing the force-densities in each element

$$\mathbf{q} = [q_1, q_2, q_3, ..., q_m]^T \tag{2.7}$$

For a small part of the structure shown in Figure 2.1, the connectivity matrix, $\mathbf{C}$, and the diagonal square matrix, $\mathbf{Q}$, are written as

$$\mathbf{C} = \begin{bmatrix} 1 & -1 & 0 \\ 1 & 0 & -1 \end{bmatrix} \qquad \mathbf{Q} = \begin{bmatrix} q_{i,j} & 0 \\ 0 & q_{i,k} \end{bmatrix} \tag{2.8}$$

The equilibrium equations in x direction can be written as

$$\mathbf{C^T Q C x} = \begin{bmatrix} q_{i,j}+q_{i,k} & -q_{i,j} & -q_{i,k} \\ -q_{i,j} & q_{i,j} & 0 \\ -q_{i,k} & 0 & q_{i,k} \end{bmatrix} \begin{bmatrix} x_i \\ x_j \\ x_k \end{bmatrix} = \begin{bmatrix} f^e_{i,x} \\ ... \\ ... \end{bmatrix} \tag{2.9}$$

Equation 2.9 can be expanded into three-dimensional space to represent the equilibrium equations compactly with matrix notation. In Equation 2.9, only a small part of the structure is considered; therefore, no information about the forces acting at the i^{th} and j^{th} nodes are available.

Under the assumption of no external force acting on the structure, Equation 2.5 can be written as in Equation 2.10, which are called self-equilibrium equations, by defining a new matrix called the force-density matrix [24–26]. Vassart and Motro [27] suggest a method to directly construct the force-density matrix which does not involve the connectivity matrix.

$$\mathbf{D}\mathbf{x}_i = \mathbf{0} \tag{2.10}$$

where $\mathbf{D}(\in R^{nxn})$ is the force-density matrix given below.

$$\mathbf{D} = \mathbf{C^T Q C} \tag{2.11}$$

The force-density matrix is symmetric and singular. The first application of the force-density matrix was on cable net structures which consist solely of tension carrying members, and therefore it is always positive definite [23]. On the other hand, since tensegrity structures also host compressive elements, the force-density matrix becomes positive semi-definite [35]. For a three-dimensional space, the final form of the self-equilibrium equations are

$$\mathbf{D}[\mathbf{x}\ \mathbf{y}\ \mathbf{z}] = [\mathbf{0}\ \mathbf{0}\ \mathbf{0}] \tag{2.12}$$

Similarly, another representation of the self-equilibrium equations can be obtained after rearranging Equation 2.12. This representation is in terms of nodal coordinates and a new matrix, the equilibrium matrix, is introduced.

$$\mathbf{C^T Q C x}_i = \mathbf{A}_i\mathbf{q} = \mathbf{0} \tag{2.13}$$

where $\mathbf{A}(\in R^{dnxm})$ is the equilibrium matrix. In three-dimensional space, the equilibrium matrix is given as [13]

$$\mathbf{A} = \begin{bmatrix} \mathbf{C^T} diag(\mathbf{Cx}) \\ \mathbf{C^T} diag(\mathbf{Cy}) \\ \mathbf{C^T} diag(\mathbf{Cz}) \end{bmatrix} \tag{2.14}$$

Equations 2.12 and 2.13 are linear homogeneous versions of the self-equilibrium equations and, in fact, they are the same with different representations. Equation 2.12 represents the self-equilibrium equations in terms of nodal coordinates while Equation 2.13 is in terms of force-densities. For a tensegrity structure, these equations have to be satisfied simultaneously in order to ensure a self-equilibrated geometry.

2.1.1 Rank Deficiency Conditions

In order to generate a d-dimensional self-equilibrated tensegrity configuration, two rank conditions need to be satisfied alongside the equilibrium equations [13, 24, 28]. These rank conditions are on the equilibrium and the force-density matrices. Potential solutions for the nodal coordinates and the force-densities are obtained from the nullspace of the corresponding matrices. The first rank deficiency condition ensures that a d-dimensional structure is generated, while the second condition allows the determination of the force-density vector.

The first rank deficiency condition is given as

$$n_D \geq d + 1 \tag{2.15}$$

where

$$n_D = n - r_D \tag{2.16}$$

where n and r_D are the number of nodes and the rank of the force-density matrix. This condition ensures that at least d particular solutions can be obtained for Equation 2.12, generating a d-dimensional structure [25, 26, 29]. For a d-dimensional tensegrity structure, the largest possible rank of $\mathbf{D}$ is $r_D = n - d - 1$ for geometric embedding into R^d [25, 26, 29].

The second rank deficiency condition is

$$n_A = m - r_A \geq 1 \tag{2.17}$$

where m and r_A are the number of members and the rank of the equilibrium matrix. This condition is the prestressability condition for a tensegrity structure and ensures that the structure has at least one force-density vector or state of self-stress that satisfies equilibrium. This rank deficiency or nullity allows a non-trivial solution for Equation 2.13 to be found from the nullspace of the equilibrium matrix.

These two rank deficiency conditions play key roles in generating a d-dimensional, self-equilibrated tensegrity configuration. In the literature, several publications are devoted to this matter, explaining the mathematical theory behind it [24, 25, 28, 29]. Another explanation can be sought in terms of static and kinematic indeterminacies, given in the next subsection.

2.1.2 Static and Kinematic Indeterminacy

A structure is said to be statically determinate if the number of available independent equilibrium equations is equal to the number of unknown forces. This allows the forces to be determined from the equilibrium equations uniquely. However, if the number of unknowns is greater than the number of equilibrium equations, the forces cannot be uniquely determined, and the system is then called statically indeterminate. In such systems, in order to determine the forces, compatibility equations are required.

If a structure exhibits additional modes of deformation other than rigid body motion, then it is said to be kinematically indeterminate. Another explanation is that the locations of the joints cannot be uniquely determined by the length of the members. Kinematically indeterminate structures exhibit infinitesimal mechanisms, a type of mechanism in which the length variations of the individual members are infinitesimal of a lower order than the order of the displacements [2].

The level of static and kinematic indeterminacies are governed by Maxwell's rule [30]. In a d dimensional space, Maxwell's rule is

$$dn - m - n_b = n_m - n_s \tag{2.18}$$

where n_s is the number of independent states of self-stress, n_m is the total number of infinitesimal mechanisms, n is the number of joints or nodes, m is the number of bars/elements in the structure, and n_b is the number of rigid body motions. If either of n_s and n_m is found, then the other can be determined by Maxwell's Rule.

On the other hand, the number of independent states of self-stress and the total number of infinitesimal mechanisms can be obtained by the matrix analysis developed by Pellegrino and Calladine [31]. The matrix analysis utilizes the rank of the equilibrium matrix and the number of members present in the structure. They are given as

$$n_s = m - r_A \tag{2.19}$$

$$n_m = dn - n_b - r_A \tag{2.20}$$

which satisfy Maxwell's Rule. Based on these parameters, pin-jointed structures can be classified as follows [30, 31]:

- $n_s = 0$, $n_m = 0$: Statically and kinematically determinate
- $n_s = 0$, $n_m \geq 1$: Statically determinate and kinematically indeterminate
- $n_s \geq 1$, $n_m = 0$: Statically indeterminate and kinematically determinate
- $n_s \geq 1$, $n_m \geq 1$: Statically and kinematically indeterminate

Tensegrity structures show static indeterminacy, which is imperative for self-equilibrium. The self-equilibrium is satisfied by the state of self-stress found from the nullspace of the equilibrium matrix. On the other hand, tensegrity structures are often kinematically indeterminate, which reduces the overall stiffness of the structure due to mechanisms found in the structure. The effects of infinitesimal mechanisms on the stiffness of tensegrity structures are discussed in more depth in Chapter 3.

2.2 Form Finding

The form-finding problem of tensegrity structures is an essential part of the tensegrity design problem. It seeks a solution to Equations 2.12 and 2.13 with a predefined or known connectivity. The solution yields a geometric shape and a force-density vector that satisfy the self-equilibrium equations as well as the rank deficiency conditions. The obtained nodal locations and the force-density values are relative and can be normalized in different ways. Over the years, numerous form finding methods have been developed and new methods are sought for designing mostly irregular tensegrity structures.

The most commonly used methods for form-finding include analytical methods (mostly applicable to simple and symmetrical tensegrities), non-linear programming and energy methods. A small list of the form finding methods can be given as

- Analytical methods
- Non-linear programming
- Dynamic relaxation
- Reduced coordinates
- Energy method
- Force-density method
- Algebraic method

More information about the methods listed above can be found in the review paper published by Tibert and Pellegrino [26]. In this dissertation, the force-density method for the form-finding problem is chosen due to its straightforwardness and relative ease of implementation. Search of new tensegrity configurations is not the focus of this dissertation, and the form-finding problem is mostly used for validation purposes.

The force-density method was first suggested by Schek in 1974 for the form finding problem of cable net structures [23]. This method introduces force-densities to equilibrium equations for linearization purposes, $q_i = f_i/l_i$. Then, the method is extended for the form-finding problem of tensegrity structures. In the literature, many applications of the force-density method are available which employ analytical, semi-analytical, and numerical approaches [27, 32–34]. In the last decade, novel numerical force-density methods emerged in order to reduce the complexity of the problem [24, 25, 29, 35].

As more powerful computers were developed, the research on force-density form-finding methods shifted to numerical and semi-analytical approaches rather than analytical methods. The increased computational power allowed researchers to develop iterative algorithms to find self-equilibrated geometries. Furthermore, modified numerical methods allowed the search of complex and irregular tensegrity geometries. A form-finding method which specializes in designing tensegrity structures with partially defined geometry and a known set of force-densities is called *unique configuration search* [25, 35].

In the following subsections, numerical and semi-analytical force-density form-finding methods are investigated in further detail. For demonstration purposes, the simplest three-dimensional tensegrity structure, the *triplex*, is selected and the form finding problem is solved with numerical and semi-analytical methods. The geometry of the triplex is shown in Figure 2.2.

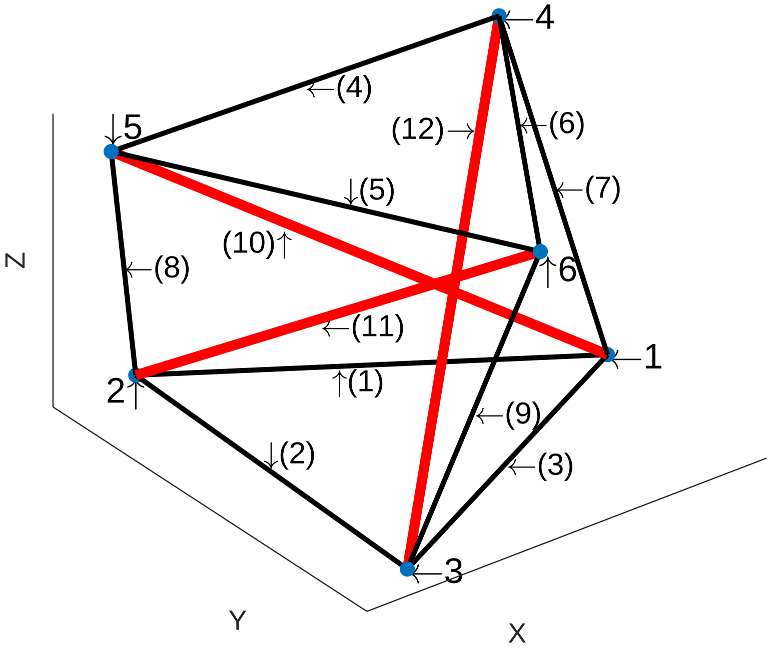

Figure 2.2: Three-Strut Cylindrical Tensegrity "Triplex"

Figures 2.3 and 2.4 provide the top and side views of the triplex. The structure has 9 cables and 3 struts which are represented with black and thick red lines. Each

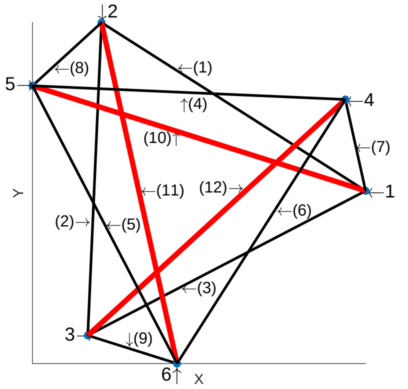

Figure 2.3: Triplex Top View

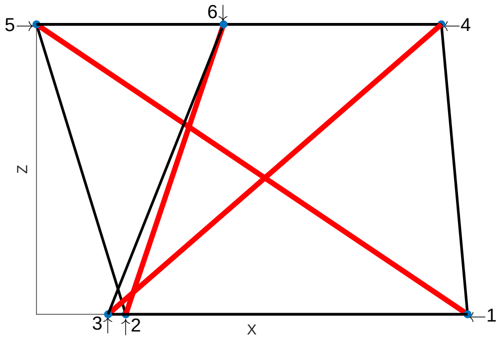

Figure 2.4: Triplex Side View

node is numbered and shown on the figures, while element numbers are indicated by numbers with brackets.

The results obtained from form-finding methods can be scaled by multiplying force-density values and/or nodal coordinates by a constant since they are relative. The scaling of force-densities is achieved with a coefficient known as the *pre-stress coefficient*. To find the actual forces in members, the force-densities are multiplied by the lengths of elements. Then, forces in elements are given as follows:

$$\mathbf{f} = P_s \mathbf{L} \mathbf{q} \tag{2.21}$$

where $\mathbf{f}$ is a column vector which stores the forces in each element. P_s is the pre-stress coefficient, $\mathbf{q}$ is the force-density vector, and $\mathbf{L}$ is a diagonal square matrix of member lengths.

2.2.1 Numerical Form-Finding

This numerical force-density form-finding method is developed by Estrada [24], and it exploits computational power to iteratively update the force-densities and nodal coordinates until the self-equilibrium equations are satisfied. The required information for the numerical force-density form finding method is connectivity and element type (cable or strut). Force-density values of +1 and -1 are assigned to corresponding elements, and the force-density vector is constructed. The algorithm updates force-densities and nodal coordinates until the generated configuration has at least one state of self-stress and the self-equilibrium equations are satisfied alongside with rank deficiency conditions.

The initial step in numerical form finding is to intuitively guess the connectivity between the nodes and the connecting element types. Then, the connectivity matrix can be constructed and, with the assignment of force-densities to corresponding elements, the numerical form-finding process can be started. The triplex shown in Figure 2.2 has 12 elements and 6 nodes; therefore, the connectivity matrix is 12 × 6, as given:

$$\mathbf{C} = \begin{bmatrix} 1 & -1 & 0 & 0 & 0 & 0 \\ 0 & 1 & -1 & 0 & 0 & 0 \\ 1 & 0 & -1 & 0 & 0 & 0 \\ 0 & 0 & 0 & 1 & -1 & 0 \\ 0 & 0 & 0 & 0 & 1 & -1 \\ 0 & 0 & 0 & 1 & 0 & -1 \\ 1 & 0 & 0 & -1 & 0 & 0 \\ 0 & 1 & 0 & 0 & -1 & 0 \\ 0 & 0 & 1 & 0 & 0 & -1 \\ 1 & 0 & 0 & 0 & -1 & 0 \\ 0 & 1 & 0 & 0 & 0 & -1 \\ 0 & 0 & 1 & -1 & 0 & 0 \end{bmatrix} \tag{2.22}$$

The force-density vector is 12 × 1, and the corresponding entries for cables and struts are assigned with +1 and -1, respectively.

$$\mathbf{q} = \begin{bmatrix} 1 & 1 & 1 & 1 & 1 & 1 & 1 & 1 & 1 & -1 & -1 & -1 \end{bmatrix}^T \tag{2.23}$$

Then, the force-density matrix can be constructed as

$$\mathbf{D} = \begin{bmatrix} 2 & -1 & -1 & -1 & 1 & 0 \\ -1 & 2 & -1 & 0 & -1 & 1 \\ -1 & -1 & 2 & 1 & 0 & -1 \\ -1 & 0 & 1 & 2 & -1 & -1 \\ 1 & -1 & 0 & -1 & 2 & -1 \\ 0 & 1 & -1 & -1 & -1 & 2 \end{bmatrix} \tag{2.24}$$

The initial force-density matrix does not satisfy the first rank deficiency condition (Equation 2.15) and is not positive semi-definite because of the arbitrarily assigned force-densities. Then, the force-density matrix is decomposed into its eigenvalues and eigenvectors, Λ and Φ, respectively.

$$\mathbf{D} = \Phi \Lambda \Phi^T \tag{2.25}$$

The nodal locations can be approximated from the eigenvector columns as long as two conditions are satisfied. An eigenvector column is a candidate for nodal locations as long as none of the members have zero length, and that column and $\mathbf{I}_i$, the i^{th} column vector of the identity matrix, are linearly independent (where $\mathbf{I}$ is the identity matrix). The projected lengths can be calculated as

$$\mathbf{L} = \mathbf{C}\Phi = [(\mathbf{C}\phi_1) \quad (\mathbf{C}\phi_2) \quad \dots \quad (\mathbf{C}\phi_{n_D})] \tag{2.26}$$

The candidate eigenvector columns are removed if one of the following conditions on linear dependency and zero length members, respectively, are satisfied.

$$\mathbf{C}\phi_i = 0 \tag{2.27}$$

$$det|\mathbf{L}_d \mathbf{L}_d^T| = 0 \tag{2.28}$$

where in three dimensional space

$$\mathbf{L}_d = \sqrt{(\mathbf{C}\phi_i)^2 + (\mathbf{C}\phi_j)^2 + (\mathbf{C}\phi_k)^2} \tag{2.29}$$

After removing the corresponding columns, the remaining first three columns are selected as nodal locations. Most commonly, the eigenvectors of the smallest eigenvalues are selected, and they are iteratively updated until the eigenvalues are zero, satisfying the rank deficiency condition [24, 35].

Then, the selected eigenvectors are used as nodal coordinates to construct the equilibrium matrix, $\mathbf{A}$, using Equation 2.14. Singular value decomposition is applied to the equilibrium matrix as in Equation 2.30, in order to obtain the left and right nullspace vectors and the singular values.

$$\mathbf{A} = \mathbf{U}\mathbf{V}\mathbf{W}^T \tag{2.30}$$

U and **W** are unitary matrices that also include the left and right nullspace vectors, respectively, while **V** is the diagonal matrix in which the singular values are stored. The last column of **W** is the right nullspace vector of the equilibrium matrix and can be chosen as the force-density vector.

However, in the beginning of the iterations, the equilibrium matrix is unlikely to be rank deficient as required and has no nullspace. In this case, none of the columns of **W** is a solution to Equation 2.13. The column whose signs of entries are identical to the ones determined initially for the force-density vector is selected. If none of the columns are in such a condition, then more than one column is required to approximate an updated force-density vector, **q**. Using a least square fit, it is possible to calculate $\tilde{\mathbf{q}}$, that minimizes the following quantity:

$$\left\| [w_j \quad \dots \quad w_m]\tilde{\mathbf{q}} - \mathbf{q} \right\|^2 \tag{2.31}$$

where the updated force-densities

$$\mathbf{q}^* = [w_j \quad \dots \quad w_m]\tilde{\mathbf{q}} \tag{2.32}$$

This procedure, if needed, starts by taking the two rightmost column vectors of **W** and increases the number of column vectors until the sign of the entries of $\mathbf{q}^*$ matches the sign of the entries of **q**. Then $\mathbf{q}^*$ becomes the updated force-density vector and the force-density matrix is calculated again with the updated force-densities. This process iteratively continues until the rank deficiency conditions are satisfied and the structure has at least one state of self-stress.

As a result of the iterations in the present example, the force-density vector converges to:

$$\mathbf{q} = \begin{bmatrix} 1 & 1 & 1 & 1 & 1 & 1 & \sqrt{3} & \sqrt{3} & \sqrt{3} & -\sqrt{3} & -\sqrt{3} & -\sqrt{3} \end{bmatrix}^T \tag{2.33}$$

Then, the final form of the force-density matrix (having a nullity of 4) is obtained as

$$\mathbf{D} = \begin{bmatrix} 2 & -1 & -1 & \sqrt{3} & 0 & -\sqrt{3} \\ -1 & 2 & -1 & -\sqrt{3} & \sqrt{3} & 0 \\ -1 & -1 & 2 & 0 & -\sqrt{3} & \sqrt{3} \\ \sqrt{3} & -\sqrt{3} & 0 & 2 & -1 & -1 \\ 0 & \sqrt{3} & -\sqrt{3} & -1 & 2 & -1 \\ -\sqrt{3} & 0 & \sqrt{3} & -1 & -1 & 2 \end{bmatrix} \tag{2.34}$$

The nodal locations are then obtained from the right nullspace vector of the force-density matrix, and the generated geometry is shown in Figures 2.2, 2.3 and 2.4. As can be seen from the figures, the structure is symmetric and has different members carrying the same loads. In this example, these members are the top and bottom cables, vertical cables, and struts. These members have the same lengths and the same force-density values. The grouping of members is discussed in the semi-analytical form-finding and force-finding subsections in more depth.

In summary, with only minimal knowledge of the investigated tensegrity system, this numerical method enables searching for valid tensegrity configurations. If the force-density vector is defined to consist of +1 and -1, the obtained configurations are mostly regular and symmetrical tensegrities. It is also possible to alter the initial force-density matrix $\mathbf{q}$ in a way that the signs of the entries are preserved while the numbers are changed, say to random values. This time the resulting configuration may be irregular; however, it is likely to end with a trivial result or to diverge.

2.2.2 Semi-Analytical Form Finding

Semi-analytical form finding methods differ from numerical force-density form finding methods by assigning symbolic variables instead of numerical values [27]. The force-density vector and the force-density matrix are constructed symbolically. After construction of the force-density matrix, the first rank deficiency condition is imposed to the force-density matrix, and the solution is obtained for the force-densities. Finally, with knowledge of the force-density values, the nodal coordinates can be obtained from Equation 2.12 by calculating the nullspace vector of the force-density matrix.

Symbolically constructed force-density matrix can be reduced to upper echelon form by employing Gaussian elimination. In order to achieve the rank deficiency condition on the force-density matrix, all the entries in the required number of rows can be set to zero, yielding a symbolic solution. However, this approach is mostly limited to symmetrical tensegrity structures due to the difficulty in obtaining the upper echelon form.

After careful investigation of symmetric tensegrity structure, the members which carry identical force-densities can be identified and they can be assigned the same symbolic force density. Going through the construction of the force-density matrix and the application of the rank deficiency condition yields the ratio between the force-densities in different groups of members.

The triplex example investigated with the numerical form-finding method is considered again. The connectivity matrix remains the same; however, the force-density vector is replaced with a symbolic one given in Equation 2.35 below. Careful examination shows that a geometric symmetry can exist in the structure. Given such symmetry, similarly positioned, identical members are identified. Based on that, the force-densities are assigned as follows:

1. Cables between nodes 1-2-3: q_t (Top cables)
2. Cables between nodes 4-5-6: q_b (Bottom cables)
3. Cables between nodes 1-4, 2-5, 3-6: q_v (Vertical cables)
4. Struts between nodes 1-5, 2-6, 3-4: $-q_s$ (Struts)

$$\mathbf{q} = \begin{bmatrix} q_t & q_t & q_t & q_b & q_b & q_b & q_v & q_v & q_v & -q_s & -q_s & -q_s \end{bmatrix}^T \tag{2.35}$$

When the bottom and the top triangles are assumed to be horizontal, in order to satisfy the force balance, by inspection, it can be seen that $q_s = -q_v$. Using this relation, the force-density matrix is constructed using MATLAB's symbolic toolbox, MuPAD, as follows:

$$\mathbf{D} = \begin{bmatrix} 2q_t & -q_t & -q_t & -q_v & q_v & 0 \\ -q_t & 2q_t & -q_t & 0 & -q_v & q_v \\ -q_t & -q_t & 2q_t & q_v & 0 & -q_v \\ -q_v & 0 & q_v & 2q_b & -q_b & -q_b \\ q_v & -q_v & 0 & -q_b & 2q_b & -q_b \\ 0 & q_v & -q_v & -q_b & -q_b & 2q_b \end{bmatrix} \tag{2.36}$$

Employing Gaussian elimination, the upper echelon form of the force-density matrix is obtained by MuPAD

$$\mathbf{D} = \begin{bmatrix} q_v & -q_v & 0 & -q_b & 2q_b & -q_b \\ 0 & q_t & -q_t & -\sigma_1 & 2\sigma_1 - q_v & -\sigma_1 + q_v \\ 0 & 0 & 0 & \sigma_2 & -2\sigma_2 & \sigma_2 \\ 0 & 0 & 0 & 0 & \sigma_3 & -\sigma_3 \\ 0 & 0 & 0 & 0 & 0 & 0 \\ 0 & 0 & 0 & 0 & 0 & 0 \end{bmatrix} \tag{2.37}$$

where

$$\begin{aligned} \sigma_1 &= \frac{q_b q_t}{q_v} \\ \sigma_2 &= \frac{3q_b q_t - q_v^2}{q_v} \\ \sigma_3 &= \frac{3q_b q_t - q_v^2}{q_t} \end{aligned} \tag{2.38}$$

In order to satisfy the rank deficiency condition of the force-density matrix, the required nullity is 4 (for a three dimensional structure), meaning that all the entries in 4 rows must be zero. In this case, two rows already satisfy this condition while two more rows are required. Therefore, the solution can be obtained by setting $\sigma_2 = 0$ and $\sigma_3 = 0$. This yields,

$$q_t = \frac{q_v^2}{3q_b} \tag{2.39}$$

$$q_b = q_b \tag{2.40}$$

$$q_v = q_v \tag{2.41}$$

$$q_s = -q_v \tag{2.42}$$

The results show that two of the assigned force-densities can be selected arbitrarily while the other two are represented in terms of the selected ones. These expressions allow free selection of some force-densities and computation of the others. Then using the feasible force-densities found here, the geometry of the structure can be obtained from Equation 2.12.

In this example, selecting $q_b = 1$ and $q_v = 1$, q_t is calculated and the equilibrium equations are solved. The resulting geometry is shown in Figures 2.5 and 2.6.

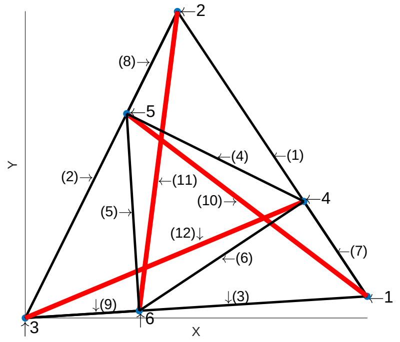

Figure 2.5: First set of force-densities: Top view

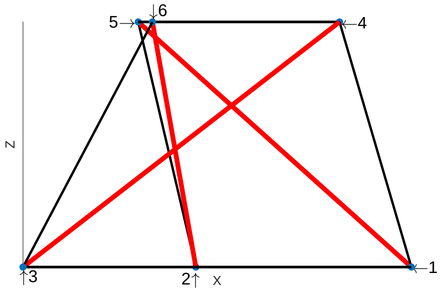

Figure 2.6: First set of force-densities: Side view

Figures 2.5 and 2.6 show that the configuration is clearly different from the one found using numerical form finding as it has an inscribed top triangle. Additionally, by varying the free selected force-densities with the expressions obtained (Equations 2.39, 2.40, 2.41 and 2.42), it is possible to reconfigure the structure.

Selecting the force-densities as $q_b = 1$ and $q_v = 1/2$, and solving the equilibrium equations yield a different tensegrity configuration, which is shown in Figures 2.7 and 2.8. These two different force-density cases show that it is possible to have some control over the length ratios of the elements by adjusting the force-densities. This could be achieved in practice (in principle) via cable actuation and allows deployment or shape modifications which are addressed in the next chapter.

Even though the semi-analytical form finding method offers some advantages, it requires high computation power for larger tensegrities in computing the upper echelon form when it is difficult to identify the symmetry and assign appropriate force-densities.

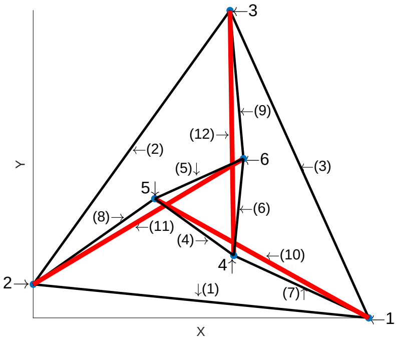

Figure 2.7: Second set of force-densities: Top view

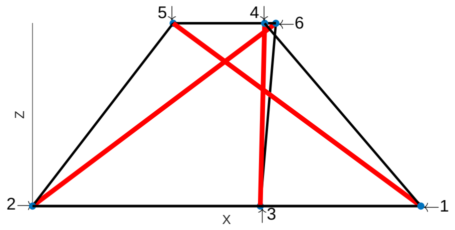

Figure 2.8: Second set of force-densities: Side view

2.3 Force Finding

The force finding method is another tool used for design of tensegrity structures, and it differs from form finding methods by definition. The force finding method, as revealed by the name, looks for the force-densities that satisfy force balance at each node for a predefined configuration (connectivity and nodal locations). This method is also known as initial self-stress design [36].

Known connectivity and nodal coordinates allow the construction of the equilibrium matrix with Equation 2.14, which does not require any information of force-densities in the members. By calculating the rank of the equilibrium matrix, the number of independent state of self-stress can be obtained from Equation 2.19. Similar to the numerical form finding method, singular value decomposition is applied to the equilibrium matrix as in Equation 2.43.

$$\mathbf{A} = \mathbf{U}\mathbf{V}\mathbf{W}^T \tag{2.43}$$

As noted before, the last n_s columns of matrix $\mathbf{W}$ are the right nullspace vectors of the matrix $\mathbf{A}$. Then, based on the number of independent state of self-stress, two possibilities occur.

Case I

If the number of states of self-stress is equal to 1 ($n_s = 1$), there is only one vector in the right nullspace, and it satisfies the self-equilibrium equations, Equation 2.13.

Due to distinct computational approaches taken by different software, the obtained force-density vector, $\mathbf{q}$, might be found in a way that all cables carry compression and struts carry tension. Since the force-density values are relative, in order to satisfy unilateral behavior of elements, the force-density vector can be multiplied by -1.

Case II

If the number of states of self-stress is greater than one ($n_s > 1$), there are n_s number of independent state of self-stress, and, individually, they do not necessarily satisfy the unilateral behavior of elements. Then, the force-density vector needs to be expressed as a linear combination of the last n_s columns of matrix $\mathbf{W}$ as in Equation 2.44.

$$\mathbf{q} = c_1\mathbf{w}_{m-n_s+1} + c_2\mathbf{w}_{m-n_s+2} + c_3\mathbf{w}_{m-n_s+3} + \cdots + c_{n_s}\mathbf{w}_m \tag{2.44}$$

where $\mathbf{c}$ is the coefficient vector for n_s independent self-stress modes. For convenience and simplicity, the last n_s columns of matrix $\mathbf{W}$ is also stored in a matrix $\mathbf{G}$.

$$\mathbf{c} = \begin{Bmatrix} c_1 & c_2 & \cdots & c_{n_s} \end{Bmatrix} \tag{2.45}$$

$$\mathbf{W} = \begin{bmatrix} \mathbf{w}_1 & \mathbf{w}_2 & \cdots & \mathbf{w}_{r_A} & |\mathbf{w}_{m-n_s+1} & \mathbf{w}_{m-n_s+2} & \cdots & \mathbf{w}_m \end{bmatrix} \tag{2.46}$$

$$\mathbf{G} = \begin{bmatrix} \mathbf{g}_1 & \mathbf{g}_2 & \cdots & \mathbf{g}_{n_s} \end{bmatrix} = \begin{bmatrix} \mathbf{w}_{m-n_s+1} & \mathbf{w}_{m-n_s+2} & \cdots & \mathbf{w}_m \end{bmatrix} \tag{2.47}$$

Then, the force-density vector can be written as

$$\mathbf{q} = \mathbf{G}\mathbf{c} \tag{2.48}$$

The columns of $\mathbf{G}$ do not necessarily satisfy the unilateral behavior of elements since the equilibrium matrix does not carry the information of element type. In order to overcome this problem, the members that carry the same amount of force density are sought for [36]. A geometric symmetry can be found by identifying the members in similar positions with same length, carrying identical force density.

This symmetry can be used to create h groups among the elements. Following that, the force-density vector can be written as

$$\mathbf{q} = \begin{Bmatrix} q_1 & q_1 & \cdots & q_i & q_i & \cdots & q_h & q_h \end{Bmatrix}^T = \begin{bmatrix} 1 & 0 & 0 & 0 & 0 \\ \vdots & 1 & 0 & 0 & 0 \\ 0 & \vdots & 1 & 0 & 0 \\ 0 & 0 & \vdots & 1 & \vdots \\ 0 & 0 & 0 & \vdots & 1 \end{bmatrix} \begin{bmatrix} q_1 \\ \vdots \\ q_i \\ \vdots \\ q_h \end{bmatrix} \tag{2.49}$$

More compactly,

$$\mathbf{q} = \begin{Bmatrix} q_1 & \cdots & q_i & \cdots & q_h \end{Bmatrix}^T = \begin{bmatrix} \mathbf{e}_1 & \cdots & \mathbf{e}_i & \cdots & \mathbf{e}_h \end{bmatrix} \begin{bmatrix} q_1 \\ \vdots \\ q_i \\ \vdots \\ q_h \end{bmatrix} \tag{2.50}$$

where q_i is the force density in the members of the i^{th} group end $\mathbf{e}_i$ is a column vector whose entries corresponding to i^{th} group are 1 while the others are 0, i.e. a basis vector. Substitution of Equation 2.50 into Equation 2.48 yields

$$c_1\mathbf{g}_1 + c_2\mathbf{g}_2 + \cdots + c_{n_s}\mathbf{g}_{n_s} - \mathbf{e}_1 q_1 - \mathbf{e}_2 q_2 - \cdots - \mathbf{e}_h q_h = \mathbf{0} \tag{2.51}$$

In matrix notation

$$\bar{\mathbf{G}}\bar{\mathbf{c}} = \mathbf{0} \tag{2.52}$$

where

$$\bar{\mathbf{G}} = \begin{bmatrix} \mathbf{g}_1 & \mathbf{g}_2 & \cdots & \mathbf{g}_{n_s} & -\mathbf{e}_1 & \cdots & -\mathbf{e}_i & \cdots & -\mathbf{e}_h \end{bmatrix} \tag{2.53}$$

$$\bar{\mathbf{c}} = \begin{Bmatrix} c_1 & c_2 & \cdots & c_{n_s} & q_1 & \cdots & q_i & \cdots & q_h \end{Bmatrix}^T \tag{2.54}$$

The solution to this system, Equation 2.52, lies in the nullspace of the matrix $\bar{\mathbf{G}}$, and it is a column vector in which the coefficients, c_i's and the force-densities of each group of element are defined. However, if the nullity or rank deficiency of $\bar{\mathbf{G}}$ is greater than one, there is more than one solution. On the other hand, if the nullity of $\bar{\mathbf{G}}$ is equal to zero, then the solution is trivial. Therefore, a proper grouping of the elements by taking into account the symmetry is vital.

The force finding method has been implemented in static and dynamic analyses of tensegrity structures, investigated in Chapter 3. This method allows determination of the initial self-stress state of a tensegrity structure before the application of external loads. Another application of the force finding method is the deployment simulations conducted in Chapters 4 and 5, in order to track the forces in each elements during deployment. By doing so, it is possible to ensure that cables are always in tension and do not go slack.

Numerical Example

The force finding method is applied to a two-stage triplex tensegrity boom as shown in Figure 2.9. Top and side views are also illustrated in Figures 2.10 and 2.11. In this structure, four groups of elements can be identified, namely top and bottom cables, vertical cables, saddle cables, and struts. For sake of clarity in the figures, these groups of elements are indicated with different colors. Black, blue, and green lines represent top and bottom, vertical, and saddle cables, respectively, while thick red lines denote struts.

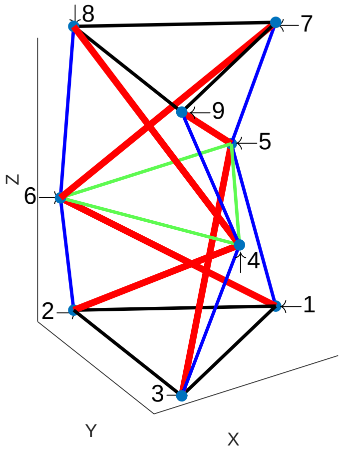

Figure 2.9: Two Stage Triplex Boom

Based on the symmetry explained above, the force-density vector is 21 × 1, and for compactness, it is given in the following form in which multiplicities are shown in brackets. q_{tb}, q_v, q_s and q_{st} represent the force-densities in the top and bottom cables, vertical cables, saddle cables, and struts, respectively.

$$\mathbf{q} = \begin{bmatrix} q_{tb}(6) & q_v(6) & q_s(3) & q_{st}(6) \end{bmatrix}^T \tag{2.55}$$

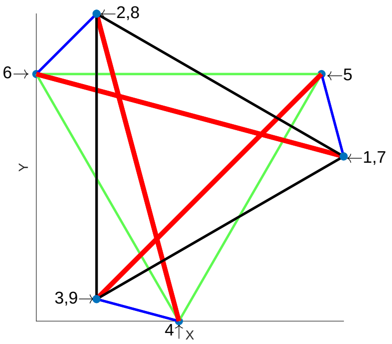

Figure 2.10: Two Stage Triplex Boom: Top View

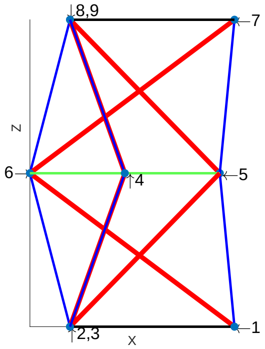

Figure 2.11: Two Stage Triplex Boom: Side View

For this numerical example, the nodal coordinates are given as

$$\mathbf{x} = \begin{Bmatrix} 10 \\ -5 \\ -5 \\ 0 \\ 8.6603 \\ -8.6603 \\ 10 \\ -5 \\ -5 \end{Bmatrix}, \quad \mathbf{y} = \begin{Bmatrix} 0 \\ 8.6603 \\ -8.6603 \\ -10 \\ 5 \\ 5 \\ 0 \\ 8.6603 \\ -8.6603 \end{Bmatrix}, \quad \mathbf{z} = \begin{Bmatrix} 0 \\ 0 \\ 0 \\ 15 \\ 15 \\ 15 \\ 30 \\ 30 \\ 30 \end{Bmatrix} \tag{2.56}$$

The equilibrium matrix is constructed with Equation 2.14, which has a nullity of 2. Equation 2.19 reveals that the number of independent state of self-stress, n_s, is equal to 2. This problem falls into Case II, and therefore, the solution to the force-density matrix is a linear combination of the last n_s columns of matrix $\mathbf{W}$, as in Equation 2.44. Application of Equation 2.52 yields

$$
\bar{\mathbf{G}}\bar{\mathbf{c}} = \begin{bmatrix}
0.1205 & 0.1667 & -1 & 0 & 0 & 0 \\
0.1205 & 0.1667 & -1 & 0 & 0 & 0 \\
0.1205 & 0.1667 & -1 & 0 & 0 & 0 \\
-0.1805 & 0.0987 & -1 & 0 & 0 & 0 \\
-0.1805 & 0.0987 & -1 & 0 & 0 & 0 \\
-0.1805 & 0.0987 & -1 & 0 & 0 & 0 \\
0.2087 & 0.2888 & 0 & -1 & 0 & 0 \\
0.2087 & 0.2888 & 0 & -1 & 0 & 0 \\
0.2087 & 0.2888 & 0 & -1 & 0 & 0 \\
-0.3126 & 0.1710 & 0 & -1 & 0 & 0 \\
-0.3126 & 0.1710 & 0 & -1 & 0 & 0 \\
-0.3126 & 0.1710 & 0 & -1 & 0 & 0 \\
-0.0600 & 0.2655 & 0 & 0 & -1 & 0 \\
-0.0600 & 0.2655 & 0 & 0 & -1 & 0 \\
-0.0600 & 0.2655 & 0 & 0 & -1 & 0 \\
-0.2087 & -0.2888 & 0 & 0 & 0 & -1 \\
-0.2087 & -0.2888 & 0 & 0 & 0 & -1 \\
-0.2087 & -0.2888 & 0 & 0 & 0 & -1 \\
0.3126 & -0.1710 & 0 & 0 & 0 & -1 \\
0.3126 & -0.1710 & 0 & 0 & 0 & -1 \\
0.3126 & -0.1710 & 0 & 0 & 0 & -1
\end{bmatrix}
\begin{Bmatrix} c_1 \\ c_2 \\ q_{tb} \\ q_v \\ q_s \\ q_{st} \end{Bmatrix} = \mathbf{0} \tag{2.57}
$$

And the nullspace of matrix $\bar{\mathbf{G}}$ yields the solution to $\bar{\mathbf{c}}$

$$
\begin{aligned}
\bar{\mathbf{c}} &= \begin{Bmatrix} c_1 & c_2 & q_{tb} & q_v & q_s & q_{st} \end{Bmatrix}^T \\
&= \begin{Bmatrix} 0.2009 & -0.8891 & -0.1240 & -0.2148 & -0.2481 & 0.2148 \end{Bmatrix}^T
\end{aligned} \tag{2.58}
$$

The obtained force-density results show that the unilateral behavior of elements is not satisfied. However, the obtained force-density vector can be normalized to the first group of elements, and the results are given in Equation 2.59, satisfying unilateral behavior.

$$
\mathbf{q} = \begin{bmatrix} q_{tb} & q_v & q_s & q_{st} \end{bmatrix}^T = \begin{bmatrix} 1 & 1.7321 & 2 & -1.7321 \end{bmatrix}^T \tag{2.59}
$$

One important point worth mentioning here is that the saddle cables, which are located at the interface of two triplex units, contribute to the equilibrium of both stages. Therefore, the force-density values in the saddle cables are generally greater than the force-densities of the top and bottom cables. Because of the equal lengths of the top, bottom, and saddle cables in this case, the force-density values of the saddle cables are greater by a factor of two.

In the next chapter, static and dynamic analyses of tensegrity structures are investigated. The developed finite element model is explained and utilized to investigate the behavior of tensegrity structures under external loads. The free vibration problem is studied, and effective stiffness properties are also obtained.

Chapter 3

Static and Dynamic Analyses of Tensegrity Structures

Design of tensegrity structures not only involves form-finding, but also requires determination of the response under external loads. In order to understand how tensegrity structures behave under external loads, determining how much they deflect is very important from a design point of view. Dynamic behavior of tensegrity structures also requires attention in order to avoid unwanted vibration problems. Therefore, it is important to develop tools to study the static and dynamic behavior of tensegrity structures.

Tensegrity structures are unique, spatially reticulated systems [37]. Generally speaking, the dynamic behavior of spatial reticulated systems is studied by linearizing the systems about its equilibria, and for most applications, the results are considered to be sufficient [38]. However, based on the mechanical properties of the materials or the type of applied loads (such as, for example, following forces), different approaches are taken. Such cases require nonlinear models to analyze deflections and behavior. The encountered nonlinearities in solid mechanics are geometric and material nonlinearities.

Tensegrity structures inherently exhibit geometric nonlinearity due to the existing pre-stress in the members which stabilize the structure. The pre-stress present in tensegrity structures presents a unique feature that is not present in typical structures. It contributes to the overall stiffness of the structure, and the effect is proportional to pre-stress levels. As deformation occurs, the force distribution in the structure varies due to external loads, considering the force balance at each node, and as a result, the effective stiffness of the structure changes. Therefore, nonlinear models and solution methods are mandatory for the static and dynamic analyses of tensegrity structures.

The earliest nonlinear model for pre-stressed structures which takes into account large displacements was developed by Argyris [39]. Motro [40] enhanced this method and applied it to tensegrity structures for static analyses. A nonlinear finite element approach was developed by Bathe [41], which can account for material and geometric nonlinearities using total or updated Lagrangian formulations. The nonlinear finite element method depends on an incremental analysis to address any possible changes that may occur such as elastic-to-plastic transition of materials when the strains reach a certain level. For tensegrity structures, this approach has to be considered for cable slackness and/or large-scale stiffness changes due to large deformations and/or displacements. Cable slackness poses a challenge since it is a non-smooth nonlinearity and is mostly addressed numerically.

More recently, Kebiche et al. [38] presented a numerical, geometrical nonlinear analysis of a quadruplex tensegrity unit (four-strut cylindrical tensegrity) under various load cases. Tran and Lee [42] studied nonlinear analysis of a quadruplex grid under vertical loads using both total and updated Lagrangian formulations. Nuhoglu and Korkmaz [43] proposed a practical approach for the nonlinear analysis problem. A Co-Rotational Method was developed to carry out geometrical nonlinear analyses by Faroughi and Lee [44].

On the other hand, detailed nonlinear analyses to study the behavior of a structure under external loads are usually expensive in terms of computational power and time. The larger the structure is, the more tedious are the analyses required. One solution to alleviate this difficulty is the use of continuum modeling. Long lattice or repeating structures or in this case, tensegrities, can be modeled as continuum beams, and their effective stiffness properties such as bending, torsional, and axial rigidities can be evaluated. Such effective stiffness properties permit analysis of the approximate behavior of tensegrity systems under external loads, and making a fair comparison between different structures.

Long lattice structures or repeating tensegrity booms can be modeled as three dimensional continuum beams. This reduces the number of degrees of freedom in the model, and the governing six parameters, called the effective stiffness properties, can be obtained, allowing for rapid and accurate estimation of the global behavior. These beam models contain the same amount of strain energy when deformed as the actual structure. This method is called energy equivalency, and a few variations have been developed and studied by many researchers.

Noor et al. [45] developed a symbolic method to obtain the total strain energy accumulated in a relatively simple repetitive three dimensional lattice structure under an assumed displacement field. Taylor series expansion along the longitudinal axis takes strain and strain gradients into consideration for a fairly accurate model. The variation of the displacement field assumption by Noor and Andersen [46] allowed them to account for warping and the distortion of cross-sections. Anisotropic stiffness properties are also considered in another study by Noor and Russell [47]. However, Noor abandoned his symbolic approach as he develops a numerical method [48] since more complex lattice structures require more computational power and exhibit anisotropic stiffness properties.

Dow et al. [49] developed a more general approach than Noor's in terms of displacement field assumptions. The displacements at each node in three different directions are approximated with a full cubic polynomial having 60 coefficients. This approximation is evaluated at the origin of the local coordinate system, and the coefficients are determined in terms of rigid body displacement, rotations, strains, and strain gradients. Then the procedure starts by isolating the repeating cell and developing a finite element model. A transformation matrix is used to relate nodal displacements to continuum displacements, which are used to express strain energy of the continuum model. Based solely on the configuration of the repeating cell, the number of coefficients is reduced by identifying the strain and/or strain gradients which cannot be exhibited by the structure; the equivalent stiffness properties are obtained through four transformation steps.

Kebiche et al. [50] follows Dow's work by applying their method to tensegrity structures by considering the pre-stress. The total strain energy is obtained by considering both elastic rigidity (linear portion) and initial self-stress (nonlinear portion). The initial selfstress levels are varied, and the change in effective stiffness properties is observed. Lee [51] developed a method which uses spectral elements to determine the effective stiffness properties of truss-type space structures. McCallen and Romstad [52] also use energy equivalency for a geometrically nonlinear two dimensional problem by developing an expression for the generalized stress.

In this chapter, mathematical formulations of the developed finite element model are derived. The solution method for static analyses under external loads is explained, and a numerical example taken from the literature is investigated. Dynamic analyses of tensegrity structures are also included in this chapter, and the free vibration problem is addressed. Then, continuum beam modeling for tensegrity structures is studied, and a nonlinear finite element validation procedure is provided.

3.1 Nonlinear Finite Element Model

The nonlinearity exhibited by tensegrity structures originates from two primary sources. The first one is the self-stress present in the structure. It contributes to the stiffness and, after the application of external loads, as the force distribution in the structure varies, the stiffness is affected. The second one is the large deformations and/or displacements that result when a large external load is applied. As the deformations and/or displacements occur, the nodal locations change, resulting in a change of length of elements which, in turn, affect stiffness. The effect of pre-stress appears linearly in the stiffness matrix; however, due to large displacements/rotations, it varies remarkably. Furthermore, material nonlinearity, which is not considered in this dissertation, is a different source that occurs when the strains of individual elements reach yield strain, and the transition from elastic to plastic response takes place.

Therefore, in order to capture possible critical transitions such as a cable going slack or substantial changes in stiffness levels due to large deformations and/or displacements that occur under applied external loads, an incremental iterative analysis with a modified Newton-Raphson method is crucial.

The developed nonlinear model for tensegrity structures is similar to truss structures except it includes geometric nonlinearity. The individual elements (either cables or struts) are modeled as one-dimensional space truss elements. An arbitrarily oriented space truss element is shown in Figure 3.1. The important assumptions for the developed nonlinear model are as follows:

- Materials are linear elastic.
- Elements carry solely axial loads.
- Cables and struts are capable of carrying only tension and compression, respectively (unilateral element behavior).

- Loads are applied at the nodes.

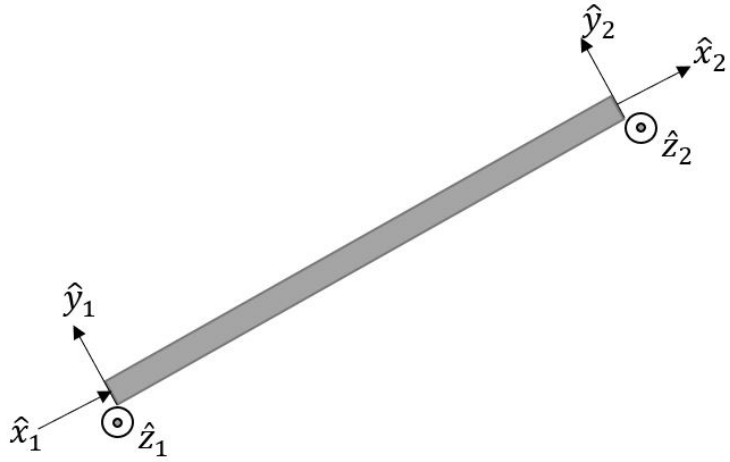

Figure 3.1: Two Noded Space Truss Element

The space truss element shown in Figure 3.1 has two nodes, one at each end, and the local axes are shown with $\hat{x}$, $\hat{y}$ and $\hat{z}$. Then, the strain energy of the space truss element is written as in Equation 3.1.

$$U_e = \frac{1}{2}\int_0^L \sigma_{\hat{x}}\varepsilon_{\hat{x}} A d\hat{x} \tag{3.1}$$

where L and A are the length and the cross-sectional area of the element, respectively. σ and ε are axial stress and strain quantities. The linear elastic material assumption gives a relationship between stress and strain as

$$\sigma_{\hat{x}} = E\varepsilon_{\hat{x}} \tag{3.2}$$

where E is the modulus of elasticity of the material. Substituting Equation 3.2 into 3.1 yields

$$U_e = \frac{1}{2}\int_0^L EA\varepsilon_{\hat{x}}^2 d\hat{x} \tag{3.3}$$

In order to account for large deformations and/or displacements, quadratic terms in the strain expression are retained. The axial strain is then written as

$$\varepsilon = \frac{\partial \hat{u}}{\partial \hat{x}} + \frac{1}{2}\Big[\Big(\frac{\partial \hat{u}}{\partial \hat{x}}\Big)^2 + \Big(\frac{\partial \hat{v}}{\partial \hat{x}}\Big)^2 + \Big(\frac{\partial \hat{w}}{\partial \hat{x}}\Big)^2\Big] \tag{3.4}$$

where $\hat{u}$, $\hat{v}$ and $\hat{w}$ are displacements in $\hat{x}$, $\hat{y}$ and $\hat{z}$ directions, respectively. The displacements $\hat{u}$, $\hat{v}$ and $\hat{w}$ linearly vary along the truss element and, therefore, the displacement derivatives in Equation 3.4 can be written in terms of the displacements as follows:

$$\begin{aligned}\frac{\partial\hat{u}}{\partial\hat{x}} &= \frac{\Delta\hat{u}}{\Delta\hat{x}} = \frac{\hat{x}_2-\hat{x}_1}{L}\\ \frac{\partial\hat{v}}{\partial\hat{x}} &= \frac{\Delta\hat{v}}{\Delta\hat{x}} = \frac{\hat{y}_2-\hat{y}_1}{L}\\ \frac{\partial\hat{w}}{\partial\hat{x}} &= \frac{\Delta\hat{w}}{\Delta\hat{x}} = \frac{\hat{z}_2-\hat{z}_1}{L}\end{aligned} \tag{3.5}$$

Equations 3.4 and 3.5 are substituted into Equation 3.3 and, ignoring the cubic and higher order terms, yields

$$U_e = \frac{1}{2}EAL\Big[\Big(\frac{\hat{x}_2-\hat{x}_1}{L}\Big)^2 + \frac{\partial\hat{u}}{\partial\hat{x}}\Big\{\Big(\frac{\hat{x}_2-\hat{x}_1}{L}\Big)^2 + \Big(\frac{\hat{y}_2-\hat{y}_1}{L}\Big)^2 + \Big(\frac{\hat{z}_2-\hat{z}_1}{L}\Big)^2\Big\}\Big] \tag{3.6}$$

Rearranging Equation 3.6 gives

$$U_e = \frac{1}{2}\frac{EA}{L}\Big[(\hat{x}_2-\hat{x}_1)^2 + \frac{\partial\hat{u}}{\partial\hat{x}}\Big\{(\hat{x}_2-\hat{x}_1)^2 + (\hat{y}_2-\hat{y}_1)^2 + (\hat{z}_2-\hat{z}_1)^2\Big\}\Big] \tag{3.7}$$

Additionally, the term $\partial\hat{u}/\partial\hat{x}$ in Equation 3.7 can be represented as

$$\frac{\partial\hat{u}}{\partial\hat{x}} \approx \varepsilon_{\hat{x}} = \frac{\sigma_{\hat{x}}}{E} = \frac{T}{EA} \tag{3.8}$$

where T is the pre-stress force in the element. T is always positive for a cable in tension. As a result, the strain energy of the two-noded space truss element is written in the following form:

$$U_e = \frac{1}{2}\frac{EA}{L}(\hat{x}_2-\hat{x}_1)^2 + \frac{1}{2}\frac{T}{L}\Big\{(\hat{x}_2-\hat{x}_1)^2 + (\hat{y}_2-\hat{y}_1)^2 + (\hat{z}_2-\hat{z}_1)^2\Big\} \tag{3.9}$$

Defining a nodal displacement vector as $\bar{\mathbf{q}} = \{\hat{x}_1, \hat{y}_1, \hat{z}_1, \hat{x}_2, \hat{y}_2, \hat{z}_2\}^T$, the quadratic terms found in Equation 3.9 can be represented in the following manner:

$$(\hat{x}_2 - \hat{x}_1)^2 = (\hat{x}_2 - \hat{x}_1)^T(\hat{x}_2 - \hat{x}_1) = \bar{\mathbf{q}}^T \begin{Bmatrix} -1 \\ 0 \\ 0 \\ 1 \\ 0 \\ 0 \end{Bmatrix} \begin{Bmatrix} -1 & 0 & 0 & 1 & 0 & 0 \end{Bmatrix} \bar{\mathbf{q}} \tag{3.10}$$

$$(\hat{x}_2 - \hat{x}_1)^2 = \begin{bmatrix} 1 & 0 & 0 & -1 & 0 & 0 \\ 0 & 0 & 0 & 0 & 0 & 0 \\ 0 & 0 & 0 & 0 & 0 & 0 \\ -1 & 0 & 0 & 1 & 0 & 0 \\ 0 & 0 & 0 & 0 & 0 & 0 \\ 0 & 0 & 0 & 0 & 0 & 0 \end{bmatrix} \tag{3.11}$$

Similarly for $\hat{y}$ and $\hat{z}$ directions

$$(\hat{y}_2 - \hat{y}_1)^2 = \begin{bmatrix} 0 & 0 & 0 & 0 & 0 & 0 \\ 0 & 1 & 0 & 0 & -1 & 0 \\ 0 & 0 & 0 & 0 & 0 & 0 \\ 0 & 0 & 0 & 0 & 0 & 0 \\ 0 & -1 & 0 & 0 & 1 & 0 \\ 0 & 0 & 0 & 0 & 0 & 0 \end{bmatrix} \tag{3.12}$$

$$(\hat{z}_2 - \hat{z}_1)^2 = \begin{bmatrix} 0 & 0 & 0 & 0 & 0 & 0 \\ 0 & 0 & 0 & 0 & 0 & 0 \\ 0 & 0 & 1 & 0 & 0 & -1 \\ 0 & 0 & 0 & 0 & 0 & 0 \\ 0 & 0 & 0 & 0 & 0 & 0 \\ 0 & 0 & -1 & 0 & 0 & 1 \end{bmatrix} \tag{3.13}$$

Substituting Equations 3.11, 3.12 and 3.13 into Equation 3.9 yields the final form of the strain energy.

$$U_e = \frac{1}{2}\bar{\mathbf{q}}^T\bar{\mathbf{K}}_L\bar{\mathbf{q}} + \frac{1}{2}\bar{\mathbf{q}}^T\bar{\mathbf{K}}_{NL}\bar{\mathbf{q}} \tag{3.14}$$

where $\bar{\mathbf{K}}_L$ and $\bar{\mathbf{K}}_{NL}$ are the linear and geometric stiffness matrices [38,41,42] respectively, with respect to local coordinates. The linear stiffness matrix results from the axial stiffness of the element while the geometric stiffness matrix is a result of the pre-stress in the structure. Their expressions are given as follows:

$$\bar{\mathbf{K}}_L = \frac{EA}{L}\begin{bmatrix} 1 & 0 & 0 & -1 & 0 & 0 \\ 0 & 0 & 0 & 0 & 0 & 0 \\ 0 & 0 & 0 & 0 & 0 & 0 \\ -1 & 0 & 0 & 1 & 0 & 0 \\ 0 & 0 & 0 & 0 & 0 & 0 \\ 0 & 0 & 0 & 0 & 0 & 0 \end{bmatrix} \tag{3.15}$$

$$\bar{\mathbf{K}}_{NL} = \frac{T}{L}\begin{bmatrix} 1 & 0 & 0 & -1 & 0 & 0 \\ 0 & 1 & 0 & 0 & -1 & 0 \\ 0 & 0 & 1 & 0 & 0 & -1 \\ -1 & 0 & 0 & 1 & 0 & 0 \\ 0 & -1 & 0 & 0 & 1 & 0 \\ 0 & 0 & -1 & 0 & 0 & 1 \end{bmatrix} \tag{3.16}$$

The geometric stiffness matrix shows the effect of pre-stress, and it is “isotropic” at each node [53,54]. Przemieniecki [55] suggests employing an approximation of large deformation with “moderate rotation” since it is more economical in terms of computational time. This approximation modifies the geometric stiffness matrix by eliminating the displacements in local $\hat{x}$ direction caused by pre-stress. However, considering the computational power of modern computers, this precaution is not necessary.

The stiffness matrices are expressed with respect to local coordinates. In order to obtain the full stiffness matrix of the assemblage of the elements, local coordinates, $\bar{\mathbf{q}}$, need to be expressed in terms of global coordinates $\mathbf{q}$. This is achieved via transformation matrices. The relationship between local and global coordinates can be formed as

$$\bar{\mathbf{q}} = \mathbf{T}\mathbf{q} \tag{3.17}$$

where $\mathbf{T}$ is the transformation matrix as given below

$$\mathbf{T} = \begin{bmatrix} l_1 & m_1 & n_1 & 0 & 0 & 0 \\ l_2 & m_2 & n_2 & 0 & 0 & 0 \\ l_3 & m_3 & n_3 & 0 & 0 & 0 \\ 0 & 0 & 0 & l_1 & m_1 & n_1 \\ 0 & 0 & 0 & l_2 & m_2 & n_2 \\ 0 & 0 & 0 & l_3 & m_3 & n_3 \end{bmatrix} \tag{3.18}$$

The direction cosines in the first and fourth rows of the transformation matrix are given as

$$\begin{aligned} l_1 &= \frac{x_2 - x_1}{L} \\ m_1 &= \frac{y_2 - y_1}{L} \\ n_1 &= \frac{z_2 - z_1}{L} \end{aligned} \tag{3.19}$$

where x, y and z are the global nodal coordinates. For space truss elements, the other direction cosines are unimportant since they do not appear in the final expression of the stiffness matrix. Similarly, the applied external forces in local coordinates can be expressed by the forces in global coordinates.

$$\bar{\mathbf{P}} = \mathbf{TP} \tag{3.20}$$

where $\bar{\mathbf{P}}$ and $\mathbf{P}$ are the external load vectors in local and global coordinates. For a typical structural system, the displacement-force relationship in local coordinates is written by the stiffness equation as follows:

$$\bar{\mathbf{P}} = \bar{\mathbf{K}}\bar{\mathbf{q}} \tag{3.21}$$

Substitution of Equation 3.17 and 3.20 into Equation 3.21 yields

$$\mathbf{TP} = \bar{\mathbf{K}}\mathbf{Tq} \tag{3.22}$$

By rearranging,

$$\mathbf{P} = \mathbf{T}^{-1}\bar{\mathbf{K}}\mathbf{Tq} \tag{3.23}$$

Transformation matrices are orthogonal matrices with the property of, $\mathbf{T}^{-1} =$

$\mathbf{T}^T$. Therefore,

$$\mathbf{P} = \mathbf{T}^T \bar{\mathbf{K}} \mathbf{T} \mathbf{q} \tag{3.24}$$

As a result, the stiffness matrix in terms of global coordinates is defined as follows:

$$\mathbf{K} = \mathbf{T}^T \bar{\mathbf{K}} \mathbf{T} \tag{3.25}$$

Both the linear and geometric stiffness matrices of individual elements need to be represented in nodal coordinates associated with global axes, using transformation matrices. After the transformation into the global coordinate system, the linear and geometric stiffness matrices are summed to obtain the overall stiffness matrix of the element, which is known as the *tangent stiffness matrix*. Then, the traditional finite element assembly process can be carried out to compute the global stiffness matrix.

$$\mathbf{K}_T = \mathbf{K}_L + \mathbf{K}_{NL} \tag{3.26}$$

One important thing to note here is that the geometric stiffness matrix is invariant to transformation and, therefore, application of Equation 3.25 is not required.

$$\mathbf{K}_{NL} = \bar{\mathbf{K}}_{NL} \tag{3.27}$$

Additionally, since the space truss element is pre-stressed, an internal force vector is generated. As a result of the pre-stress, the element internal force vector with respect to local coordinates can be written as

$$\bar{\mathbf{F}} = T \begin{Bmatrix} -1 & 0 & 0 & 1 & 0 & 0 \end{Bmatrix} \tag{3.28}$$

The internal force vector can be transformed to global coordinates with the same transformation matrix $\mathbf{T}$ as follows

$$\mathbf{F} = \mathbf{T}^T \bar{\mathbf{F}} \tag{3.29}$$

Similar to assembly of the global stiffness matrix, the global internal force vector can be assembled. Under no external load, the internal force vector generates a null vector, since tensegrity structures are self-equilibrated with pre-stress.

Additionally, the consistent mass matrix of the space truss element is written as in Equation 3.30. Many studies address its derivation and, therefore, it is not given here [55, 56].

$$\bar{\mathbf{M}} = \frac{\rho A L}{6} \begin{bmatrix} 2 & 0 & 0 & 1 & 0 & 0 \\ 0 & 2 & 0 & 0 & 1 & 0 \\ 0 & 0 & 2 & 0 & 0 & 1 \\ 1 & 0 & 0 & 2 & 0 & 0 \\ 0 & 1 & 0 & 0 & 2 & 0 \\ 0 & 0 & 1 & 0 & 0 & 2 \end{bmatrix} \tag{3.30}$$

The element mass matrix is also referred to local coordinates. The coordinates can be transformed to the global coordinates by the transformation matrix given in Equation 3.18. The element mass matrix in global coordinates is calculated as

$$\mathbf{M} = \mathbf{T}^T \bar{\mathbf{M}} \mathbf{T} \tag{3.31}$$

However, similar to the geometric stiffness matrix, the element mass matrix of the space truss element is also invariant to transformation of coordinates [55, 56] and, therefore, it is not required to use Equation 3.31. Analogously, the global mass matrix of the structure can be constructed by assembling the element mass matrices.

3.2 Static Analyses Under External Loads

Study of deflections or the behavior of tensegrity structures under external loads requires a nonlinear solution method. Due to applied external loads, the structure may undergo large deformations and/or displacements, resulting in substantial changes in the stiffness level of the structure. At some load levels, cables may also go slack, decreasing the stiffness of the structure, or the force distribution in the structure may change considerably, affecting stiffness.

In order to account for such cases, the nonlinear static problem is investigated using an incremental iterative analysis with the Newton-Raphson method. The applied loads are increased iteratively, and the solution is obtained for each iteration. The stiffness matrix of the structure is recalculated based on the deformed geometry.

The nonlinear force-displacement relationship can be written as follows:

$$\mathbf{K}_T \Delta \mathbf{U} = \mathbf{P} - \mathbf{F} \tag{3.32}$$

where $\mathbf{K}_T$ is the tangent stiffness matrix of the structure, $\Delta\mathbf{U}$ is the displacement vector, $\mathbf{P}$ is the external load vector, and $\mathbf{F}$ is the internal load vector due to pre-stress.

In more detail, the static analyses of tensegrity structures under external loads consist of iterations and sub-iterations in which the stiffness matrix of the structure is continuously recalculated. In each iteration, external forces are increased while in each sub-iteration, convergence is sought. The analysis starts with calculating the tangent stiffness matrix and the internal force vector (initially null). Then a fraction of the external loads is applied, starting the first iteration. During each iteration, the system given in Equation 3.32 is solved for $\Delta\mathbf{U}$, and the nodal coordinates are updated. Based on updated nodal coordinates, the stiffness matrix and internal force vector are recalculated. Then force balance at each node is checked by controlling the norm of the right-hand side of Equation 3.32. These steps are called sub-iterations. If force balance is satisfied at each node, called *convergence*, then the sub-iterations end, and the analysis moves on to next iteration. The solution method can be clarified with the following procedure.

Procedure:

- Step 0: Calculate the tangent stiffness matrix and internal force vector
- Step 1: Increase the applied load and calculate the external load vector
- Step 2: Solve Equation 3.32 and obtain the $\Delta\mathbf{U}$ vector
- Step 3: Update nodal locations using the $\Delta\mathbf{U}$ vector
- Step 4: Update the pre-stress force using the linear elastic material assumption
- Step 5: Calculate the tangent stiffness matrix and the internal force vector
- Step 6: Check convergence

1. $norm(\mathbf{P} - \mathbf{F}) < tolerance$, go to Step 1
2. $norm(\mathbf{P} - \mathbf{F}) \geq tolerance$, go to Step 2

The procedure ends when the applied load reaches the actual external load value. In the procedure, Step 0 is the initialization process, Steps 1 to 6 refer to an iteration, and Steps 3 to 6 represent a sub-iteration.

Calculation of the tangent stiffness matrix and internal force vector were explained in the previous section. Increasing the applied load can be achieved in different ways. The most commonly employed way divides the actual external load by a total number of iterations, and in each iteration, the applied load is increased by that value. Nodal locations are updated using Equation 3.33, in which $\mathbf{U}$ is the nodal locations vector.

$$\mathbf{U} = \mathbf{U} + \Delta\mathbf{U} \tag{3.33}$$

The pre-stress force can be updated for the deformed geometry using Hooke's Law for linear elastic materials [44]. During the initialization process, the rest length of the members should be computed. To do so, after the selection of pre-stress coefficient, P_s, a relationship can be written as

$$P_s q_i L_i = f_i = \frac{E_i A_i}{L_{0,i}}(L_i - L_{0,i}) \tag{3.34}$$

The relationship given in Equation 3.34 is analogous to application of Hooke's law to linear springs, $f = kx$. Subscript i indicates the individual elements, and the term $E_i A_i / L_{0,i}$ is the axial stiffness of the element. $L_{0,i}$ is the rest length of the element, the length at which the element carries no pre-stress. Therefore, $L_i - L_{0,i}$ represents how much the element is deformed. Equation 3.34 can be solved for the rest length of the elements as follows:

$$L_{0,i} = \frac{E_i A_i L_i}{E_i A_i + f_i} = \frac{E_i A_i L_i}{E_i A_i + P_s q_i L_i} \tag{3.35}$$

Equation 3.35 expresses the rest length of the i^{th} element in terms of its axial stiffness, cross-sectional area, and initially designed pre-stress. The rest length of the elements are calculated from the initial geometry and, as deformation occurs under external loads, the pre-stress force variations can be calculated with Equation 3.34.

Additionally, the possibility of cable slackness is treated in the following way. In each subiteration, individual lengths of the elements are calculated and, if the length of a cable reaches a value lower than its rest length, the cable becomes slack. Then, the pre-stress force in this cable is set to zero, $f_i = 0$, as well as the axial stiffness, $E_i A_i = 0$. As long as the length of the cable is shorter than its actual rest length, the pre-stress and the axial stiffness remain this way since the cable has no contribution to stiffness, either linear or geometrical.

Numerical Example

The procedure described for static analyses of tensegrity structures under external loads is applied to a quadruplex unit, which is a tensegrity structure with four struts. The geometry of the quadruplex unit is shown in Figure 3.2. This example problem was studied by Kebiche et al. [38], Tran and Lee [42], and Faroughi and Lee [44].

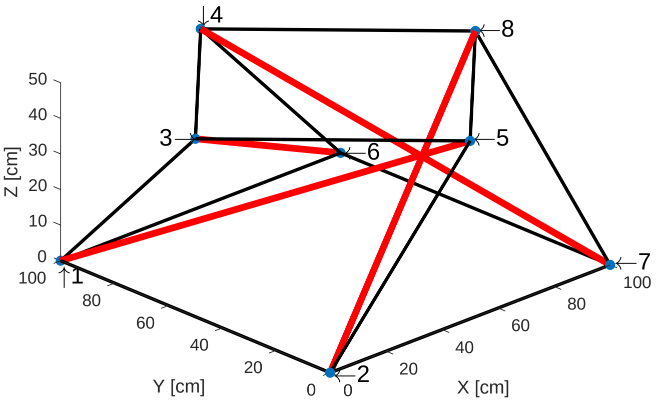

Figure 3.2: Four-Strut Tensegrity Unit - Quadruplex

The structure has square cross-sections at the bottom and top planes, which are parallel to each other. The node locations and the connectivity information are given in Tables 3.1 and 3.2.

The quadruplex unit consists of 12 cables (black lines) and 4 struts (red lines). In order to determine the force-density vector, the force finding method is used since the nodal locations and the connectivity are defined. The pre-stress coefficient

Table 3.1: Node locations

Nodes	x	y	z	Nodes	x	y	z
1	0	100	0	5	50	0	50
2	0	0	0	6	100	100	0
3	0	50	50	7	100	0	0
4	50	100	50	8	100	50	50

is selected as, P_s =55 N/cm. The force-density vector and the initial pre-stress forces in each element are given in Table 3.2.

Table 3.2: Element Connectivity and Properties

Element	Node 1	Node 2	Element Type	Force Density	Length / Rest Length [cm]	Initial Force [N]
1	1	6	Bottom Cables	1	100 / 99.51	5500
2	2	7		1	100 / 99.51	5500
3	1	2		1	100 / 99.51	5500
4	6	7		1	100 / 99.51	5500
5	3	4	Top Cables	2	70.71 / 70.22	7778.17
6	3	5		2	70.71 / 70.22	7778.17
7	4	8		2	70.71 / 70.22	7778.17
8	5	8		2	70.71 / 70.22	7778.17
9	2	5	Vertical Cables	2	70.71 / 70.22	7778.17
10	7	8		2	70.71 / 70.22	7778.17
11	4	6		2	70.71 / 70.22	7778.17
12	1	3		2	70.71 / 70.22	7778.17
13	3	6	Struts	-2	122.47 / 122.73	-13472.19
14	2	8		-2	122.47 / 122.73	-13472.19
15	1	5		-2	122.47 / 122.73	-13472.19
16	4	7		-2	122.47 / 122.73	-13472.19

The cross-sectional areas of cables and struts were chosen as 0.28 cm^2 and 0.325 cm^2, respectively. The elasticity modulus of cables and struts are 40 GPa and 200 GPa, respectively. Node 1 is completely fixed, node 2 is restricted in the x and z directions, while node 3 is only restricted in the x direction. Then, $P = \pm 2\ kN$ nodal forces are applied at nodes 6, 7 and 8 in the x direction. These cases are referred to as traction and compression, respectively.

Figure 3.3 shows the analysis results for both cases in terms of average displacements of nodes 6, 7 and 8 in the x direction versus the applied loads ($3P$). The results provided by Kebiche et al. [38] are also included in the same figure, showing the validity of the results and modeling approach. The solid lines indicate the compression case while the dashed lines represent the traction case.

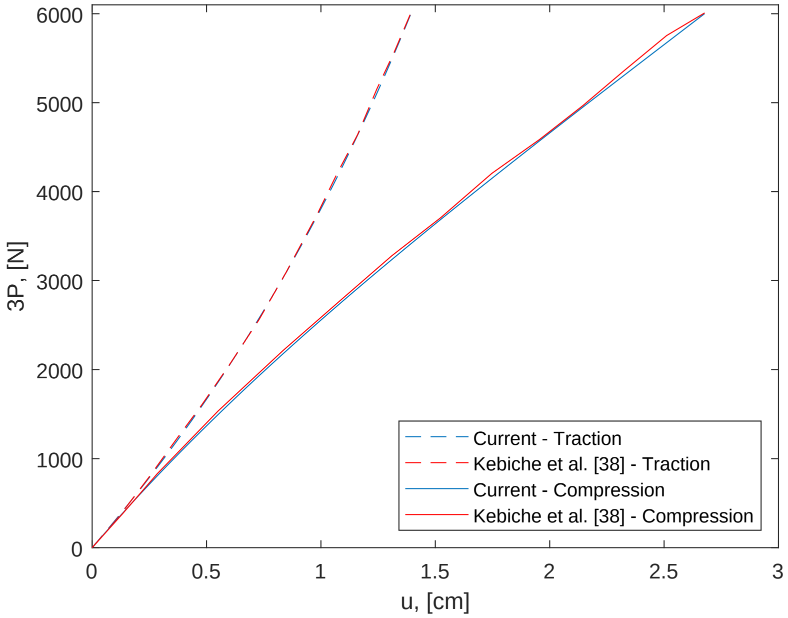

Figure 3.3: Behavior of the quadruplex unit under traction and compression

The structure responds to the traction and compression loads quite differently due to its nonlinear nature. As the applied traction loads are increased, the structure becomes stiffer due to increased pre-stress which affects the geometric stiffness matrix. On the other hand, under the applied compression loads, the structure becomes softer as the level of pre-stress forces in the members decrease. These effects are known as “stiffening” and “softening”. The slopes of the solutions given in Figure 3.3 are identical in the beginning for applied small loads. However, as the loads are increased, the two solutions differ substantially from each other. Based on these findings, it can be said that the quadruplex unit shows “anisotropic behavior” [38].

3.3 Free Vibration Problem

Dynamic behavior of tensegrity structures is of great importance for deployable boom designs. Under dynamic disturbances, deployable booms should maintain stability and not exceed allowable deformation limits given for the mission. Resonance effects must be avoided, and any dynamic couplings must be prevented. Therefore, the dynamic behavior of tensegrity structures plays a crucial role on the overall performance of spacecraft and should be investigated carefully.

Modal analyses can be conducted to study the dynamic behavior of tensegrity structures. Considering harmonic motion in the form of $\mathbf{x} = \mathbf{X}e^{i\omega t}$, the generalized eigenvalue problem can be written as follows:

$$\mathbf{K}_T\mathbf{X} = \omega^2\mathbf{M}\mathbf{X} \tag{3.36}$$

where $\mathbf{x}$ is the nodal displacements, $\mathbf{X}$ is the amplitude, and ω is the angular frequency of the system. The tangent stiffness matrix and the mass matrix defined by Equations 3.26 and 3.31 are utilized for the modal analyses.

Since tensegrity structures often kinematically indeterminate, infinitesimal mechanisms may be present and affect the dynamic behavior. The infinitesimal modes typically exhibit very low natural frequencies compared to other vibration modes. Additionally, infinitesimal mechanisms are stiffened by pre-stress, and the corresponding vibration modes are susceptible to changes with the level of pre-stress. More specifically, it has been found that the associated natural frequencies increase proportionally to the square root of the level of pre-stress [53, 54]. Higher vibration modes are governed by the axial stiffness of individual members, and they are not as affected by the pre-stress as infinitesimal mechanism modes are.

Numerical Example

Modal analyses are conducted for a triplex unit shown in Figure 3.4. The height and the radius of the structure are chosen as 1 m. All the cables and struts are assumed to be made of steel with modulus of elasticity and density of $E = 200$ GPa and $\rho = 7860$ kg/m^3, respectively. The cables have solid circular cross-section with radius of 0.001 m, and the struts are hollow-shaped with outer and inner radii of 0.015 m and 0.01 m, respectively.

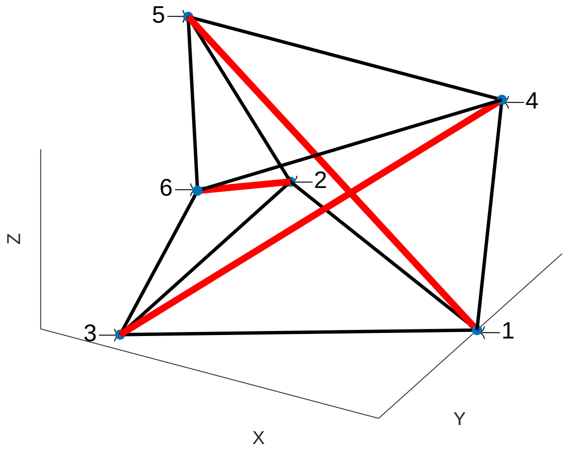

Figure 3.4: Triplex Unit

The pre-stress values in the struts are varied between 0.4 MPa and 2 MPa and the natural frequencies are obtained for six modes. The natural frequencies of the triplex unit are tabulated and given in Table 3.3.

Table 3.3: Natural Frequencies of Triplex Unit

Pre-stress [MPa]	First Mode [Hz]	Second Mode [Hz]	Third Mode [Hz]	Fourth Mode [Hz]	Fifth Mode [Hz]	Sixth Mode [Hz]
0.4	1.0549	34.9923	34.9923	68.4403	68.4403	74.3909
0.8	1.4918	35.0036	35.0036	68.4487	68.4487	74.3947
1.2	1.8271	35.0148	35.0148	68.4570	68.4570	74.3985
1.6	2.1097	35.0261	35.0261	68.4654	68.4654	74.4023
2	2.3586	35.0373	35.0373	68.4738	68.4738	74.4061

Table 3.3 shows the natural frequencies. The first vibration mode is an infinitesimal mechanism mode, and its natural frequency is very low compared to the other modes. The natural frequency associated with this mode is also found to increase proportionally with the square root of the level of pre-stress. The other modes are not affected very much by the level of pre-stress. Furthermore, the second and the third modes and the fourth and the fifth modes are the same vibration modes in different directions, respectively. The corresponding mode shapes are shown in Figures 3.5, 3.6, 3.7, and 3.8.

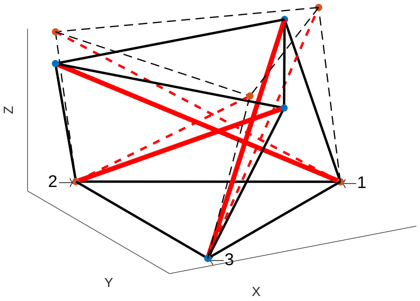

Figure 3.5: First mode

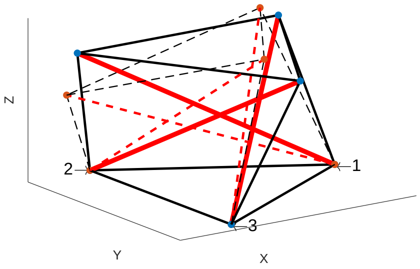

Figure 3.6: Second mode

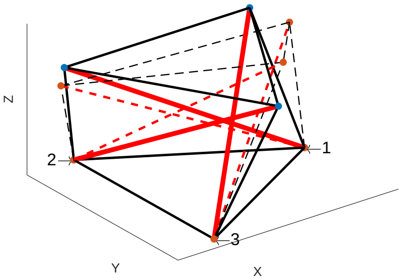

Figure 3.7: Fourth mode

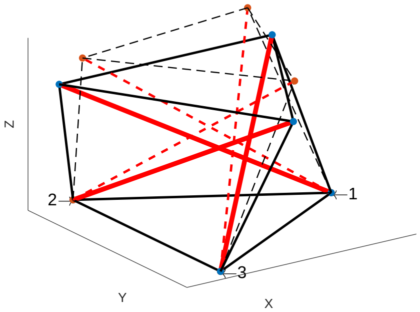

Figure 3.8: Sixth mode

3.4 Effective Stiffness Properties of Tensegrity Booms

A fair comparison between deployable booms in terms of stiffness can be achieved by evaluating the effective stiffness properties of the structures such as bending, torsional, and axial rigidity. Continuum beam models which contain the same amount of strain energy when deformed as tensegrity booms can be obtained. This method is called *energy equivalency*, and a few variations which implement symbolic and numerical approaches for truss structures have been developed. The symbolic approaches are abandoned by researchers since they are not effective when dealing with a complex lattice structure. This led to numerical approaches thanks to high available computational power.

The symbolic approaches start with a displacement field assumption of the cross-section in terms of rigid body motion and rotation, and strain terms. Employing small strain assumptions leads to strain components. The axial strain in each member in the structure can be derived from the strain components, and they are expanded into a Taylor series along the longitudinal axis in order to generate a fairly accurate model. Then strain energy is written in terms of strain and strain gradient terms, and conditions on zero energy local deformations within structure are imposed. As a result, the strain energy is represented in terms of the fundamental strain terms exhibited by a three dimensional beam. The coefficients of the fundamental strain terms yield the effective stiffness properties as shown by Noor [45, 46].

A numerical approach developed by Dow et al. [49] uses a generalized version of Noor's displacement field. The displacement field assumption consists of 60 coefficients which are obtained in terms of rigid body displacements, rotations, strains, and strain gradients by evaluating the displacement field assumptions at the origin of the structure. Effective stiffness properties are constant throughout the lattice structure and, therefore, the smallest repeating cell is isolated. A finite element model is developed and four transformation matrices are used to reduce the size of the stiffness matrix to the size of a three dimensional beam's. The terms found in the reduced stiffness matrix are identified as effective stiffness properties and associated coupling terms [47, 48]. Application of Dow's numerical approach to tensegrity structures is achieved by Kebiche et al. [50] considering pre-stress. The influence of pre-stress is introduced by using the geometric stiffness matrix derived previously.

In this section, Dow's numerical approach is explained, and a simple method is developed to determine the effective stiffness properties of tensegrity booms. The method developed here reduces the number of transformations rather than going through four transformation steps.

3.4.1 Energy Equivalency Method

The energy equivalency method developed by Dow et al. [49] starts with an approximation of displacement field in three different directions to determine effective stiffness properties. In Dow's previous work [49], these extensive displacement field assumptions are given as follows:

$$\begin{aligned} u(x,y,z) = u + \varepsilon_x x + \Big(\frac{1}{2}\gamma_{xy} - r\Big)y + \Big(\frac{1}{2}\gamma_{xz} + q\Big)z + \frac{1}{2}\varepsilon_{x,x}x^2 + \varepsilon_{x,y}xy \\ +\varepsilon_{x,z}xz + \frac{1}{2}\Big(\gamma_{xy,y} - \varepsilon_{y,x}\Big)y^2 + \frac{1}{2}\Big(\gamma_{xy,z} - \gamma yz, x + \gamma xz, y\Big)yz + \frac{1}{2}\Big(\gamma_{xz,z} - \varepsilon_{z,x}\Big)z^2 \\ +\frac{1}{6}\varepsilon_{x,xx}x^3 + \frac{1}{2}\varepsilon_{x,xy}x^2y + \frac{1}{2}\varepsilon_{x,xz}x^2z + \frac{1}{6}\Big(\gamma_{xy,yy} - \varepsilon_{y,xy}\Big)y^3 + \frac{1}{2}\Big(\varepsilon_{x,yy}\Big)y^2x \\ +\frac{1}{2}\Big(\gamma_{xy,yz} - \varepsilon_{y,xz}\Big)y^2z + \frac{1}{6}\Big(\gamma_{xz,zz} - \varepsilon_{z,xz}\Big)z^3 + \frac{1}{2}\varepsilon_{x,zz}z^2x + \frac{1}{2}\Big(\gamma_{xz,yz} - \varepsilon_{z,xy}\Big)z^2y \\ +\varepsilon_{x,yz}xyz \end{aligned} \tag{3.37}$$

$$\begin{aligned} v(x,y,z) = v + \Big(\gamma_{xy} - r\Big)x + \varepsilon_y y + \Big(\frac{1}{2}\gamma_{yz} - p\Big)z + \frac{1}{2}\Big(\gamma_{xy,x} - \varepsilon_{x,y}\Big)x^2 + \varepsilon_{y,x}xy \\ +\frac{1}{2}\Big(\gamma_{xy,z} + \gamma_{yz,x} - \gamma_{xz,y}\Big)xz + \frac{1}{2}\varepsilon_{y,y}y^2 + \varepsilon_{y,z}yz + \frac{1}{2}\Big(\gamma_{yz,z} - \varepsilon_{z,y}\Big)z^2 \\ +\frac{1}{6}\Big(\gamma_{xy,xx} - \varepsilon_{x,xy}\Big)x^3 + \frac{1}{2}\varepsilon_{y,xx}x^2y + \frac{1}{2}\Big(\gamma_{xy,xz} - \varepsilon_{x,yz}\Big)x^2z + \frac{1}{6}\varepsilon_{y,yy}y^3 + \frac{1}{2}\varepsilon_{y,xy}y^2x \\ +\frac{1}{2}\varepsilon_{y,yz})y^2z + \frac{1}{6}\Big(\gamma_{yz,zz} - \varepsilon_{z,yz}\Big)z^3 + \frac{1}{2}\Big(\gamma_{yz,xz} - \varepsilon_{z,xy}\Big)z^2x + \frac{1}{2}\varepsilon_{y,zz}z^2y + \varepsilon_{y,xz}xyz \end{aligned} \tag{3.38}$$

$$\begin{aligned} w(x,y,z) = w + \Big(\gamma_{xz} - q\Big)x + \Big(\frac{1}{2}\gamma_{yz} + p\Big)y + \varepsilon_z z + \frac{1}{2}\Big(\gamma_{xz,x} - \varepsilon_{x,z}\Big)x^2 \\ +\frac{1}{2}\Big(-\gamma_{xy,z} + \gamma_{yz,x} + \gamma_{xz,y}\Big)xy + \varepsilon_{z,x}xz + \frac{1}{2}\Big(\gamma_{yz,y} - \varepsilon_{y,z}\Big)y^2 + \varepsilon_{z,y}yz + \frac{1}{2}\varepsilon_{z,z}z^2 \\ +\frac{1}{6}\Big(\gamma_{xz,xx} - \varepsilon_{x,xz}\Big)x^3 + \frac{1}{2}\Big(\gamma_{xz,xy} - \varepsilon_{x,yz}\Big)x^2y + \frac{1}{2}\varepsilon_{z,xx}x^2z + \frac{1}{6}\Big(\gamma_{yz,yy} - \varepsilon_{y,yz}\Big)y^3 \\ +\frac{1}{2}\Big(\gamma_{yz,xy} - \varepsilon_{y,xz}\Big)y^2x + \frac{1}{2}\varepsilon_{z,yy})y^2z + \frac{1}{6}\varepsilon_{z,zz}z^3 + \frac{1}{2}\varepsilon_{z,xz}z^2x + \frac{1}{2}\varepsilon_{z,yz}z^2y + \varepsilon_{z,xy}xyz \end{aligned} \tag{3.39}$$

where u is the displacement in axial direction, and v and w are the displacements in lateral directions. The axial and lateral directions are shown on a long boom in Figure 3.9.

Dow suggests an application of four transformations to the global stiffness

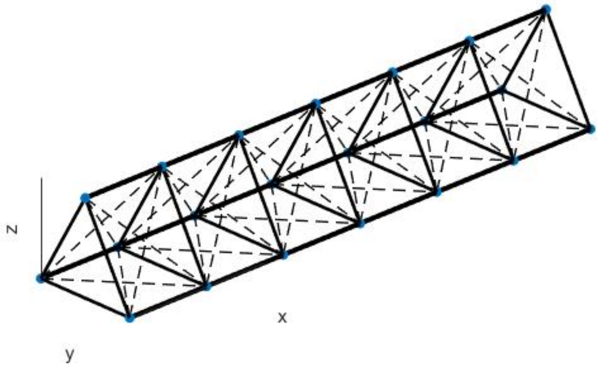

Figure 3.9: Axes shown on a long boom

matrix of the repeating cell. These transformations reduce the stiffness matrix to 6×6, which is represented in terms of the fundamental strains that govern the motion of a three dimensional beam. The final form is given as:

$$\begin{bmatrix} N \\ M_y \\ M_z \\ V_y \\ V_z \\ M_x \end{bmatrix} = \begin{bmatrix} EA & c_{12} & c_{13} & c_{14} & c_{15} & c_{16} \\ c_{12} & EI_y & c_{23} & c_{24} & c_{25} & c_{26} \\ c_{13} & c_{23} & EI_z & c_{34} & c_{35} & c_{36} \\ c_{14} & c_{24} & c_{34} & GA_y & c_{45} & c_{46} \\ c_{15} & c_{25} & c_{35} & c_{45} & GA_z & c_{56} \\ c_{15} & c_{26} & c_{36} & c_{46} & c_{56} & GJ \end{bmatrix} \begin{bmatrix} \varepsilon_x^0 \\ k_y^0 \\ k_z^0 \\ \gamma_{xy} \\ \gamma_{xz} \\ k_t^0 \end{bmatrix} \tag{3.40}$$

where EA, EI_y, EI_z, GA_y, GA_z, and GJ are the effective stiffness properties while the c_{ij}'s are the coupling terms. N, M_y, M_z, V_y, V_z, and M_x are the axial force, bending moments in y and z axes, shear forces in y and z axes, and torsional moment. On the other hand, ε_x^0, k_y^0, k_z^0, γ_{xy}^0, γ_{xz}^0, and k_t^0 denote the longitudinal strain, bending curvatures, transverse shear strains, and twist. For a symmetrical beam (zero couplings), the strain energy per unit length can be computed as

$$U = \frac{1}{2}EA(\varepsilon_x^0)^2 + \frac{1}{2}EI_y(k_y^0)^2 + \frac{1}{2}EI_z(k_z^0)^2 + \frac{1}{2}GA_y(\gamma_{xy}^0)^2 + \frac{1}{2}GA_z(\gamma_{xz}^0)^2 + \frac{1}{2}GJ(k_t^0)^2 \tag{3.41}$$

where

$$k_y^0 = \varepsilon_{x,y}; \qquad k_z^0 = \varepsilon_{x,z}; \qquad k_t^0 = \frac{1}{2}(\gamma_{xy,z} - \gamma_{xz,y}) \tag{3.42}$$

Kebiche et al. [50] noted that the total strain energy of a pre-stressed and pin-jointed structure can be written as

$$U = \frac{1}{2}\{u\}^T[K_T]\{u\} \tag{3.43}$$

where $\{u\}$ is the nodal displacement vector. The nodal displacement vector needs to be transformed into continuum displacement parameters, which are found in Equations 3.40 and 3.41. A transformation matrix, T_1 $(3k \times 60)$ is formed by the displacement field assumptions to achieve this transformation where k is the number of nodes. The first transformation is given as

$$\{u\} = [T_1]\{u\}_\varepsilon \tag{3.44}$$

The total strain energy in terms of the continuum strain vector $\{u\}_\varepsilon$ is

$$U = \frac{1}{2}\{u\}_\varepsilon^T[T_1]^T[K_T][T_1]\{u\}_\varepsilon \tag{3.45}$$

The second transformation, T_2, reduces the number of variables (strains and strain gradients) found in the continuum strain vector $\{u\}_\varepsilon$. This elimination depends solely on the configuration of the structure. Some parameters may not be exhibited by the structure or they may be linearly dependent. Identification of these parameters may be confusing - yet is crucial - and two methods are explained by Dow et al. [49]. The second transformation is given as

$$\{u\}_\varepsilon = [T_2]\{\mu\}_\varepsilon \tag{3.46}$$

where $\{\mu\}_\varepsilon$ is the reduced continuum strain vector. Then, the total strain energy can be expressed in terms of $\{\mu\}_\varepsilon$:

$$U = \frac{1}{2}\{\mu\}_\varepsilon^T[T_2]^T[T_1]^T[K_T][T_1][T_2]\{\mu\}_\varepsilon \tag{3.47}$$

The third transformation reorders the variables and creates two groups in the reduced continuum vector $\{\mu\}_\varepsilon$. It locates the fundamental strain terms to the first six rows while the order of the remaining variables is arbitrary. Therefore, the third transformation matrix $[T_3]$ has to be created somewhat manually for each configuration and may be tedious. The third transformation is given as

$$\{\mu\}_\varepsilon = [T_3] \begin{Bmatrix} \alpha \\ \beta \end{Bmatrix}_\varepsilon \tag{3.48}$$

where α is 6×1 vector which consists of the fundamental strain terms found in Equations 3.40 and 3.41. The total strain energy is

$$U = \frac{1}{2} \begin{Bmatrix} \alpha \\ \beta \end{Bmatrix}_\varepsilon^T [T_3]^T [T_2]^T [T_1]^T [K_T][T_1][T_2][T_3] \begin{Bmatrix} \alpha \\ \beta \end{Bmatrix}_\varepsilon = \frac{1}{2} \begin{Bmatrix} \alpha \\ \beta \end{Bmatrix}_\varepsilon^T [S] \begin{Bmatrix} \alpha \\ \beta \end{Bmatrix}_\varepsilon \tag{3.49}$$

The fourth transformation is static condensation. The vector $\{\beta\}_\varepsilon$ is written in terms of the vector $\{\alpha\}_\varepsilon$ by setting the forces associated with $\{\beta\}_\varepsilon$ to zero

$$\begin{Bmatrix} \alpha \\ \beta \end{Bmatrix}_\varepsilon = [T_4]\{\alpha\}_\varepsilon \tag{3.50}$$

The final form of the total strain energy is found as

$$U = \frac{1}{2}\{\alpha\}_\varepsilon^T [T_4]^T [S][T_4]\{\alpha\}_\varepsilon = \frac{1}{2}\{\alpha\}_\varepsilon^T [K^*]\{\alpha\}_\varepsilon \tag{3.51}$$

where $[K^*]$ is the stiffness matrix of the equivalent continuum beam with dimensions of 6×6. After dividing it by the length of the repeating unit, it can directly be compared with the matrix given in Equation 3.40 to determine the effective stiffness properties and the coupling terms. From the static condensation or the fourth transformation, $[K^*]$ is computed as

$$[K^*] = [S_{11} - S_{12} S_{22}^{-1} S_{21}] \tag{3.52}$$

where S_{11}, S_{12}, S_{22} and S_{21} are the submatrices of matrix $[S]$ in Equation 3.49.

3.4.2 Modified Energy Equivalency Method

The method proposed here is a modified version of Dow's method [49] to make the procedure more straightforward and systematic. It also accounts for self-stress as suggested by Kebiche et al. [50] to determine effective stiffness properties of tensegrity structures. The third transformation is eliminated since the displacement field assumptions given by Dow are rearranged, and a systematic approach is suggested to identify the strain and strain gradients that will be retained through the second transformation. The first transformation is solely based on the cubic displacement field assumptions and, therefore, $[T_1]$ is slightly modified as displacement field assumptions are rearranged. The fourth transformation is a static condensation which is the same for any configuration. The modified energy equivalency method eliminates the second and the third transformations, and the whole process becomes more straightforward.

Similar to the previous method, the initial step is to approximate the displacement field at the nodes. Rearranged and rewritten displacement field assumptions are

$$\begin{split}u(x,y,z) = \varepsilon_x x + \varepsilon_{x,y} xy + \varepsilon_{x,z} xz + \frac{1}{2}\gamma_{xy} y + \frac{1}{2}\gamma_{xz} z + u + \frac{1}{2}\varepsilon_{x,x} x^2 - \frac{1}{2}\varepsilon_{y,x} y^2 \\ - \frac{1}{2}\varepsilon_{z,x} z^2 + \frac{1}{6}\varepsilon_{x,xx} x^3 + \frac{1}{2}\varepsilon_{x,yy} xy^2 + \frac{1}{2}\varepsilon_{x,zz} xz^2 + \frac{1}{2}\varepsilon_{x,xy} x^2 y - \frac{1}{6}\varepsilon_{y,xy} y^3 \\ - \frac{1}{2}\varepsilon_{z,xy} yz^2 + \frac{1}{2}\varepsilon_{x,xz} x^2 z - \frac{1}{2}\varepsilon_{y,xz} y^2 z - \frac{1}{6}\varepsilon_{z,xz} z^3 + \varepsilon_{x,yz} xyz + qz - \frac{1}{2}\gamma_{yz,x} y^2 \\ + \frac{1}{2}\gamma_{xy,y} yz + \frac{1}{2}(\gamma_{xy,z} + \gamma_{xz,y}) yz - ry + \frac{1}{2}\gamma_{xz,z} z^2 + \frac{1}{6}\gamma_{xy,yy} y^3 + \frac{1}{6}\gamma_{xz,zz} z^3 \\ + \frac{1}{2}\gamma_{xy,yz} y^2 z + \frac{1}{2}\gamma_{xz,yz} yz^2\end{split} \tag{3.53}$$

$$\begin{aligned} v(x,y,z) = &-\frac{1}{2}\varepsilon_{x,y}x^2 + \frac{1}{2}\gamma_{xy}x^2 + \frac{1}{2}(\gamma_{xy,z} - \gamma_{xz,y})xz + \varepsilon_y y + \varepsilon_{y,x}xy + v + \frac{1}{2}\varepsilon_{y,y}y^2 \\ &-\frac{1}{2}\varepsilon_{z,y}z^2 + \varepsilon_{y,z}yz + \frac{1}{2}\varepsilon_{y,xx}x^2y + \frac{1}{6}\varepsilon_{y,yy}y^3 + \frac{1}{2}\varepsilon_{y,zz}yz^2 - \frac{1}{6}\varepsilon_{x,xy}x^3 + \frac{1}{2}\varepsilon_{y,xy}xy^2 \\ &-\frac{1}{2}\varepsilon_{z,xy}xz^2 + \varepsilon_{y,xz}xyz - \frac{1}{2}\varepsilon_{x,yz}x^2z + \frac{1}{2}\varepsilon_{y,yz}y^2z - \frac{1}{6}\varepsilon_{z,yz}z^3 - pz + \frac{1}{2}\gamma_{yz}z + \frac{1}{2}\gamma_{xy,x}x^2 \\ &+\frac{1}{2}\gamma_{yz,x}xz + rx + \frac{1}{2}\gamma_{yz,z}z^2 + \frac{1}{6}\gamma_{xy,xx}x^3 + \frac{1}{6}\gamma_{yz,zz}z^3 + \frac{1}{2}\gamma_{xy,xz}x^2z + \frac{1}{2}\gamma_{yz,xz}xz^2 \end{aligned} \tag{3.54}$$

$$\begin{aligned} w(x,y,z) = &-\frac{1}{2}\varepsilon_{x,z}x^2 + \frac{1}{2}\gamma_{xz}x - \frac{1}{2}(\gamma_{xy,z} - \gamma_{xz,y})xy + \varepsilon_z z + \varepsilon_{z,x}xz + \varepsilon_{z,y}yz + w \\ &-\frac{1}{2}\varepsilon_{y,z}y^2 + \frac{1}{2}\varepsilon_{z,z}z^2 + \frac{1}{2}\varepsilon_{z,xx}x^2z + \frac{1}{2}\varepsilon_{z,yy}y^2z + \frac{1}{6}\varepsilon_{z,zz}z^3 + \varepsilon_{z,xy}xyz - \frac{1}{6}\varepsilon_{x,xz}x^3 \\ &-\frac{1}{2}\varepsilon_{y,xz}xy^2 + \frac{1}{2}\varepsilon_{z,xz}xz^2 - \frac{1}{2}\varepsilon_{x,yz}x^2y - \frac{1}{6}\varepsilon_{y,yz}y^3 + \frac{1}{2}\varepsilon_{z,yz}yz^2 + py - qx + \frac{1}{2}\gamma_{yz}y \\ &+\frac{1}{2}\gamma_{xz,x}x^2 + \frac{1}{2}\gamma_{yz,x}xy + \frac{1}{2}\gamma_{yz,y}y^2 + \frac{1}{6}\gamma_{xz,xx}x^3 + \frac{1}{6}\gamma_{yz,yy}y^3 + \frac{1}{2}\gamma_{xz,xy}x^2y + \frac{1}{2}\gamma_{yz,xy}xy^2 \end{aligned} \tag{3.55}$$

The first transformation matrix can be formed while retaining the fundamental strains in the first six rows of the continuum strain vector as follows:

$$\begin{bmatrix} u_1 \\ v_1 \\ w_1 \\ u_2 \\ v_2 \\ w_2 \\ \vdots \\ u_k \\ v_k \\ w_k \end{bmatrix} = \begin{bmatrix} x_1 & x_1y_1 & x_1z_1 & \frac{1}{2}y_1 & \frac{1}{2}z_1 & \cdots & \frac{1}{2}y_1^2z_1 & \frac{1}{2}y_1z_1^2 & 0 \\ 0 & -\frac{1}{2}x_1^2 & 0 & \frac{1}{2}x_1 & 0 & \cdots & 0 & 0 & \frac{1}{2}x_1z_1^2 \\ 0 & 0 & -\frac{1}{2}x_1^2 & 0 & \frac{1}{2}x_1^2 & \cdots & 0 & 0 & 0 \\ x_2 & x_2y_2 & x_2z_2 & \frac{1}{2}y_2 & \frac{1}{2}z_2 & \cdots & \frac{1}{2}y_2^2z_2 & \frac{1}{2}y_2z_2^2 & 0 \\ 0 & -\frac{1}{2}x_2^2 & 0 & \frac{1}{2}x_2 & 0 & \cdots & 0 & 0 & \frac{1}{2}x_2z_2^2 \\ 0 & 0 & -\frac{1}{2}x_2^2 & 0 & \frac{1}{2}x_2^2 & \cdots & 0 & 0 & 0 \\ \vdots & \vdots & \vdots & \vdots & \vdots & \vdots & \vdots & \vdots & \vdots \\ x_k & x_ky_k & x_kz_k & \frac{1}{2}y_k & \frac{1}{2}z_k & \cdots & \frac{1}{2}y_k^2z_k & \frac{1}{2}y_kz_k^2 & 0 \\ 0 & -\frac{1}{2}x_k^2 & 0 & \frac{1}{2}x_k & 0 & \cdots & 0 & 0 & \frac{1}{2}x_kz_k^2 \\ 0 & 0 & -\frac{1}{2}x_k^2 & 0 & \frac{1}{2}x_k^2 & \cdots & 0 & 0 & 0 \end{bmatrix} \begin{bmatrix} \varepsilon_x \\ \varepsilon_{x,y} \\ \varepsilon_{x,z} \\ \gamma_{xy} \\ \gamma_{xz} \\ k_t^0 \\ \vdots \\ \gamma_{xy,yz} \\ \gamma_{xz,yz} \\ \gamma_{yz,xz} \end{bmatrix} \tag{3.56}$$

Application of the first transformation (Equation 3.45) increases the size of the equivalent stiffness matrix to 60 × 60. The next step is the determination of the strains and strain gradients by investigating the configuration of the structure. They either cannot be exhibited by the structure or are linearly dependent on each other. Two methods are suggested by Dow et al. [49] to determine strain and strain gradient terms that will be not be retained for the analysis: calculating the rank of T_1 or utilizing the Love-Kirchoff approximations. In any case, the elimination process may be confusing when there are plentiful elements in the configuration. In this work, kinematic assumptions made by Noor et al. [45] are implemented to determine the coefficients retained.

The displacement components have a linear variation in the plane of a cross-section and are approximated as

$$u(x,y,z) = u^0 - y\phi_3 + z\phi_2 \tag{3.57}$$

$$v(x,y,z) = v^0 + y\varepsilon_y^0 + z\Big(-\phi_1 + \frac{1}{2}\gamma_{yz}^0\Big) \tag{3.58}$$

$$w(x,y,z) = w^0 + y\Big(\phi_1 + \frac{1}{2}\gamma_{yz}^0\Big) + z\varepsilon_z^0 \tag{3.59}$$

where the superscript 0 indicates a quantity evaluated at the center of the cross section $y = 0$, $z = 0$ and ϕ_i is the rotation around the i^{th} axis. Using strain-displacement relations the strain components are obtained as follows:

$$\varepsilon_x = \varepsilon_x^0 - y\kappa_y^0 + z\kappa_z^0 \tag{3.60}$$

$$\varepsilon_y = \varepsilon_y^0 \tag{3.61}$$

$$\varepsilon_z = \varepsilon_z^0 \tag{3.62}$$

$$\gamma_{xy} = \gamma_{xy}^0 + y\varepsilon_{y,x}^0 + z\Big(-\kappa_t^0 + \frac{1}{2}\gamma_{yz,x}^0\Big) \tag{3.63}$$

$$\gamma_{xz} = \gamma_{xz}^0 + y\Big(\kappa_t^0 + \frac{1}{2}\gamma_{yx,x}^0\Big) + z\varepsilon_{z,x}^0 \tag{3.64}$$

$$\gamma_{yz} = \gamma_{yz}^0 \tag{3.65}$$

Then, strain components are expanded into Taylor Series about the center of the lattice, $x = 0$. The Taylor Series expansions are:

$$\varepsilon_x = \varepsilon_x^0 - y\kappa_y^0 + z\kappa_z^0 + x(\varepsilon_{x,x}^0 - y\kappa_{y,x}^0 + z\kappa_{z,x}^0) \tag{3.66}$$

$$\varepsilon_y = \varepsilon_y^0 + x\varepsilon_{y,x}^0 + \frac{1}{2}x^2\varepsilon_{y,xx}^0 \tag{3.67}$$

$$\varepsilon_z = \varepsilon_z^0 + x\varepsilon_{z,x}^0 + \frac{1}{2}x^2\varepsilon_{z,xx}^0 \tag{3.68}$$

$$\gamma_{xy} = \gamma_{xy}^0 + y\varepsilon_{y,x}^0 + z\Big(-\kappa_t^0 + \frac{1}{2}\gamma_{yz,x}^0\Big) + x\Big(\gamma_{xy,x}^0 + y\varepsilon_{y,xx}^0 + z\Big(-\kappa_{t,x}^0 + \frac{1}{2}\gamma_{yz,xx}^0\Big)\Big) \tag{3.69}$$

$$\gamma_{xz} = \gamma_{xz}^0 + y\Big(\kappa_t^0 + \frac{1}{2}\gamma_{yx,x}^0\Big) + z\varepsilon_{z,x}^0 + x\Big(\gamma_{xz,x}^0 + y\Big(\kappa_{t,x}^0 + \frac{1}{2}\gamma_{yx,xx}^0\Big) + z\varepsilon_{z,xx}^0\Big) \tag{3.70}$$

$$\gamma_{yz} = \gamma_{yz}^0 + x\gamma_{yz,x}^0 + \frac{1}{2}x^2\gamma_{yz,xx}^0 \tag{3.71}$$

The number of Taylor expansion terms should be chosen based on the number of bays in the repeating unit. The detailed discussion can be found in the work by Noor et al. [45]. All the coefficients that appear in Noor's Taylor Series expansion are retained for the analysis. Then, the rows and columns associated with the strain and strain gradient terms that will be eliminated can be removed directly, similar to application of boundary conditions in finite element analysis. The result is a reduced stiffness matrix which is $r \times r$, where r is the number of coefficients retained.

The first six rows and columns of the reduced stiffness matrix are directly associated with the fundamental strains. Therefore, the third transformation is not required, and the static condensation procedure may proceed. The static condensation or the fourth transformation (second in this case) is already given in Equation 3.52 where $[S] = [K_{reduced}]$. Finally, $[K^*]$ is divided by the length of the repeating unit, and the diagonal terms provide the effective stiffness properties, while the off-diagonal terms are the coupling terms.

In summary, the proposed method here utilizes two transformation and one reduction in stiffness matrix to determine effective stiffness properties. The first transformation relates discrete nodal displacements to continuum strains and strain gradients. Then, a reduction is applied to the continuum stiffness matrix (60×60) by eliminating the coefficients which are not exhibited by the structure or are linearly dependent. Then, the second transformation is the static condensation which reduces the stiffness matrix further to 6×6 in terms of fundamental strains. Since the global stiffness matrix of the repeating unit may include the effects of pre-stress, the procedure can be applied to structures with self-stress states such as tensegrities.

Numerical Example

Yildiz and Lesieutre [57] studied a numerical example in which the modified energy equivalency method was applied to two stage cylindrical tensegrity booms with three, four, five, and six struts in each stage, as shown in Figures 3.10, 3.11, 3.12, and 3.13. The booms consist of $3n$ nodes, $2n$ struts, and $5n$ cables where n is the number of struts.

The radius of the tensegrity booms are chosen as $50\sqrt{2}$ cm and the total height is 200 cm. The modulus of elasticity of the cables and struts are 40 GPa and 200 GPa. The cross-sectional areas of the cables and struts are selected as 0.28 cm^2 and 3.25 cm^2. Then, the pre-stress coefficient, P_s is varied between 0 and 150, and the analyses are repeated to see the effect of the pre-stress values on the effective stiffness properties. After the form finding procedure, the force-densities are normalized so that the top and bottom cables carry unit force density. Then, force-densities are multiplied by the length of members and the pre-stress coefficient to calculate pre-stress forces. Table 3.4 shows the pre-stress values in the elements for each case.

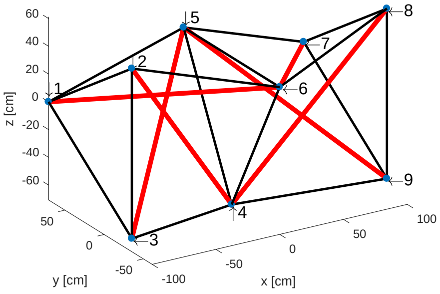

Figure 3.10: Two Stage Three-Strut Tensegrity Boom

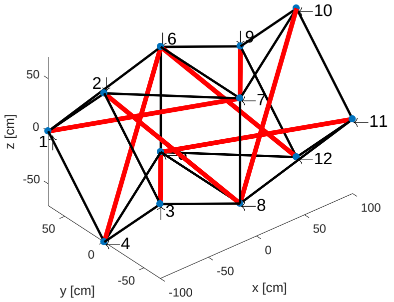

Figure 3.11: Two Stage Four-Strut Tensegrity Boom

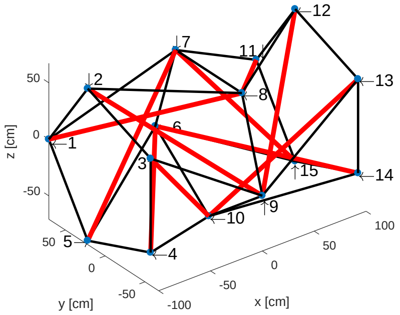

Figure 3.12: Two Stage Five-Strut Tensegrity Boom

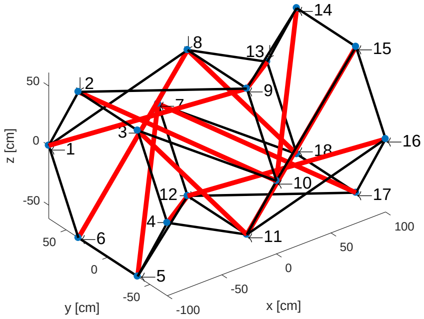

Figure 3.13: Two Stage Six-Strut Tensegrity Boom

Table 3.4: Pre-stress values in the elements

	Pre-stress [kN]			
Element Type	**n=3**	**n=4**	**n=5**	**n=6**
Top-Bottom Cables	$1.2247P_s$	$1.0000P_s$	$0.8313P_s$	$0.7071P_s$
Vertical Cables	$1.8444P_s$	$1.6080P_s$	$1.3970P_s$	$1.2247P_s$
Saddle Cables	$2.4495P_s$	$2.0000P_s$	$1.6625P_s$	$1.4142P_s$
Struts	$-2.9322P_s$	$-2.3268P_s$	$-1.8911P_s$	$-1.5811P_s$

Figures 3.14, 3.15, 3.16, and 3.17 show the variation of effective stiffness properties of the two stage tensegrity booms.

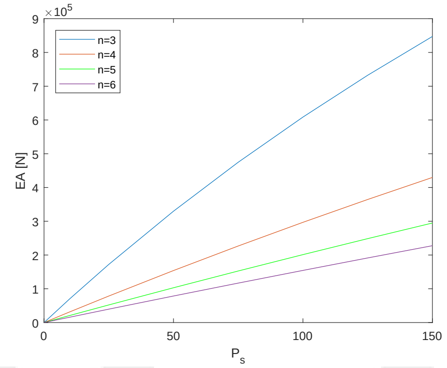

Figure 3.14: Variation of axial rigidity

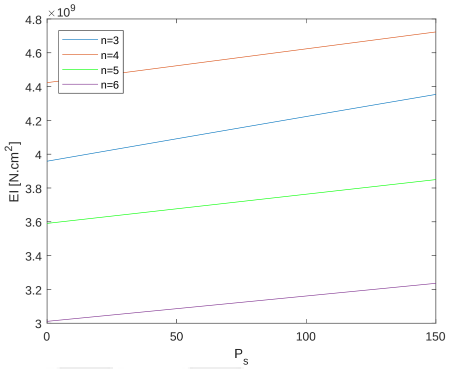

Figure 3.15: Variation of bending rigidity

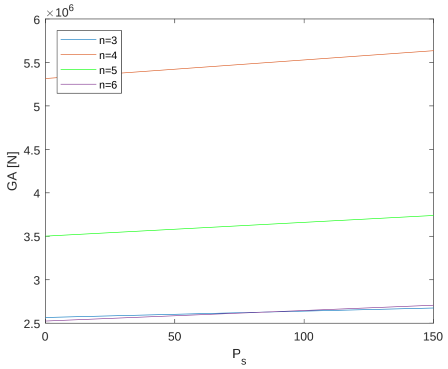

Figure 3.16: Variation of shear rigidity

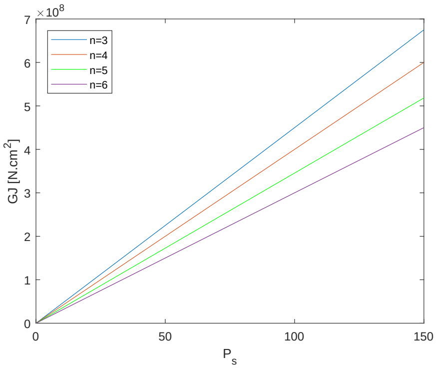

Figure 3.17: Variation of torsional rigidity

Figures 3.14 and 3.17 reveal that the axial and torsional rigidities of the investigated tensegrity booms are zero unless the structure is pre-stressed. The reason for this behavior is that the infinitesimal mechanisms exhibited by the structure act in the axial and torsional directions, making the associated rigidities zero unless it is self-stressed, as also noted by Kebiche et al. [50]. On the other hand, bending and shear rigidities are non-zero even if the structure is not pre-stressed. Furthermore, due to symmetry about the yz plane, all of the coupling terms are found to be zero.

The influence of self-stress implementation and variation of pre-stress levels on effective stiffness properties are found to be different. Axial and torsional rigidities are affected significantly as they are prone to variation of self-stress. This is mostly due to existence of mechanisms acting in these directions. Conversely, bending and shear rigidities are not affected by the changes in self-stress as axial and torsional rigidities are.

Figures 3.14, 3.15, 3.16, and 3.17 reveal another interesting result. One may anticipate that the rigidities would increase with increasing number of struts; however, the results reveal otherwise. Axial and torsional rigidities reach a maximum level when the number of struts is three. As the number of struts increases, the axial and torsional rigidities subsequently decrease with each increment. However, the maximum bending and shear rigidities are observed when the number of struts is four. These rigidities are found to be decreasing with increasing number of struts when $n \geq 4$.

The main reason for this type of behavior can be explained with the increased number of mechanisms with increasing number of struts. A two-stage cylindrical tensegrity structure exhibits $2n-4$ mechanisms and 2 states of self-stress. Therefore, as the number of struts increase, the number of mechanisms also increases. It is clear that the increased number of struts affects the structure by softening it because of the mechanisms.

3.4.3 Nonlinear Finite Element Validation

Nonlinear finite element analyses described in previous sections can also be used to determine the effective stiffness properties of tensegrity booms. Appropriate boundary conditions can be imposed to tensegrity booms, and their behavior under external forces which create pure axial, bending, shear, or torsion can be applied [58, 59]. The total strain energy of tensegrity booms under external loads can be obtained from the incremental iterative solution scheme.

Sun et al. [58] show examples of boundary conditions and loading cases for beam-like lattice structures. They state that a typical substructure (repeating unit) can be considered, and finite element analyses can be carried out. In order to determine the axial rigidity of a structure, axial loads can be applied at the free end while the other end is completely fixed. Then, a relationship between the applied the axial load and axial rigidity can be written as:

$$EA = \frac{NL}{\delta} \tag{3.72}$$

where N, L and δ are applied axial loads, length of the substructure, and axial displacement.

A similar approach can be taken for torsional rigidity. Nodal forces can be applied to the free end that create a pure torsional moment and no resultant force while the other end is completely fixed. Then, a relationship between the rotation of the free end, θ and generated torsional moment can be written as:

$$GJ = \frac{M_x L}{\theta} \tag{3.73}$$

where M_x is the generated torsional moment.

Determination of bending and torsional rigidities require different boundary conditions in order to account for possible distortion of cross-sections. The approach provided by Sun et al. [58] states that one of the nodes in the corresponding end should be fixed completely while the others should be restrained in the axial direction.

In order to determine bending rigidity, axial loads can be applied to generate a bending moment with zero resultant force. Then, the rotation angle due to bending, ϕ can be calculated, and a relationship can be formed as:

$$EI = \frac{ML}{\phi} \tag{3.74}$$

where M is the bending moment.

Applying shear loads always generates bending moments and, therefore, determination of shear rigidity is troublesome. In an attempt to create a pure shear load case, Sun et al. [58] modify the boundary conditions by constraining the free end in the axial direction. Then, shear loads can be applied and analogously, the following relationship can be formed:

$$GA = \frac{VL}{v_b} \tag{3.75}$$

where V and v_b are the shear load and lateral displacement.

On the other hand, the effective stiffness properties or rigidities can also be obtained by calculating total strain energy. From finite element analyses, the total strain energy can be obtained, and effective stiffness properties can be determined from the following strain energy expressions:

$$U = \frac{1}{2}\frac{N^2 L}{EA} \tag{3.76}$$

$$U = \frac{1}{2}\frac{M^2 L}{EI} \tag{3.77}$$

$$U = \frac{1}{2}\frac{V^2 L}{GA} \tag{3.78}$$

$$U = \frac{1}{2}\frac{M_x^2 L}{GJ} \tag{3.79}$$

However, the procedure becomes complex when the focus is tensegrity structures. Tensegrity structures exhibit initial strain energy due to pre-stress which must be considered. Furthermore, applied external loads have to be in the same order of magnitude as pre-stress levels. Since the effective stiffness properties are only valid in the proximity of the initial configuration, application of larger loads do not yield accurate results as the structure deforms greater. Furthermore, the reaction forces at the fixed end should be checked to ensure they are consistent with applied loads.

At the end of the nonlinear finite element analyses, final strain energy is computed, and the difference between final and initial strain energy is used to determine the effective stiffness properties. For different loading scenarios of pure loading, the difference in final and initial strain energies related to effective stiffness properties are

$$U_{diff} = \frac{1}{2}\int_V \sigma^T \varepsilon dV = \frac{1}{2}\frac{N^2 L}{(EA)_{eff}} \tag{3.80}$$

$$U_{diff} = \frac{1}{2}\int_V \sigma^T \varepsilon dV = \frac{1}{2}\frac{M^2 L}{(EI)_{eff}} \tag{3.81}$$

$$U_{diff} = \frac{1}{2}\int_V \sigma^T \varepsilon dV = \frac{1}{2}\frac{V^2 L}{(GA)_{eff}} \tag{3.82}$$

$$U_{diff} = \frac{1}{2}\int_V \sigma^T \varepsilon dV = \frac{1}{2}\frac{M_x^2 L}{(GJ)_{eff}} \tag{3.83}$$

where U_{diff} is the difference in the final and initial strain energy.

Nonlinear finite element analyses are applied to the tensegrity booms, and sample results are presented below in Figures 3.18, 3.19, 3.20, and 3.21 for tensegrity booms with three and four struts in each stage.

Figure 3.18, 3.19, 3.20, and 3.21 show the finite element results alongside energy

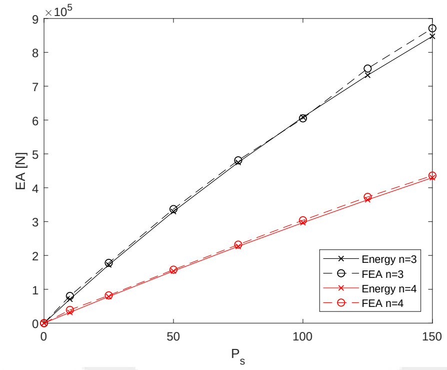

Figure 3.18: Comparison of results for axial rigidity

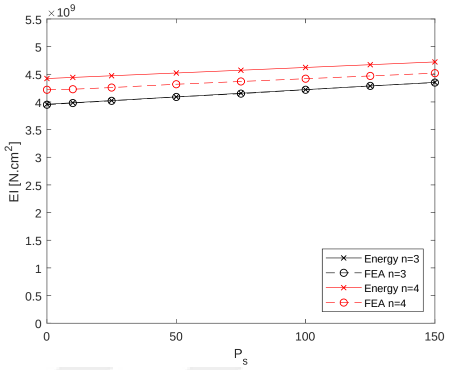

Figure 3.19: Comparison of results for bending rigidity

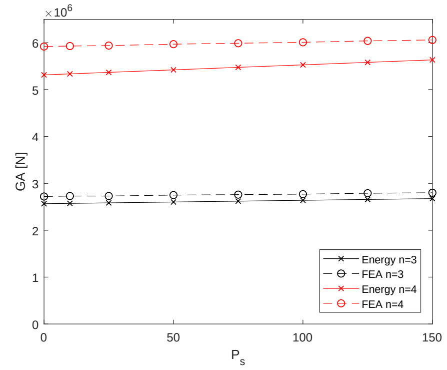

Figure 3.20: Comparison of results for shear rigidity

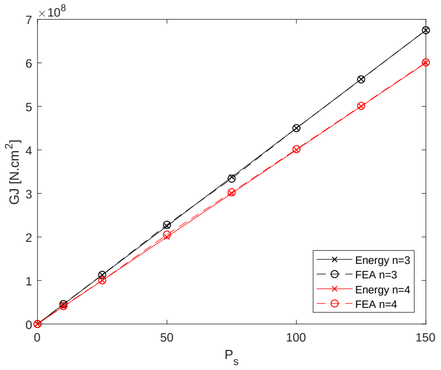

Figure 3.21: Comparison of results for torsional rigidity

equivalency results. The results show excellent agreement between finite element and energy equivalency for axial and torsional rigidities, Figures 3.18 and 3.21. On the other hand, a discrepancy occurs between the results for bending and shear rigidities, Figures 3.19 and 3.20. The maximum errors between the results are obtained as 2% for axial rigidity, 7% for bending and shear rigidity, and less than 1% for torsional rigidity.

Potential reasons for the error between the results in Figures 3.19 and 3.20 are identified as inappropriate boundary conditions and inaccurate loading. It is a known fact that generating pure shear loading is nearly impossible since shear loads also result in bending moments. The results are also very sensitive to boundary conditions, and distortion of the cross-section at the base should also be considered. Another important point is the applied level of loads since these effective stiffness properties are only valid in the close proximity of the initial configuration. If the external loads are selected relatively higher than the internal loads (pre-stress levels), the structure deforms more, leading to inconsistent results due to geometric nonlinearity.

The modified energy equivalency method reduces the complexity of computing the effective stiffness properties of a tensegrity boom, and it may be applied to truss type structures as well. Rather than requiring four transformations, the number of transformations is reduced, and an algorithm which is easier to implement has been developed. The results are compared to the nonlinear finite element results, and excellent agreement in axial and torsional rigidities are obtained while bending and shear rigidities are good.

In summary, application of the modified energy equivalency method enables straightforward optimization and comparison of different booms. For a given geometry, the optimum beam may be designed in terms of maximum stiffness or stiffness-to-mass ratio. Furthermore, instead of carrying out a full scale nonlinear finite element analysis for geometrically nonlinear problems, effective stiffness properties may iteratively be obtained and used to determine the behavior of the structure under external loads. In Chapter 6, the modified energy equivalency method is implemented for optimization of tensegrity structures to design a tensegrity boom with maximum stiffness-to-mass ratio.

Chapter 4

Deployment of Cylindrical Tensegrity Booms

Tensegrity structures have been considered as deployable space structures since the early 1990s. The idea of deployable tensegrity structures was first proposed and conceptually examined by Furuya [14]. They have been identified as very promising deployable structures for space applications due to certain advantages including light weight and high packing density. Further, most of the traditional deployable structures experience difficulties due to complex joints or the use of telescopic struts. In tensegrity structures, compressive elements are mostly discontinuous; thus complex joints are avoided. These advantages pave the way for utilization of tensegrity structures for space applications.

Two distinct strategies have been proposed for the deployment of tensegrity structures, namely cable-mode and strut-mode deployment [2, 13]. Sultan and Skelton [16, 60–62] investigated a Snelson-type tensegrity boom with three struts and made important contributions using tendon control deployment. The same Snelson-type tensegrity boom was also investigated by Tibert and Pellegrino [17], and strut-mode deployment is demonstrated using telescopic struts. The advantages and disadvantages of each method were pointed out in detail by Tibert and Pellegrino [17]. Deployment of a three-strut Class-2 cylindrical tensegrity boom was examined by Pinaud et al. [18] using cable-mode deployment. More recently, this deployment concept was also utilized for bridge constructions in which deployment starts with two bases that are connected to each other at the middle when the full deployment is achieved [63–65].

Cable-mode deployment controls the lengths of the cables with small motors attached to struts (internally or externally). Cables can be rolled over or released from small wheels to alter the lengths of the cables [16, 62]. In this way, as long as the lengths of the cables are controlled in a prescribed manner, the self-equilibrium of the structure can be maintained, exhibiting stiffness to some extent. Struts are stiffer and heavier compared to cables; therefore, they remain rigid during deployment.

The strut-mode deployment arises from the idea of struts being the longest elements in the structures [17]. Therefore, greater packaging efficiency may be acquired by folding the struts. However, this deployment strategy requires additional devices to deploy tensegrity booms since they are not self-equilibrated when stowed this way. An additional rod which controls the rate of deployment by increasing the height of the structure can be used. Furthermore, as the height of the boom is increased, the cables should be pre-stressed to gain stiffness.

Cable-mode deployment is reported to be superior since the tensegrity structure remains stiff while deploying and no additional stiffening devices are required [17]. Furthermore, if the controls are frozen at some instant of deployment, the structure will remain self-equilibrated and the deployment can be restarted.

In this chapter, deployments of tensegrity booms with different topologies are addressed. Deployment of Class-1 three-strut tensegrity booms is investigated with a cable-mode deployment strategy, and a generalization procedure for n-strut tensegrity boom deployment is given. Then, deployment of Class-2 three-strut tensegrity booms is explained, and another generalization procedure for n-strut Class-2 tensegrity towers is illustrated. For demonstration purposes, deployment examples of n-strut Class-1 and Class-2 tensegrity booms are simulated.

4.1 Deployment of Class-1 Tensegrity Booms

Deployment of Class-1 tensegrity booms was first studied by Sultan and Skelton [16, 62]. They investigated a three-strut, two-stage SVD tensegrity boom which is also known as a Snelson-type tensegrity. An SVD tensegrity structure is a Class-1 tensegrity system in which no contact between struts occur. The investigated SVD tensegrity boom consists of 6 struts and 24 cables (3 bottom, 3 top, 6 saddle, 6 vertical, and 6 diagonal), and it is named after saddle, vertical and diagonal cables. The structure has equilateral triangular top and bottom bases while an overlap at the intersection of two stages satisfies the prestressability conditions. The geometry of the SVD tensegrity boom is shown in Figure 4.1.

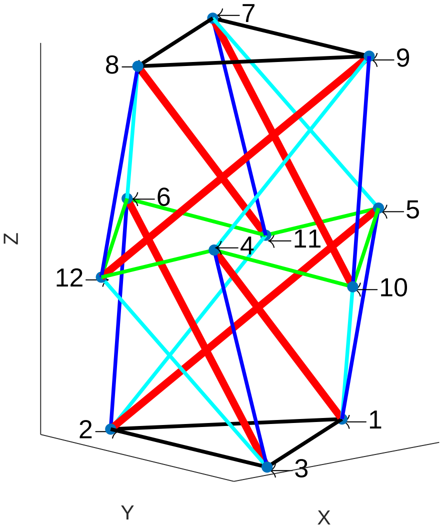

Figure 4.1: Three-strut Snelson type tensegrity

Black, blue, green, and teal lines represent top and bottom, vertical, saddle, and diagonal cables, respectively. In addition, struts are denoted with thick red lines. The overlap is the vertical distance between the nodes at the intersection, seen in Figure 4.2, while the top view of the structure is shown in Figure 4.3.

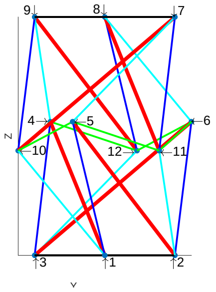

Figure 4.2: SVD Side view

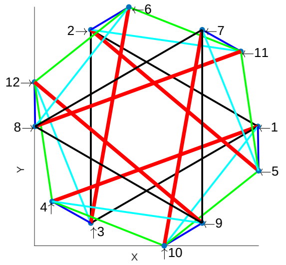

Figure 4.3: SVD Top view

Sultan noted that each node can be represented in terms of three independent parameters: azimuth angle of struts, α_{ij}, declination angle of struts, δ_{ij}, and overlap, h [61, 66]. Here, i and j represent the nodes that are connected with a strut. For a symmetrical, three-strut SVD tensegrity boom as shown in Figure 4.1, all of the declination angles are the same, while the azimuth angles of consecutive struts differ by 60°, due to symmetry.

Sultan defined an equilibrium matrix in terms of the independent parameters and obtained the solution analytically. The equilibrium matrix is given as follows:

$$\mathbf{A} = \begin{bmatrix} \dfrac{\partial S}{\partial \alpha} & \dfrac{\partial V}{\partial \alpha} & \dfrac{\partial D}{\partial \alpha} \\ \dfrac{\partial S}{\partial \delta} & \dfrac{\partial V}{\partial \delta} & \dfrac{\partial D}{\partial \delta} \\ \dfrac{\partial S}{\partial h} & \dfrac{\partial V}{\partial h} & \dfrac{\partial D}{\partial h} \end{bmatrix} \tag{4.1}$$

where S, V and D are the lengths of saddle, vertical, and diagonal cables, respectively. These length expressions are derived by Sultan analytically as follows:

$$S = \sqrt{h^2 + \frac{b^2}{3} + l^2 \sin^2(\delta) - \frac{2}{\sqrt{3}} lb \sin(\delta) \cos\left(\alpha - \frac{\pi}{6}\right)} \tag{4.2}$$

$$V = \sqrt{l^2 + b^2 - 2lb \sin(\delta) \sin\left(\alpha + \frac{\pi}{6}\right)} \tag{4.3}$$

$$D = \sqrt{l^2 + \frac{b^2}{3} + h^2 - 2lh \cos(\delta) - \frac{2}{\sqrt{3}} lb \sin(\delta) \sin(\alpha)} \tag{4.4}$$

where l is the length of struts, and b is the length of top and bottom cables (side length of the equilateral triangles). Since the structure is in a symmetric configuration, the saddle, vertical, and diagonal cables have the same length, respectively. Therefore, the azimuth angle of any of the struts can be used for the length expressions.

The prestressability condition can be written as:

$$\mathbf{A}(\alpha, \delta, h)\mathbf{T} = \mathbf{0} \tag{4.5}$$

where $\mathbf{T}$ is the normalized force vector of the saddle, vertical, and diagonal cables. The non-trivial solution is obtained from

$$det(\mathbf{A}(\alpha, \delta, h)) = 0 \tag{4.6}$$

Equation 4.6 is solved for the overlap analytically, yielding:

$$h = \begin{cases} \dfrac{\cos(\delta)}{2\sin(\delta)\cos(\alpha+\pi/6)}\left(\dfrac{-b}{\sqrt{3}} + p + \sqrt{\dfrac{b^2}{3} - 3p^2}\right) & \text{if } \alpha \neq \dfrac{\pi}{3} \\ \dfrac{l\cos(\delta)}{2} & \text{if } \alpha = \dfrac{\pi}{3} \end{cases} \tag{4.7}$$

where $p = l\sin(\delta)\cos(\alpha+\pi/6)$. The prestressability condition, Equation 4.5, can be solved for force values in individual group of members. The solution is given as

$$\mathbf{T} = \begin{bmatrix} T_s & T_v & T_d \end{bmatrix}^T \tag{4.8}$$

$$T_v = \begin{cases} \dfrac{V}{D}\dfrac{1}{\sqrt{3}\cos(\alpha+\pi/6)}\left(\left(\dfrac{l\cos(\delta)}{h} - 1\right)\sin\left(\alpha - \dfrac{\pi}{6}\right) - \cos(\alpha)\right)T_d & \text{if } \alpha \neq \dfrac{\pi}{3} \\ \dfrac{V}{D}\left(\dfrac{3l}{2b}\sin(\delta) - 1\right)T_d & \text{if } \alpha = \dfrac{\pi}{3} \end{cases} \tag{4.9}$$

$$T_s = \begin{cases} \dfrac{S}{D}\left(\dfrac{l\cos(\delta)}{h} - 1\right)T_d & \text{if } \alpha \neq \dfrac{\pi}{3} \\ T_d & \text{if } \alpha = \dfrac{\pi}{3} \end{cases} \tag{4.10}$$

$$T_d = 1 \tag{4.11}$$

Then, force balance at each node yields the force carried by struts, T_{st} as follows:

$$T_{st} = \begin{cases} \frac{T_d}{6Dh\sin(\pi/3-\alpha)}\Bigg(2\sqrt{3}hb\sin(\delta) - \frac{\sqrt{3}}{2}lb\sin(2\delta) & \\ + 6h^2\cos(\delta)\sin\left(\alpha-\frac{\pi}{3}\right) - 6lh\Bigg(\cos^2(\delta)\sin\left(\alpha-\frac{\pi}{3}\right) & \text{if } \alpha \neq \frac{\pi}{3} \\ - \frac{1}{\sqrt{3}}\sin\left(\alpha+\frac{\pi}{6}\right)\Bigg) + 2\sqrt{3}l^2\cos(\delta)\cos(\alpha) & \\ + 6l^2\cos^3(\delta)\sin\left(\alpha-\frac{\pi}{3}\right)\Bigg) & \\ \frac{T_d}{D}\left(\frac{3l^2}{2b}\sin(\delta)-\frac{l}{2}\right) & \text{if } \alpha = \frac{\pi}{3} \end{cases} \tag{4.12}$$

The overlap expression given in Equation 4.7 can be evaluated for selected l and b values. The results can be represented as equilibrium surfaces with respect to overlap and total height. For numerical values of $l = 0.4$ m and $b = 0.27$ m, the equilibrium surfaces are shown in Figures 4.4 and 4.5. Note that the equilibrium surface is found by using α_{14}, the azimuth angle of the strut between nodes 1 and 4 (Figure 4.1).

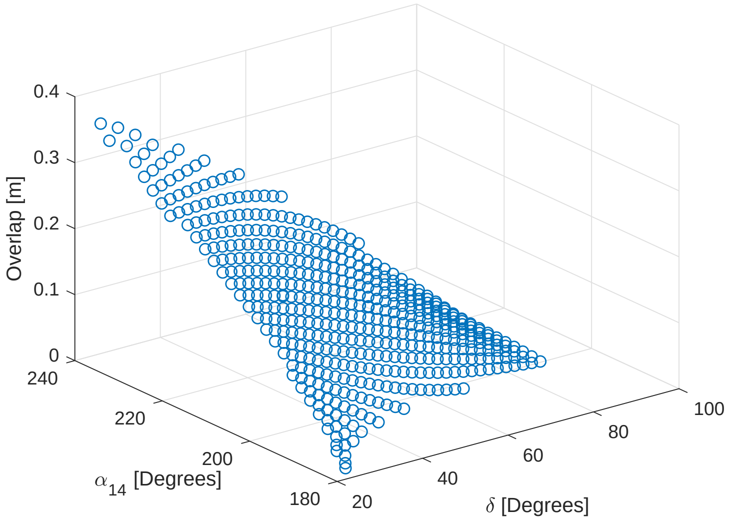

Figure 4.4: Equilibrium surface in terms of overlap

A self-equilibrated Class-1 SVD tensegrity boom is generated only if the parameters of α_{14} and δ, the azimuth angle of the strut between nodes 1 and 4, and

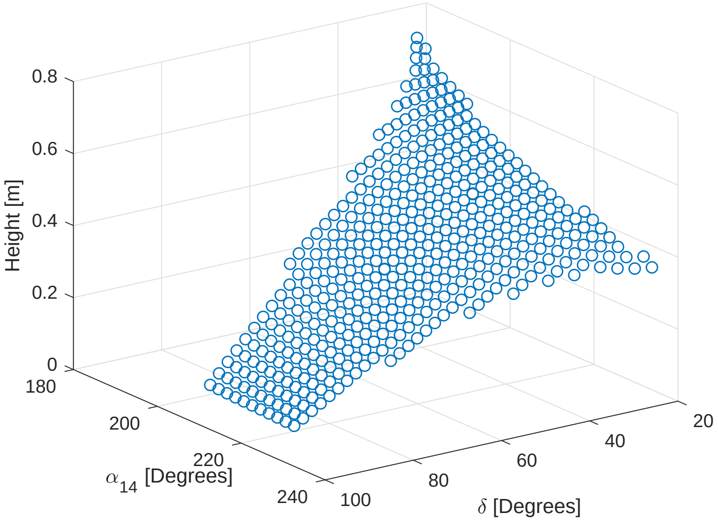

Figure 4.5: Equilibrium surface in terms of total height

the declination angle, are on the equilibrium surface. For an example deployment simulation, the initial and final parameters are chosen as $\alpha_{14,i} = 219°$, $\delta_i = 85°$, $\alpha_{14,f} = 200°$, and $\delta_f = 55°$. The deployment path is illustrated on the equilibrium surface with respect to height in Figure 4.6. The sequence of the deployment simulation can be seen in Figures 4.7, 4.8, 4.9, and 4.10.

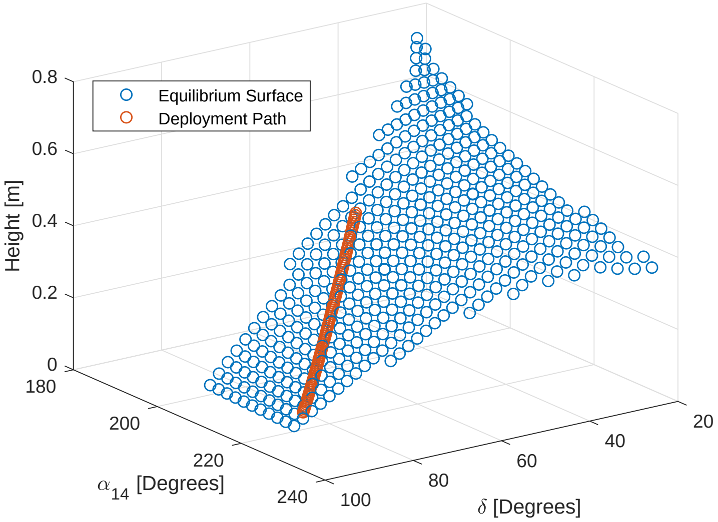

Figure 4.6: Deployment path of SVD

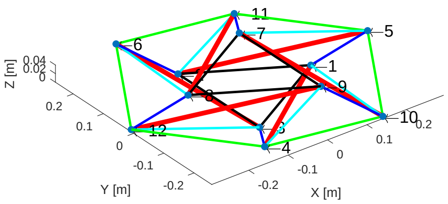

Figure 4.7: Deployment sequence, 1/4

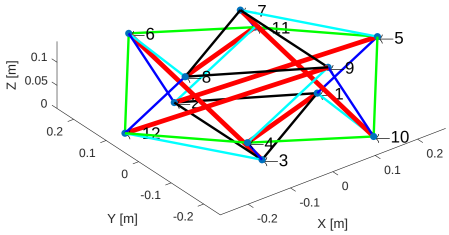

Figure 4.8: Deployment sequence, 2/4

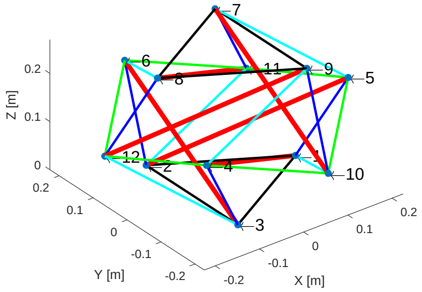

Figure 4.9: Deployment sequence, 3/4

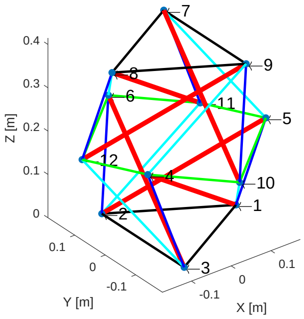

Figure 4.10: Deployment sequence, 4/4

During deployment, using a force finding method, force-densities in each type of member are tracked. Figures 4.11 and 4.12 show the variation of the lengths of and the force-densities carried by the elements in the structure, respectively. Figure 4.11 reveals that the top and bottom cables as well as the struts maintain their lengths, the saddle and diagonal cables are shortened, while the vertical cables are lengthened, increasing the total height of the structure. The variation of the force-densities, Figure 4.12, shows that cables and struts are always under tension and compression, respectively.

The same deployment procedure can be applied to longer tensegrity booms with more than two stages. In order to construct tensegrity booms longer than two stage, the tensegrity units can be stacked in such a way that there is an overlap for each pair of intersecting intermediate planes.

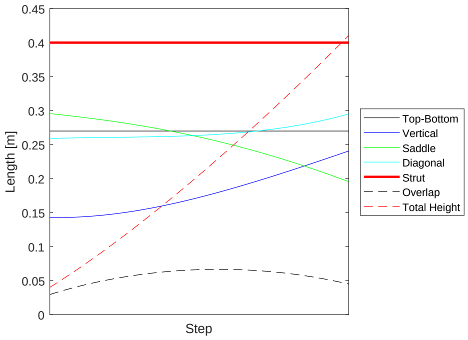

Figure 4.11: Variation of the lengths

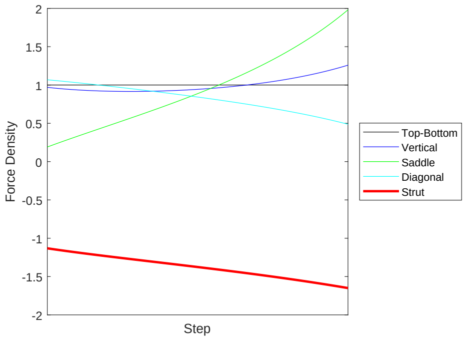

Figure 4.12: Variation of the force-densities

Additionally, it is also possible to increase the number of struts in one stage to address different concerns. This is achieved with a generalization procedure explained in the following subsection, and the deployment of n-strut Class-1 tensegrity booms is investigated.

4.1.1 Deployment of n-strut Class-1 Tensegrity Booms

In this section, the generalization of deployment of n-strut cylindrical tensegrity booms is developed. In order to generalize n-strut cylindrical Class-1 tensegrity structures, nodal locations and connectivity information need to be defined in terms of some parameters. The nodal coordinates and connectivity information are found to follow a pattern and, following this pattern, cylindrical Class-1 tensegrity booms with n struts in each stage can be constructed.

The generalization procedure starts with defining the nodal locations in terms of length of struts, radii of circumscribing circles of top and bottom stages, azimuth and declination angles. The fundamental idea is that nodes are distributed in the xy plane on a circle. For a two-stage cylindrical Class-1 tensegrity boom, the nodes are located on four different positions on the z axis, called levels. These positions are bottom, top, lower intersection, and upper intersection. The pattern given in Table 4.1 is valid for two-stage cylindrical Class-1 tensegrity booms with n struts in each stage.

These types of tensegrities typically have $4n$ nodes (n nodes in each level) and $10n$ elements.

Table 4.1: Location of the nodes in a two stage cylindrical Class-1 boom

	Node	x	y	z
Bottom Level	1	r_{base}	0	0
	2	$r_{base}\cos(\gamma)$	$r_{base}\sin(\gamma)$	0
	3	$r_{base}\cos(2\gamma)$	$r_{base}\sin(2\gamma)$	0
	$\cdots$	$\cdots$	$\cdots$	0
	n-1	$r_{base}\cos((n-2)\gamma)$	$r_{base}\sin((n-2)\gamma)$	0
	n	$r_{base}\cos((n-1)\gamma)$	$r_{base}\sin((n-1)\gamma)$	0
Upper Intersection Level	n+1	$x_1 + l_b\cos(\alpha_1)\sin(\delta)$	$y_1 + l_b\sin(\alpha_1)\sin(\delta)$	$l_b\cos(\delta)$
	n+2	$x_2 + l_b\cos(\alpha_1+\gamma)\sin(\delta)$	$y_2 + l_b\sin(\alpha_1+\gamma)\sin(\delta)$	$l_b\cos(\delta)$
	n+3	$x_3 + l_b\cos(\alpha_1+2\gamma)\sin(\delta)$	$y_3 + l_b\sin(\alpha_1+2\gamma)\sin(\delta)$	$l_b\cos(\delta)$
	$\cdots$	$\cdots$	$\cdots$	$l_b\cos(\delta)$
	2n-1	$x_{n-1} + l_b\cos(\alpha_1+(n-2)\gamma)\sin(\delta)$	$y_{n-1} + l_b\sin(\alpha_1+(n-2)\gamma)\sin(\delta)$	$l_b\cos(\delta)$
	2n	$x_n + l_b\cos(\alpha_1+(n-1)\gamma)\sin(\delta)$	$y_n + l_b\sin(\alpha_1+(n-1)\gamma)\sin(\delta)$	$l_b\cos(\delta)$
Top Level	2n+1	$r_{base}\cos(\gamma/2)$	$r_{base}\sin(\gamma/2)$	$2l_b\cos(\delta)-h$
	2n+2	$r_{base}\cos(\gamma/2+\gamma)$	$r_{base}\sin(\gamma/2+\gamma)$	$2l_b\cos(\delta)-h$
	2n+3	$r_{base}\cos(\gamma/2+2\gamma)$	$r_{base}\sin(\gamma/2+2\gamma)$	$2l_b\cos(\delta)-h$
	$\cdots$	$\cdots$	$\cdots$	$2l_b\cos(\delta)-h$
	3n-1	$r_{base}\cos(\gamma/2+(n-2)\gamma)$	$r_{base}\sin(\gamma/2+(n-2)\gamma)$	$2l_b\cos(\delta)-h$
	3n	$r_{base}\cos(\gamma/2+(n-1)\gamma)$	$r_{base}\sin(\gamma/2+(n-1)\gamma)$	$2l_b\cos(\delta)-h$
Lower Intersection Level	3n+1	$x_{2n+1} + l_b\cos(\alpha_1+\gamma/2)\sin(\delta)$	$y_{2n+1} + l_b\sin(\alpha_1+\gamma/2)\sin(\delta)$	$l_b\cos(\delta)-h$
	3n+2	$x_{2n+2} + l_b\cos(\alpha_1+\gamma+\gamma/2)\sin(\delta)$	$y_{2n+2} + l_b\sin(\alpha_1+\gamma+\gamma/2)\sin(\delta)$	$l_b\cos(\delta)-h$
	3n+3	$x_{2n+3} + l_b\cos(\alpha_1+2\gamma+\gamma/2)\sin(\delta)$	$y_{2n+3} + l_b\sin(\alpha_1+2\gamma+\gamma/2)\sin(\delta)$	$l_b\cos(\delta)-h$
	$\cdots$	$\cdots$	$\cdots$	$l_b\cos(\delta)-h$
	4n-1	$x_{3n-1} + l_b\cos(\alpha_1+(n-2)\gamma+\gamma/2)\sin(\delta)$	$y_{3n-1} + l_b\sin(\alpha_1+(n-2)\gamma+\gamma/2)\sin(\delta)$	$l_b\cos(\delta)-h$
	4n	$x_{3n} + l_b\cos(\alpha_1+(n-1)\gamma+\gamma/2)\sin(\delta)$	$y_{3n} + l_b\sin(\alpha_1+(n-1)\gamma+\gamma/2)\sin(\delta)$	$l_b\cos(\delta)-h$

where r_{base} is the radii of the circumscribing circles of top and bottom levels, α_1 is the azimuth angle of the strut that connects the nodes 1 and $n+1$, δ is the declination angle, and l_b is the length of struts. Additionally, h is the overlap and $\gamma = 2\pi/n$.

The number of stages may be increased easily by following Table 4.1. For example, in order to add another stage, the top level will be the second upper intersection level, and two new levels will be added. One of these new levels will be the second lower intersection level whose nodes overlap with the bottom level in xy plane with the height of $2l_b\cos(\delta) - 2h$, while the second new level will have the same node projection as the upper intersection level in xy plane with the height of $3l_b\cos(\delta) - 2h$.

In order to define the full geometry of a n-strut cylindrical tensegrity boom, a connectivity chart can be generated as in Figure 4.13 for the connectivity information.

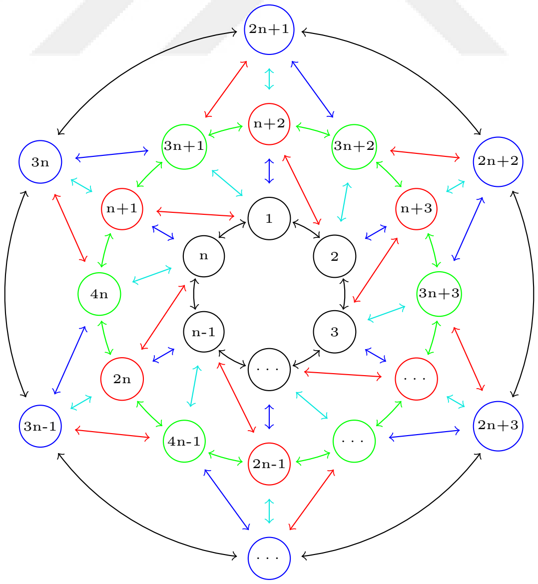

Figure 4.13: Connectivity chart for Class-1 tensregrity booms

In Figure 4.13, each node is represented with a circle, and the edge color of each circle indicates which level the node belongs to. Bottom, top, lower intersection, and upper intersection levels are indicated with black, blue, green, and red circles. Furthermore, each double-headed arrow defines a connection between the associated nodes. Three circular layers are generated to account for bottom, top and intersection levels. In order to avoid overlapping of the arrows, the first nodes of the bottom and top levels are located at the upper point of the corresponding layer such as 1 and $2n + 1$, while the intersection layer is rotated 90° in the counter-clockwise direction. Additionally, each color of the double-headed arrows indicate a different type of element. Black, blue, green, teal, and red arrows represent top and bottom, vertical, saddle, diagonal cables, and struts respectively.

Similar to nodal locations, this chart can also be generated for cylindrical Class-1 tensegrity booms with more than two stages. In order to add another stage, the outer layer can be modified by adding n more circles to make it similar to the intersection layer, and another layer can be added to the exterior. Then, the connectivity between these layers can be established by replicating the connectivity in the interior layers.

In order to generate the equilibrium surface for n-strut cylindrical Class-1 tensegrity booms, a numerical approach is adopted rather than the analytical approach employed by Sultan [61]. MATLAB's symbolic toolbox is utilized to define the nodal locations symbolically, and the lengths of saddle, vertical, and diagonal cables are obtained. These symbolic length expressions are then differentiated with respect to azimuth and declination angles, and overlap. The derivatives can be substituted into Equation 4.1, and the determinant of the equilibrium matrix can be evaluated symbolically.

Equation 4.6 is quadratic in overlap, h, and therefore, two solutions exist. Then, selecting numerical values for r_{base} and l_b, the solutions will only be a function of α_1 and δ. The solutions are evaluated for each (α_1, δ) pair, overlap values are computed, and the force finding method is employed to check if the unilateral element behavior is preserved. If unilateral element behavior is satisfied for one of the solutions, then this (α_1, δ) pair is stored with the overlap information. Finally, the combination of these points yields the equilibrium surface, and deployment is achieved by moving on it.

The procedure explained above is applied to a two-stage four-strut tensegrity boom. The length of struts and the radius of the circumscribing circle of top and bottom levels are chosen as the same as the previous example; $r_{base} = 0.1559$ m ($b = 0.27$ m) and $l_b = 0.4$ m. Then, equilibrium surfaces, one with respect to overlap and the other with respect to height, are generated and shown in Figure 4.14 and 4.15. The deployment path chosen is also visible on Figure 4.15 with initial and final parameters of $\alpha_{1,i} = 230°$, $\delta_i = 85°$, $\alpha_{1,f} = 210°$ and $\delta_f = 55°$

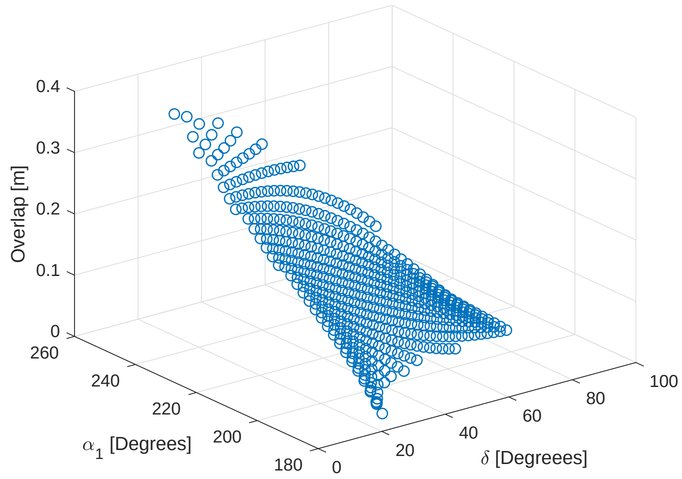

Figure 4.14: Equilibrium surface of four-strut SVD in terms of overlap

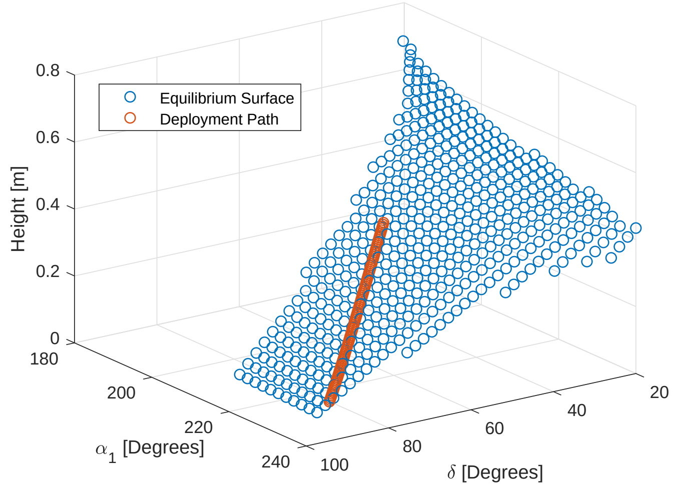

Figure 4.15: Equilibrium surface of four-strut SVD in terms of height

The deployment simulations are conducted with the selected initial and final parameters. The sequence of deployment simulation is shown in Figures 4.16, 4.17, 4.18, and 4.19. Similarly, force-densities in each type of member are tracked by the force finding method as the deployment proceeds. Figures 4.20 and 4.21 show the variation of the lengths of the elements and the force-densities in the structure, respectively.

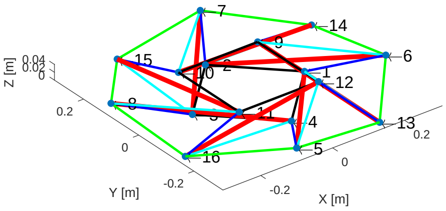

Figure 4.16: Deployment sequence, 1/4

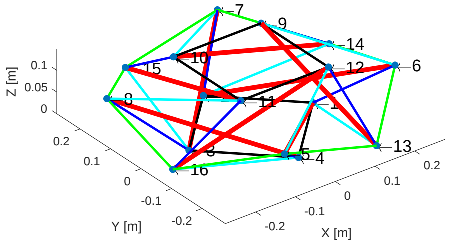

Figure 4.17: Deployment sequence, 2/4

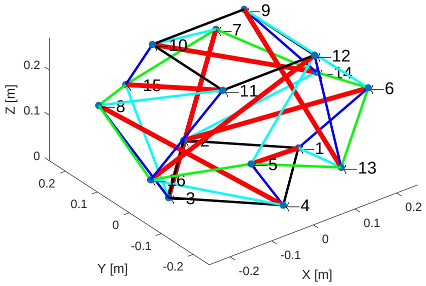

Figure 4.18: Deployment sequence, 3/4

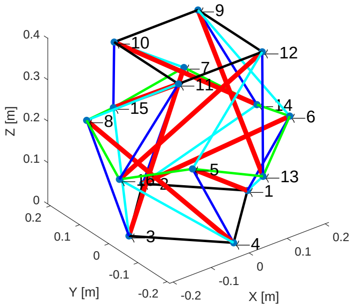

Figure 4.19: Deployment sequence, 4/4

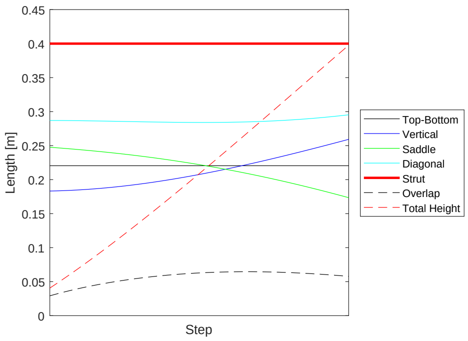

Figure 4.20: Variation of the lengths

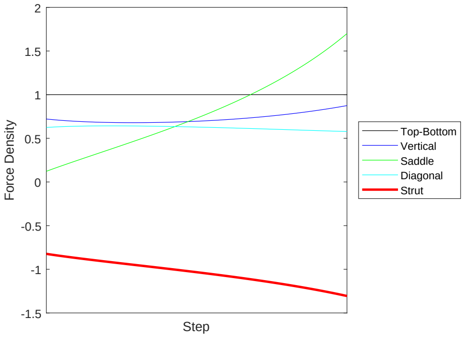

Figure 4.21: Variation of the force-densities

4.2 Deployment of Class-2 Tensegrity Booms

Tensegrity booms can also be constructed by stacking cylindrical tensegrity units on top of each other so that struts touch. Deployment of Class-2 cylindrical tensegrity booms was studied by Pinaud et al. [18], in which the tensegrity boom is constructed by stacking two triplex units. The units are connected to each other at nodes, therefore generating a Class-2 geometry. The same tensegrity units are placed in an alternating clockwise and anticlockwise sense in order to maintain symmetry in the xy plane.

The tensegrity boom studied by Pinaud et al. [18] is a two stage Class-2 cylindrical tensegrity boom that consists of three struts in each unit. The tensegrity boom has equilateral triangles at the bottom and top planes. Figures 4.22, 4.23, and 4.24 show the tensegrity boom and its top and side views, respectively. The structure has 6 struts and 21 cables (3 bottom, 3 top, 6 vertical, 3 saddle, and 6 optional reinforcing cables) and, due to symmetry, each group of elements carry the same force density. The groups of elements are illustrated in Figures 4.22, 4.23, and 4.24 by using different colors. Bottom and top cables, vertical cables, saddle cables, and struts are represented with black, blue, green, and thick red lines. Additionally, reinforcing cables are also indicated with orange dashed lines since they may not exist depending on the twist angle and the deployment strategy.

The prestressability conditions of Class-2 cylindrical tensegrity booms are satisfied if and only if the twist angle, α, between the two stacked units is defined as $\alpha = \frac{\pi}{6}$. On the other hand, the addition of reinforcing cables yields an interval

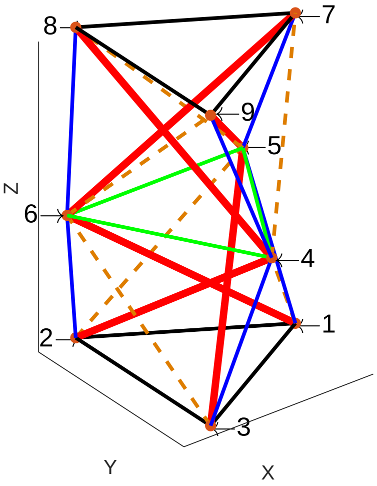

Figure 4.22: Two stage, three-strut Class-2 cylindrical tensegrity boom

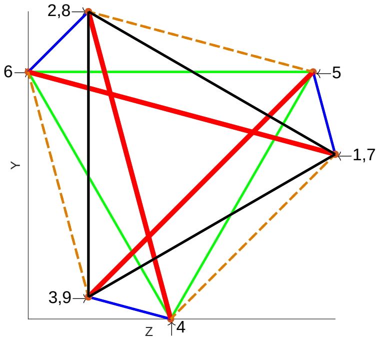

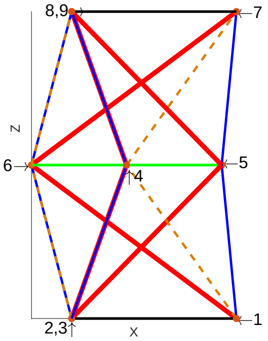

Figure 4.23: Class-2 tensegrity boom, Top view

Figure 4.24: Class-2 tensegrity boom, Side view

$\alpha = \left(\frac{\pi}{6}, \frac{\pi}{2}\right)$ for the twist angle that satisfies the prestressability conditions rather than a single value. It is possible to deploy Class-2 cylindrical tensegrity booms with and without employing reinforcing cables. These two deployment strategies are reviewed here.

Deployment with Constant Reinforcing Cables

Pinaud et al. [18] utilized reinforcing cables in order to reduce the number of actuators. The deployment strategy employed in their work is to keep the length of the reinforcing cables the same throughout the deployment. Since reinforcing cables are not actively controlled, the number of required actuators is reduced. Then, the deployment is achieved by varying the twist angle within the feasible range, resulting in a rotation and deployment of the structure.

In order to determine the configuration of the structure at any instance, it was found that the nodal locations can be represented in terms of four parameters. These parameters are as follows: the radii of circumscribing circles of the top and bottom triangles, r_{base}; the radius of circumscribing circle of the intersection plane, r; twist angle, α; and the height of one stage, h. Then, nodal locations can written as shown in Table 4.2.

Table 4.2: Nodal locations of two stage, three-strut Class-2 cylindrical tensegrity boom

	Nodes	x	y	z
Bottom Level	1	r_{base}	0	0
	2	$r_{base}\cos(\gamma)$	$r_{base}\sin(\gamma)$	0
	3	$r_{base}\cos(2\gamma)$	$r_{base}\sin(2\gamma)$	0
Intersection	4	$r\cos(\alpha-\gamma)$	$r\sin(\alpha-\gamma)$	h
	5	$r\cos(\alpha)$	$r\sin(\alpha)$	h
	6	$r\cos(\alpha+\gamma)$	$r\sin(\alpha+\gamma)$	h
Top Level	7	r_{base}	0	$2h$
	8	$r_{base}\cos(\gamma)$	$r_{base}\sin(\gamma)$	$2h$
	9	$r_{base}\cos(2\gamma)$	$r_{base}\sin(2\gamma)$	$2h$

where $\gamma = \frac{2\pi}{3}$ for Class-2 tensegrity booms with three struts per stage. During deployment, r_{base} remains constant while r decreases as the structure extends in order to keep the length of the struts constant. Figure 4.25 illustrates the parameters mentioned in Table 4.2 on the top view of the Class-2 tensegrity boom.

Using the node locations defined in Table 4.2, expressions for the lengths of the saddle, vertical and reinforcing cables can be found by calculating the distance between nodes. The saddle cable length can be calculated from the locations of nodes 4 and 5 as

$$S = \sqrt{\Big(r\cos(\alpha-\gamma) - r\cos(\alpha)\Big)^2 + \Big(r\sin(\alpha-\gamma) - r\sin(\alpha)\Big)^2} = r\sqrt{3} \qquad (4.13)$$

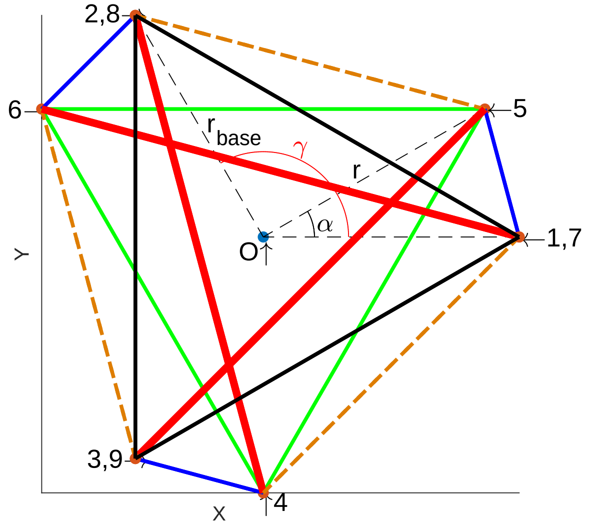

Figure 4.25: Illustration of α, γ, r_{base} and r

Similarly, the vertical cable length is calculated from the distance between the nodes 1 and 5.

$$V = \sqrt{\Big(r\cos(\alpha) - r_{base}\Big)^2 + \Big(r\sin(\alpha)\Big)^2 + h^2} \tag{4.14}$$

Finally, the reinforcing cable length can be found by calculating the distance between the nodes 1 and 4 as follows:

$$R = \sqrt{\Big(r\cos(\alpha-\gamma) - r_{base}\Big)^2 + \Big(r\sin(\alpha-\gamma)\Big)^2 + h^2} \tag{4.15}$$

Using the law of cosines, a relationship between r and h can be formed as follows:

$$(l_b - h)^2 = r_{base}^2 + r^2 - 2rr_{base}\cos\left(\frac{2\pi}{3} + \alpha\right) \tag{4.16}$$

Equation 4.16 can be solved using the quadratic formula, and the positive r solution can be obtained as

$$r = r_{base}\cos\left(\frac{2\pi}{3} + \alpha\right) + \sqrt{r_{base}^2\cos^2\left(\frac{2\pi}{3}\right) + l_b^2 - h^2 - r_{base}^2} \tag{4.17}$$

Then, Equation 4.17 can be substituted into Equation 4.15 to obtain an expression for R, which is independent of r. Assuming a constant length for reinforcing cables, R, a direct relationship between α and h can be formed.

After selection of r_{base} and l_b values, this relationship can be solved by using a Newton-Raphson Method for various fixed reinforcing cable lengths. The results are represented by solution curves shown in Figure 4.26 with parameters $r_{base} = 3.45$ cm and $l_b = 12.8$ cm.

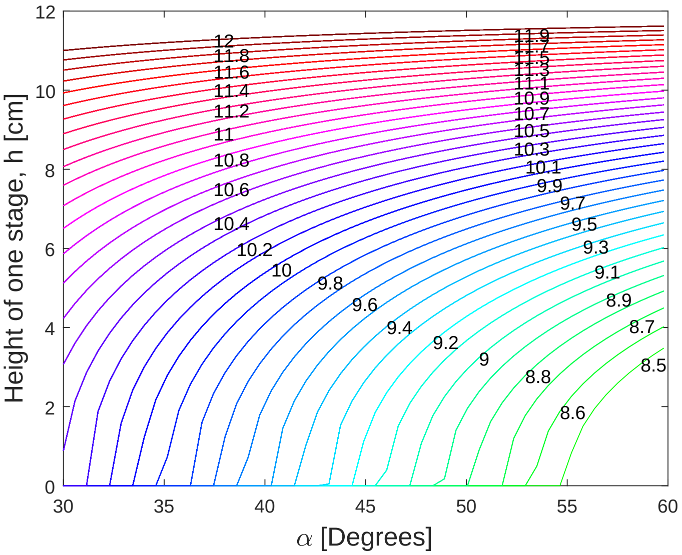

Figure 4.26: The relationship between α and h

Figure 4.26 shows that with a fixed reinforcing cable length, the height of one stage increases with an increasing twist angle. Therefore, by varying the twist angle, deployment can be achieved. Even though the feasible range for α is reported to be $\alpha = \left(\frac{\pi}{6}, \frac{\pi}{2}\right)$, the solutions are given in the $\alpha = \left(\frac{\pi}{6}, \frac{\pi}{3}\right)$. The reason for that is struts intersect at the center, and it is not physically possible to increase α further.

This deployment strategy is limited by the constant lengths of reinforcing cables. Each curve has an upper limit to which the structure can be deployed. From Figure 4.26, the constant reinforcing cable length is chosen as $R = 10$ cm and, with selections of $\alpha_i = 34$ ° and $\alpha_f = 55$ °, deployment is simulated. Figures 4.27, 4.28, 4.29 and 4.30 show the deployment sequence.

Similarly, using a force finding method, force-densities in each element are tracked during deployment. The length variation of elements and the force-density variation are shown in Figures 4.31 and 4.32, respectively.

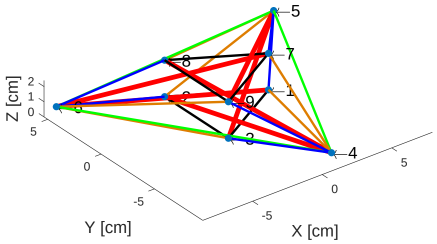

Figure 4.27: Deployment sequence, 1/4

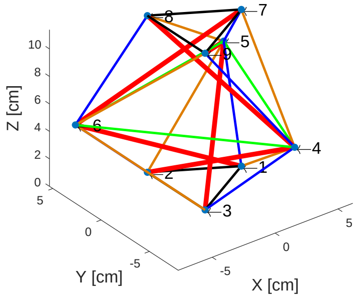

Figure 4.28: Deployment sequence, 2/4

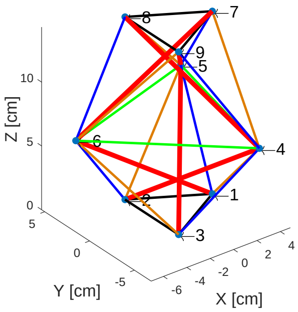

Figure 4.29: Deployment sequence, 3/4

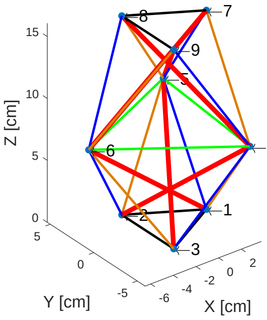

Figure 4.30: Deployment sequence, 4/4

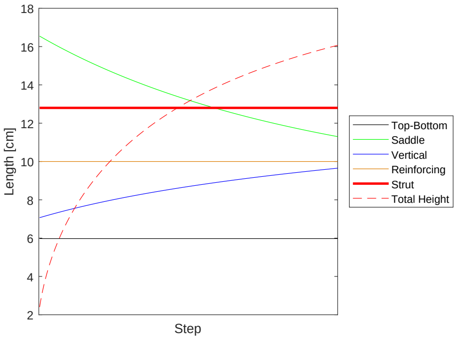

Figure 4.31: Variation of the lengths

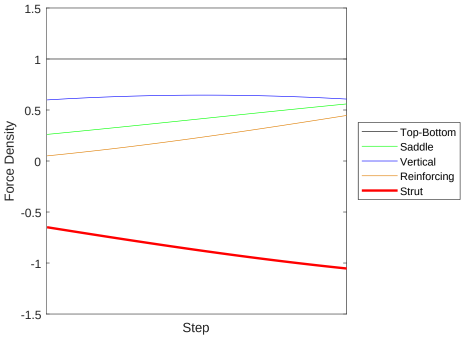

Figure 4.32: Variation of the force-densities

In general, addition of constant reinforcing cables serves two purposes. The first of which is to obtain a non-unique twist angle which can be varied to achieve deployment. The other is to increase stiffness of the structure by locking infinitesimal mechanism modes. Therefore, a potentially higher stiffness-to-mass ratio can be obtained [18]. However, even if the use of constant reinforcing cables provides a strategy for deployment of Class-2 tensegrity booms, the introduced complexities may decrease the maximum possible final-to-initial height ratio since reinforcing cables are constant.

Deployment without Constant Reinforcing Cables

Another deployment strategy for cylindrical Class-2 tensegrity booms which is not limited by the constant reinforcing cable length is explained here. This deployment strategy can be applied to Class-2 tensegrity booms with or without reinforcing cables. In this deployment strategy, if reinforcing cables are not used, the twist angle has to be set to $\alpha = \frac{\pi}{6}$ during deployment in order to satisfy the prestressability conditions. On the other hand, if they are introduced to the structure, the twist angle can be selected from the feasible range given previously.

The height of one stage, h, can be found by calculating the distance between two nodes connected by a strut as follows:

$$h = \sqrt{l_b^2 + (x_a - x_b)^2 + (y_a - y_b)^2} \tag{4.18}$$

where a and b denote the end nodes of any strut. As the deployment occurs, the height of one stage increases, affecting the position of the nodes in the intermediate plane. Since x and y components of these nodes are not independent from each other, the radius of the circumscribing circle of the intermediate plane, r, can be solved from Equation 4.18 and Table 4.2. In this way, the position of each node can be found at any instance, and the deployment can be simulated.

Using the relationship given in Equation 4.18, the initial and final heights of the tensegrity boom are selected as $h_i = 1$ cm and $h_f = 10$ cm, and the deployment is simulated. The deployment sequence for the same tensegrity boom without reinforcing cables can be seen in Figures 4.33, 4.34, 4.35, and 4.36. Similar to previous deployment simulations, variations of lengths and force-densities are also provided in Figures 4.37 and 4.38.

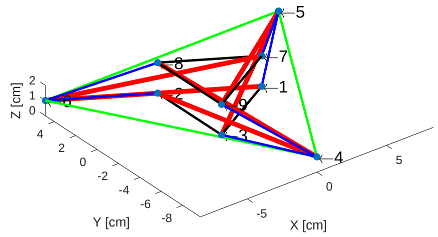

Figure 4.33: Deployment sequence, 1/4

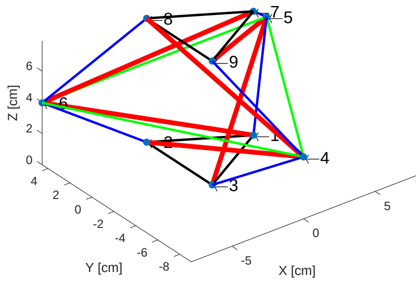

Figure 4.34: Deployment sequence, 2/4

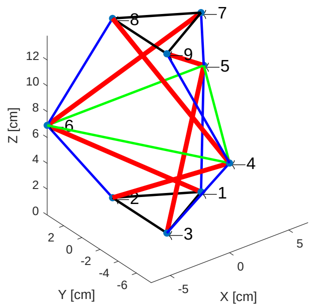

Figure 4.35: Deployment sequence, 3/4

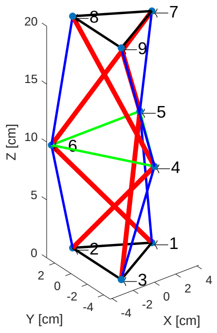

Figure 4.36: Deployment sequence, 4/4

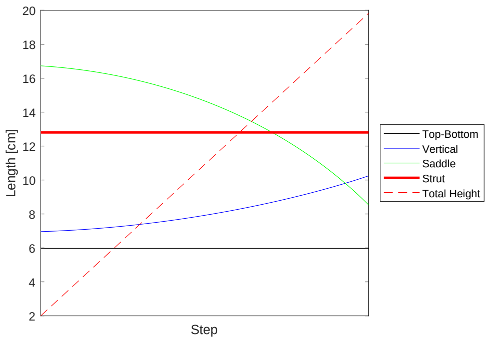

Figure 4.37: Variation of the lengths

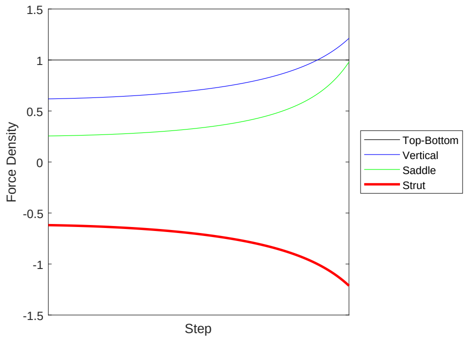

Figure 4.38: Variation of the force-densities

In the next section, the latter deployment strategy is generalized for n-strut tensegrity booms. Since it also can be applied to tensegrity booms with reinforcing cables, it is found to be more favorable. On the other hand, the applicability of the first deployment strategy is very limited for an increased number of struts in each stage, and it is found to be not very efficient. The ratio between the maximum height and the initial height decreases with an increased number of struts; therefore, the first deployment strategy is abandoned, and more attention is paid to the latter one.

4.2.1 Deployment of n-strut Class-2 Tensegrity Booms

A generalization procedure is developed for deployment of Class-2 cylindrical tensegrity booms as well by following a pattern for nodal locations similar to the one given in Table 4.1. In order to provide a full generalization procedure, connectivity information has to be defined for Class-2 tensegrity booms. As a result, a Class-2 tensegrity boom with an n-strut in each stage can be created.

The generalization procedure starts with defining the nodal locations in terms of the following: radii of the circumscribing circles of bottom and top planes; radius of the circumscribing circle of the intermediate plane; and the twist angle. The radius of the circumscribing circle of the intermediate plane can be obtained from the relation given in Equation 4.18 at any instant for a given length of struts. Table 4.3 shows the pattern of nodal locations of Class-2 cylindrical tensegrity booms with n struts in each stage. These types of tensegrities typically have $3n$ nodes (n nodes in each level) and $7n$ or $9n$ elements depending on the presence of reinforcing cables.

where $\gamma = \frac{2\pi}{n}$, r_{base} is the radii of the circumscribing circles of bottom and top levels, r is the radius of the circumscribing circle of intermediate level and h is the height of one stage. On the other hand, the twist angle is $\alpha = \frac{\pi}{2} - \frac{\pi}{n}$. However, the addition of reinforcing cables defines a feasible range for twist angle $\alpha = (\frac{\pi}{2} - \frac{\pi}{n}, \frac{\pi}{2})$ rather than a single value.

Table 4.3: Node locations of a two stage cylindrical Class-2 tensegrity boom

	Node	x	y	z
Bottom Level	1	r_{base}	0	0
	2	$r_{base}\cos(\gamma)$	$r_{base}\sin(\gamma)$	0
	3	$r_{base}\cos(2\gamma)$	$r_{base}\sin(2\gamma)$	0
	$\cdots$	$\cdots$	$\cdots$	0
	n-1	$r_{base}\cos((n-2)\gamma)$	$r_{base}\sin((n-2)\gamma)$	0
	n	$r_{base}\cos((n-1)\gamma)$	$r_{base}\sin((n-1)\gamma)$	0
Intermediate Level	n+1	$r\cos(\alpha-\gamma)$	$r\sin(\alpha-\gamma)$	h
	n+2	$r\cos(\alpha)$	$r\sin(\alpha)$	h
	n+3	$r\cos(\alpha+\gamma)$	$r\sin(\alpha+\gamma)$	h
	$\cdots$	$\cdots$	$\cdots$	h
	2n-1	$r\cos(\alpha+(n-3)\gamma)$	$r\sin(\alpha+(n-3)\gamma)$	h
	2n	$r\cos(\alpha+(n-2)\gamma)$	$r\sin(\alpha+(n-2)\gamma)$	h
Top Level	2n+1	r_{base}	0	$2h$
	2n+2	$r_{base}\cos(\gamma)$	$r_{base}\sin(\gamma)$	$2h$
	2n+3	$r_{base}\cos(2\gamma)$	$r_{base}\sin(2\gamma)$	$2h$
	$\cdots$	$\cdots$	$\cdots$	$2h$
	3n-1	$r_{base}\cos((n-2)\gamma)$	$r_{base}\sin((n-2)\gamma)$	$2h$
	3n	$r_{base}\cos((n-1)\gamma)$	$r_{base}\sin((n-1)\gamma)$	$2h$

The number of stages may be increased readily by extending Table 4.3. It is obvious that the nodes will overlap each other in xy plane in every second level. For example, two more stages can be added directly by copying the nodal locations of the intermediate and top level except for their positions in z direction. The height of each added level will be greater than the previous one by h. In order to define the full geometry of the tensegrity structure, a connectivity chart is presented in Figure 4.39.

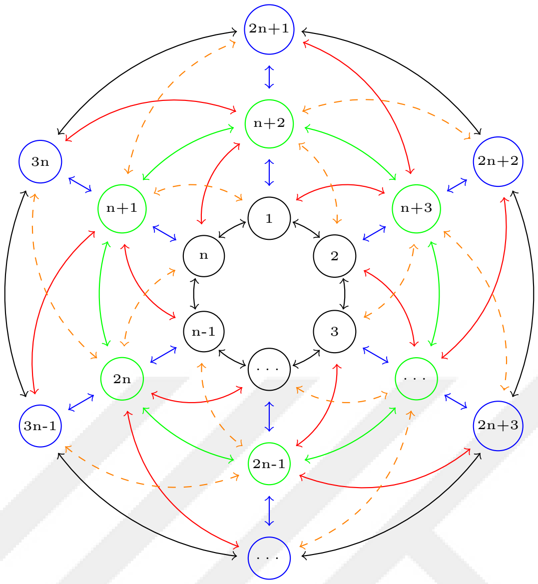

Figure 4.39: Connectivity chart for Class-2 tensegrity booms

In Figure 4.39, each node is represented with a circle, and the edge color of each circle indicates which level the node belongs to. Bottom, top, and intermediate levels are indicated with black, blue, and green circles. Furthermore, each double-headed arrow defines a connection between the corresponding nodes. Three circular layers are generated to account for the bottom, top, and intermediate levels. In order to get a clearer picture of the connectivity by preventing overlapping between arrows, the first nodes of the bottom and top levels are located at the upper point of the layer such as 1 and $2n + 1$, while the intermediate layer is rotated in the counter-clockwise direction. Black, blue, green, dashed orange, and red lines represent top and bottom, vertical, saddle, reinforcing cables (optional), and struts, respectively.

The deployment strategy which employs constant reinforcing cables is applied to a four-strut Class-2 tensegrity boom with $r_{base} = 3.45$ cm and $l_b = 12.8$ cm. In order to determine the relationship between the twist angle and the height of one stage, an expression for the constant reinforcing cable length can be obtained by calculating the distance between nodes 1 and 4. Using the law of cosines, the relationship between r and h can be formed as

$$(l_b - h)^2 = r_{base}^2 + r^2 - 2rr_{base}\cos\left(\frac{\pi}{2} + \alpha\right) \tag{4.19}$$

which can be solved for r using the quadratic formula as follows:

$$r = r_{base}\cos\left(\frac{\pi}{2}+\alpha\right)+\sqrt{-h^2+l_b^2-\frac{1}{2}r_{base}^2-\frac{1}{2}r_{base}^2\cos(2\alpha)} \tag{4.20}$$

The expression obtained for r can be substituted into the expression of reinforcing cable length, and the solution curves are obtained. The feasible twist angle range is $\alpha = \left(\frac{\pi}{4},\frac{\pi}{2}\right)$, and the solution curves are shown in Figure 4.40.

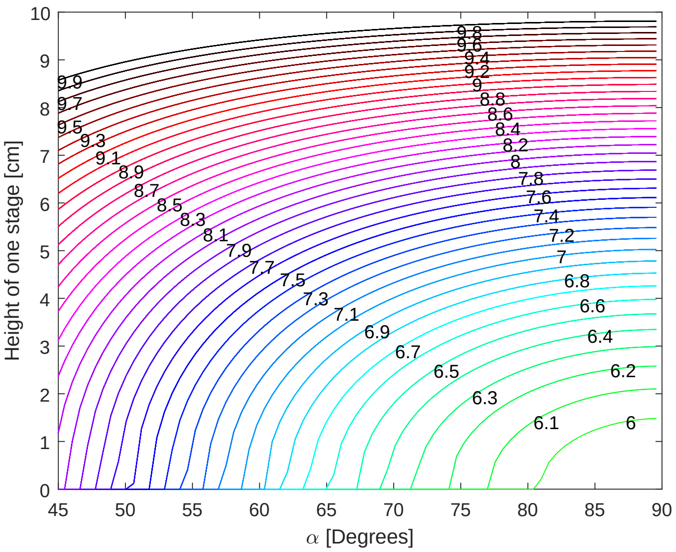

Figure 4.40: The relationship between α and h, n=4

Then, the constant reinforcing cable length is chosen as $R = 8.1$ cm, and the initial and final twist angle are selected as $\alpha_i = 46°$ and $\alpha_f = 80°$; the deployment is simulated. Figures 4.41, 4.42, 4.43, and 4.44 illustrate the deployment sequence.

Similarly, the variation of lengths and force-densities are also shown in Figures 4.45 and 4.46.

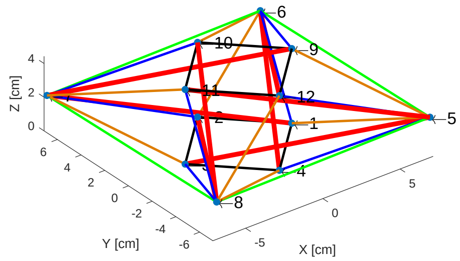

Figure 4.41: Deployment sequence, 1/4

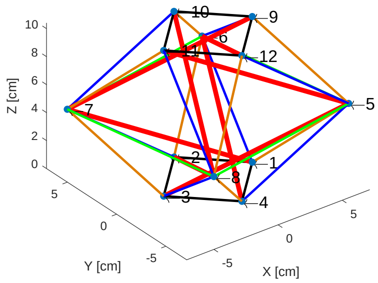

Figure 4.42: Deployment sequence, 2/4

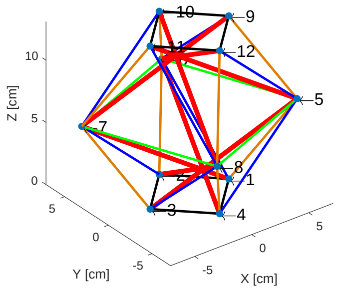

Figure 4.43: Deployment sequence, 3/4

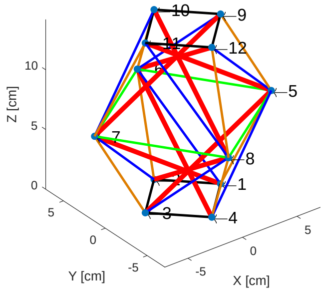

Figure 4.44: Deployment sequence, 4/4

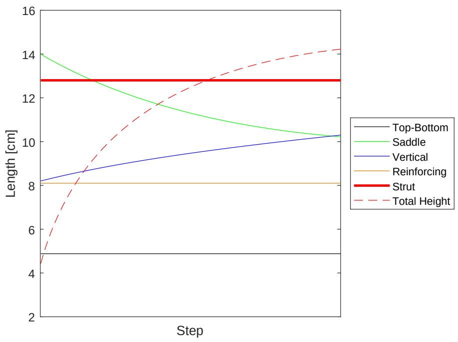

Figure 4.45: Variation of the lengths

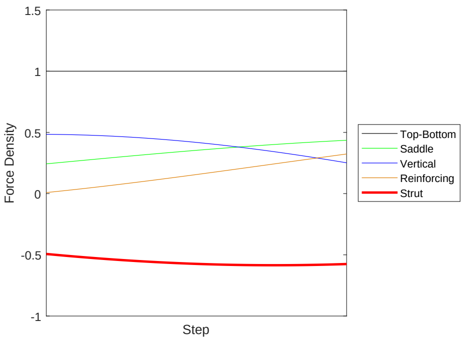

Figure 4.46: Variation of the force-densities

The deployment strategy without constant reinforcing cables can be applied by using the parametric form of the nodal locations, which allows deployment to be achieved by varying the height of one stage and calculating the positions of the nodes in the intermediate plane. Equation 4.18 is used to determine the x and y positions of the intermediate nodes. Since x and y components are directly related to r, as the height increases, the radius of the circumscribing circle of the intermediate plane decreases.

This generalization procedure is applied to the same four-strut Class-2 tensegrity boom, and the deployment is simulated. For demonstration purposes, the tensegrity boom is assumed to have actively controlled reinforcing cables and a twist angle of $\alpha = \frac{\pi}{3}$. Then, the initial and final height of one stage are selected as $h_i = 1$ cm and $h_f = 10$ cm, and the deployment is simulated as shown in Figures 4.47, 4.48, 4.49, and 4.50. Variation of lengths and force-densities of elements are also shown in Figures 4.51 and 4.52.

In the next chapter, the deployment strategies described here are utilized to devise a novel deployment strategy which involves a transformation. This novel deployment strategy employs Class-1 and Class-2 deployment in order to exploit high packaging density and improved stiffness. It may be used to provide a solution to realization of deployment tensegrity structures in space and increase their utilization.

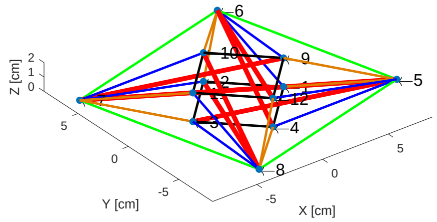

Figure 4.47: Deployment sequence, 1/4

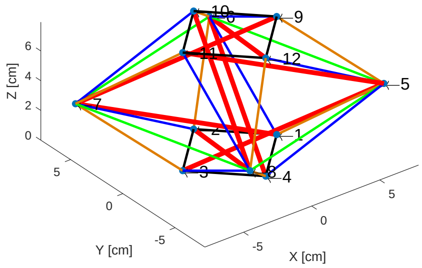

Figure 4.48: Deployment sequence, 2/4

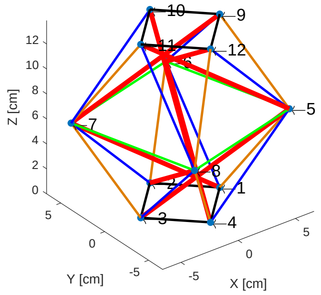

Figure 4.49: Deployment sequence, 3/4

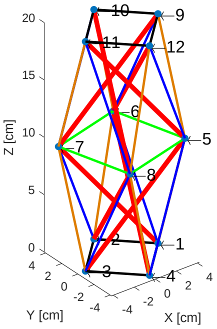

Figure 4.50: Deployment sequence, 4/4

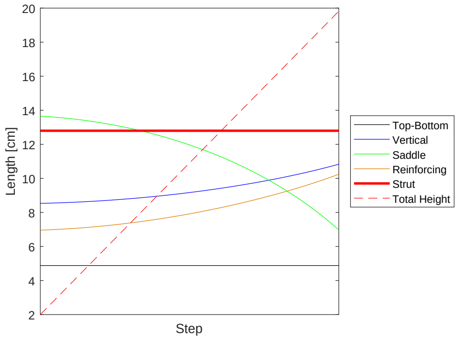

Figure 4.51: Variation of the lengths

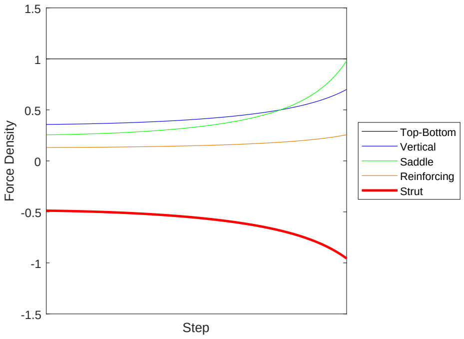

Figure 4.52: Variation of the force-densities

Chapter 5
A Novel Deployment Strategy Involving Transformation

Tensegrity structures typically suffer from inferior stiffness when they are deployed in Class-1 configuration since there is no contact between hard members, struts [21]. On the other hand, employing a Class-1 configuration results in high packing density; and therefore, the initially packed configuration can be stowed into very small volumes. However, the low stiffness when deployed creates an obstacle for their realization in space applications.

Contrary to Class-1 configurations, Class-k tensegrity configurations offer better stiffness properties due to the jointed connection between struts at nodes, as noted by many researchers [21,67]. However, this jointed connection also limits the packing capabilities of Class-k tensegrities. For a Class-k configuration, the angle between two connected struts cannot be lower than a certain value due to cross-sectional areas of struts and/or imperfections in ball joints.

In this section, a novel deployment strategy is proposed for tensegrity structures. The proposed deployment strategy aims to initially maintain high packing density and to obtain better stiffness properties by going through a transformation from Class-1 to Class-2 as deployment occurs. As a result, this deployment strategy can be utilized to design and deploy tensegrity booms without discarding high stiffness or high packing density.

The developed adaptive tensegrity boom starts as a Class-1, and as it is deployed, some of the cables are shortened until struts touch each other at the ends and are locked. In this way, the structure transforms into a Class-2 tensegrity while maintaining high packing density in the beginning.

The initial step in devising such a deployment strategy is to determine the initial and final tensegrity configurations. The configurations have to show some similarities to make a transformation possible between them. Since the idea behind the transformation is to shorten some of the cables to zero length, cable mode deployment should be employed. During deployment and transformation, the self-equilibrated geometry must be retained in order to avoid reduced stiffness or even collapse, having at least one stable state of self-stress. Significant attention should be paid, or cables could go slack and the structure could collapse.

The initial configuration of the tensegrity boom is selected as a three-strut SVD structure investigated by Sultan [61, 66], and the final configuration is chosen as a three-strut Class-2 tensegrity boom including reinforcing cables, examined by Pinaud et al. [18]. The selected geometries are shown in Figures 5.1 and 5.2.

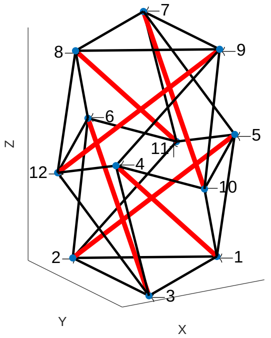

Figure 5.1: Three-strut SVD tensegrity boom

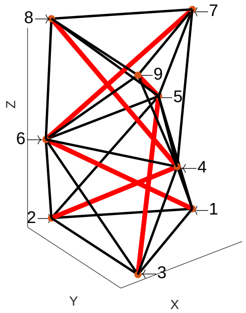

Figure 5.2: Three-strut Class-2 tensegrity boom

The resemblance between the two structures allows a transformation between them by shortening three saddle cables to zero length. Cables between nodes 4-10, 5-11, and 6-12 can be shortened, and struts touch each other and are locked. Nevertheless, the deployment strategy remains complex due to several restrictions.

Since the tensegrity boom is Class-1 initially, its configuration is governed by the equilibrium surface. After the initial deployment on the equilibrium surface, in order to prevent loss of the self-stress state, additional reinforcing cables are required. These reinforcing cables are added to the structure slackly and activated at the end of the initial deployment phase by shortening them until they are neither slack nor carrying pre-stress, discarding the dependence on the equilibrium surface. The next step is to satisfy the twist angle condition for a self-equilibrated

Class-2 tensegrity boom for the upcoming transformation phase. Therefore, the intermediate plane needs to be rotated until the twist angle is in the determined allowable range, which was defined previously. When the required rotation is completed, the transition from Class-1 to Class-2 can begin. The corresponding saddle cables can be shortened until the struts touch each other at the nodes and are locked. Finally, the structure becomes Class-2, and further deployment can be executed.

The phases of the deployment strategy can be summarized as follows:

1. Initial Deployment of the Class-1 Tensegrity Boom
2. Activation of the Reinforcing Cables
3. Rotation of the Intermediate Plane
4. Transition from Class-1 to Class-2
5. Final Deployment of the Class-2 Tensegrity Boom

5.1 Deployment Simulations

Deployment simulations begin with the free selection of the radii of the circumscribing circles of the top and bottom planes, r_{base}, and the lengths of the struts, l_b. Selecting $r_{base} = 3.45$ cm and $l_b = 12.8$ cm, the equilibrium surfaces with respect to overlap and total height are given in Figures 5.3 and 5.4, respectively.

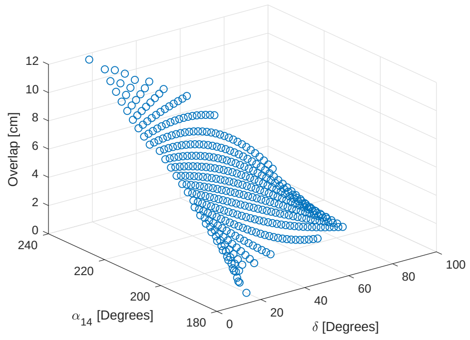

Figure 5.3: Equilibrium surface in terms of overlap

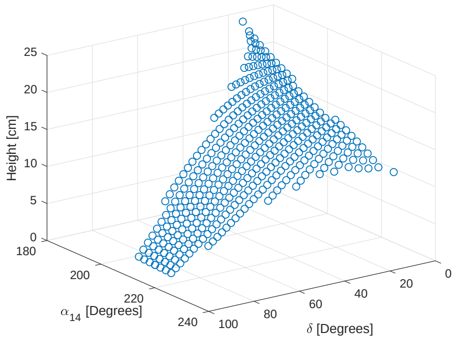

Figure 5.4: Equilibrium surface in terms of total height

The parameters for initial deployment are chosen as $\alpha_{14,i} = 216°$, $\delta_i = 88°$, $\alpha_{14,f} = 207°$, and $\delta_f = 60°$. The deployment path is shown in Figure 5.5 on the equilibrium surface with respect to total height.

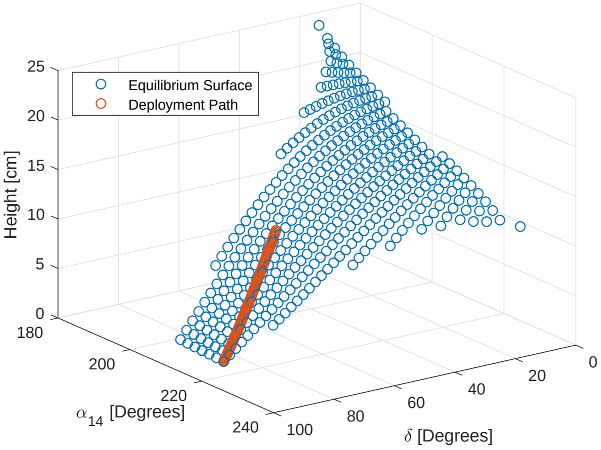

Figure 5.5: Initial deployment path on the equilibrium surface

For clarity in the following figures of deployment simulations; black, blue, green, teal, and orange lines represent the top and bottom, vertical, saddle, diagonal, and reinforcing cables, respectively. In addition, struts are denoted with thick red lines. The sequence of the initial deployment simulation can be seen in Figures 5.6, 5.7, 5.8, and 5.9.

Figures 5.10 and 5.11 show the variation of the lengths of and the force-densities carried by the elements in the structure, respectively. Figure 5.10 reveals that the top and bottom cables as well as the struts maintain their lengths, while saddle cables are shortened. The variation of the force-densities, Figure 5.11, shows that cables and struts are always under tension and compression, respectively.

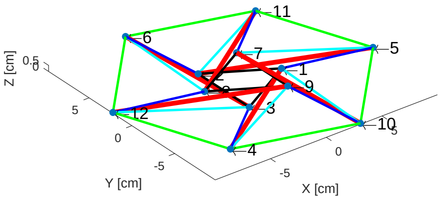

Figure 5.6: Initial deployment, 1/4

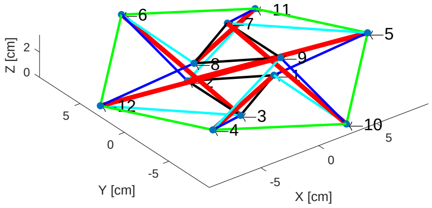

Figure 5.7: Initial deployment, 2/4

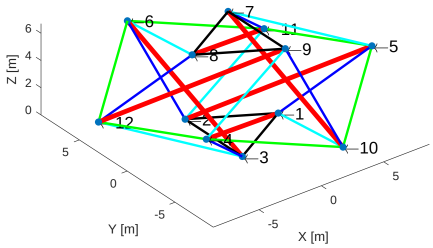

Figure 5.8: Initial deployment, 3/4

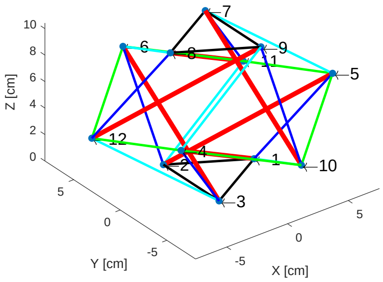

Figure 5.9: Initial deployment, 4/4

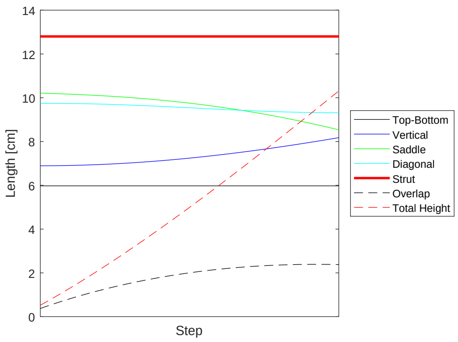

Figure 5.10: Variation of the lengths

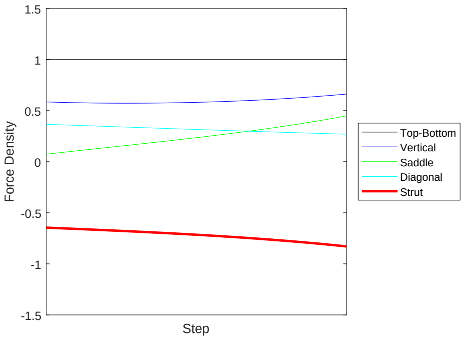

Figure 5.11: Variation of the force-densities

Figure 5.10 shows that the initial configuration has almost zero height, which explains the selection of $\alpha_{14,i}$ and δ_i. Once the initial Class-1 deployment is achieved, the reinforcing cables (in orange) are activated, as shown in Figure 5.12.

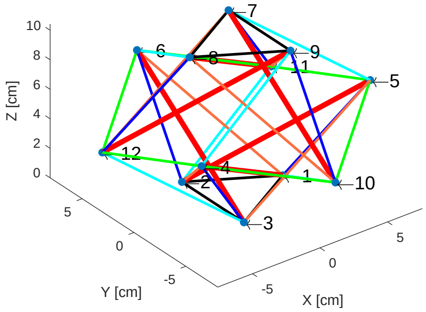

Figure 5.12: Activation of the reinforcing cables

Then, in order to satisfy the twist angle range constraint for the Class-2 tensegrity boom, the middle plane (lower and upper intersection) starts to rotate until the twist angle reaches $\frac{5\pi}{12}$, which is in the feasible range of the twist angle defined previously. This twist angle is determined arbitrarily, which allows the rest of the deployment to be accomplished without losing the state of self-stress. Even though the feasible twist angle range is defined as $(\frac{\pi}{6}, \frac{\pi}{2})$, collision between struts occurs at $\frac{\pi}{3}$. Considering this fact and any possible cable entanglements, the twist angle is selected to be between $(\frac{\pi}{3}, \frac{\pi}{2})$. As a result, this rotation sequence is illustrated in Figures 5.13, 5.14, 5.15, and 5.16.

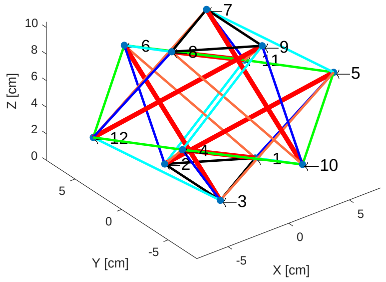

Figure 5.13: Rotation Phase, 1/4

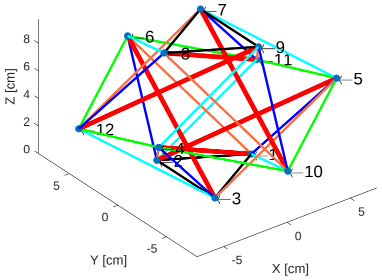

Figure 5.14: Rotation Phase, 2/4

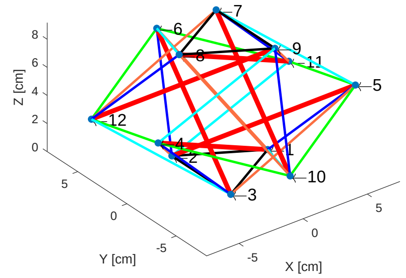

Figure 5.15: Rotation Phase, 3/4

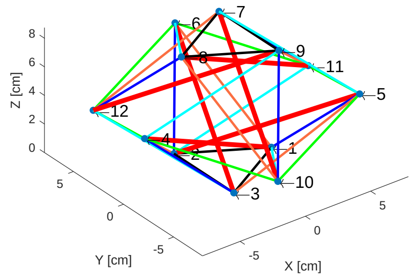

Figure 5.16: Rotation Phase, 4/4

Similar to initial deployment, variation of the lengths of the elements are tracked and are shown in Figure 5.17 as well as the force-densities carried by the elements as in Figure 5.18.

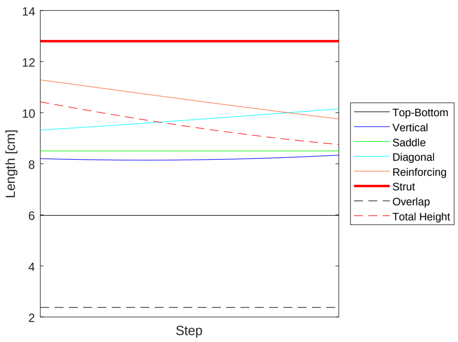

Figure 5.17: Variation of the lengths

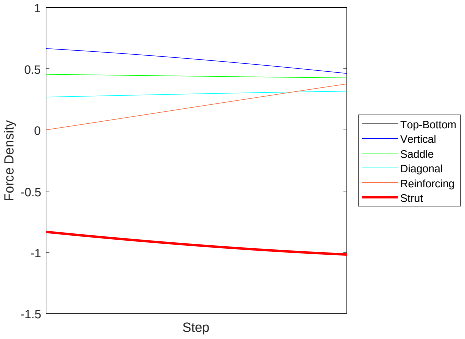

Figure 5.18: Variation of the force-densities

Figure 5.17 shows that the total height of the tensegrity boom initially decreases and comes to a rest as the rotation occurs. On the contrary, the overlap is not affected by the rotation since the intermediate plane is rotated as a whole without any distortion. Figure 5.18 illustrates the level of force-densities carried by each group of element. Additionally, it shows that the force-densities carried by the reinforcing cables start from zero and increase. This means the reinforcing cables are redundant before the rotation sequence begins. The rotation sequence is a very important step for the transformation, and it makes the configuration drift away from the equilibrium surface obtained before, meaning that the structure loses the state of self-stress. The actual reason of the introduction of the reinforcing cables is to make the rotation sequence possible by increasing the number of states of self-stress.

When the rotation is completed, the transition between Class-1 and Class-2 starts. In this case, nodes 4, 5, and 6 maintain their locations and nodes 10, 11, and 12 approach nodes 4, 5, and 6, respectively. The transition sequence is shown in Figures 5.19, 5.20, 5.21, and 5.22.

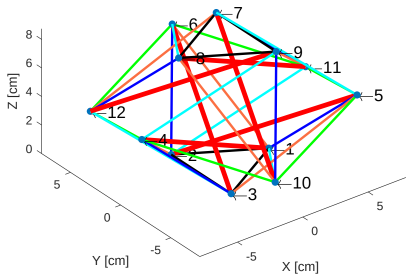

Figure 5.19: Transition Phase, 1/4

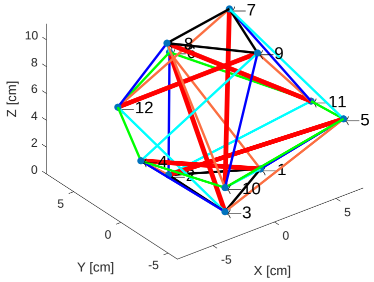

Figure 5.20: Transition Phase, 2/4

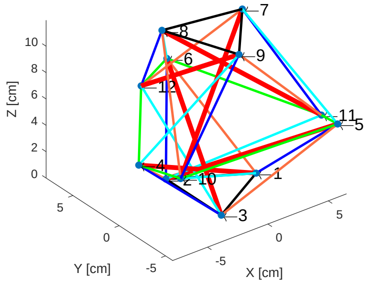

Figure 5.21: Transition Phase, 3/4

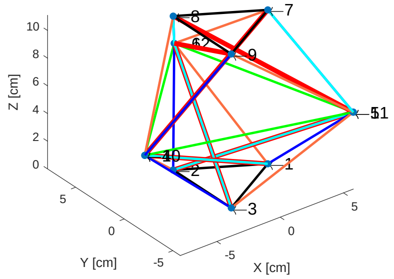

Figure 5.22: Transition Phase, 4/4

Similarly, Figures 5.23 and 5.24 show the variation of element lengths and the normalized force-densities in the elements. Figure 5.23 reveals that the transition sequence is not symmetric since the same type of cables in different stages have different lengths and force densities. Therefore, the number of groups in the structure increases. Since three saddle cables are shortened to zero length while the other three fill their gap simultaneously, asymmetric reconfiguration makes the same members of the group of elements act differently in different stages. The distinction between these groups is visible in Figures 5.23 and 5.24 in terms of both length and force density. Since the force-densities are force-per-unit length by definition, as the lengths of one group of saddle cables approach zero, the force-densities increase significantly. However, the actual pre-stress carried by that group of cables is of the same order of magnitude of the pre-stress in other elements.

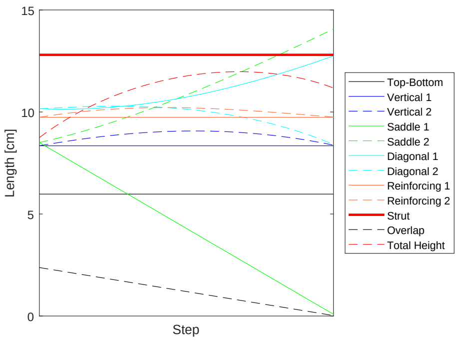

Figure 5.23: Variation of the lengths

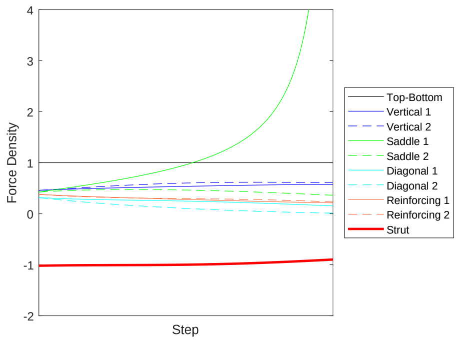

Figure 5.24: Variation of the force-densities

Explicitly, each group of vertical and reinforcing cables creates two different groups during the transition phase. However, at the end of this phase, their lengths become the same again, satisfying the symmetrical shape. On the other hand, two groups created by the diagonal cables coincide with different types of elements. For instance, in the bottom stage, the diagonal cables coincide with struts while in the top stage, the diagonal cables coincide with the vertical cables. Therefore, as they approach very close to each other, motors can increase the length of one kind of cable, preferably diagonal cables, to allow them go slack. In this way, the connectivity of the structure changes, and when the struts touch each other at nodes, the structure becomes a Class-2 tensegrity boom as shown in Figure 5.25.

Now, the resulting configuration is a Class-2 tensegrity system, and since all of the cables are actively controlled so far, there is no restriction on the number of actuators. Therefore, the final deployment can be executed by actuating all cables until r is approximately the same as r_{base} to obtain a uniform cross section along the longitudinal axis, which will be referred to as *full deployment*. The final deployment sequence is shown in Figures 5.26, 5.27, 5.28, and 5.29. Additionally, Figures 5.30 and 5.31 show the variation of lengths of and force densities in elements.

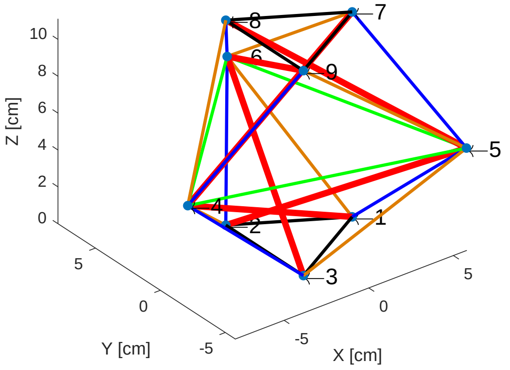

Figure 5.25: Transformed Class-2 tensegrity boom

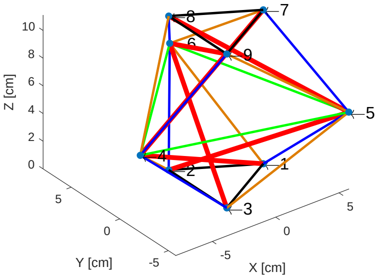

Figure 5.26: Final Deployment, 1/4

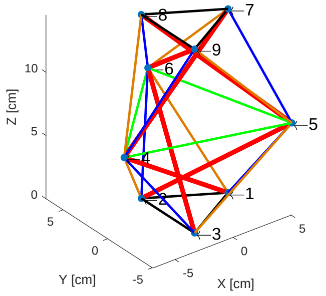

Figure 5.27: Final Deployment, 2/4

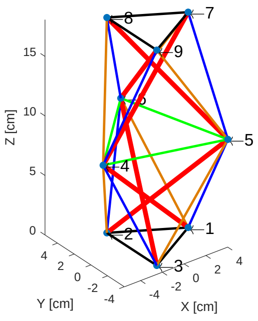

Figure 5.28: Final Deployment, 3/4

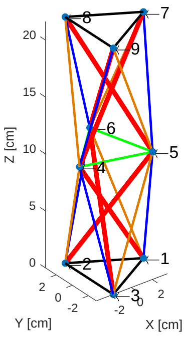

Figure 5.29: Final Deployment, 4/4

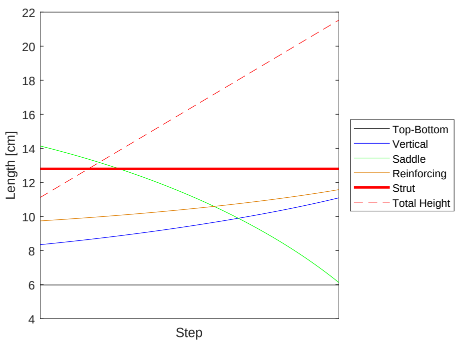

Figure 5.30: Variation of the lengths

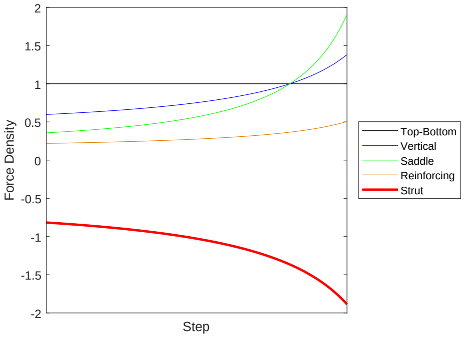

Figure 5.31: Variation of the force-densities

As a result, the final configuration becomes a Class-2 tensegrity boom with additional *reinforcing cables*. Strut-to-strut contact occurs, and bending stiffness of the tensegrity boom is increased. Furthermore, the number of mechanism modes is also decreased due to the addition of reinforcing cables, and infinitesimal mechanisms are locked. Another important feature of this deployment strategy is the increment of the total height. The overlap found in Class-1 tensegrity configuration is not necessary anymore and during transformation this overlap adds to the total height of the structure, increasing the deployment efficiency in terms of the ratio between the final height and the initial height of the boom.

5.2 Stiffness Comparison

In order to justify the claim of bending stiffness improvement, two differently deployed tensegrity booms are investigated using nonlinear finite element analyses. The first example is the Class-1 SVD boom and the second example is the transformed Class-2 tensegrity boom examined in this chapter. Final configurations are selected in such a way that they resemble a cylindrical boom with a constant radius. Since the radii of the circumscribing circles of the top and bottom planes are constant, this resemblance is controlled by the radius of the circumscribing circle of the intermediate plane. The deployment of the first example starts with the same Class-1 tensegrity boom given in Figure 5.6 and is achieved by moving on the equilibrium surface until the radius of the circumscribing circle of the intermediate plane is almost equal to r_{base}. The initial and final azimuth and declination angles are selected as $\alpha_{14,i} = 216°$, $\delta_i = 88°$, $\alpha_{14,f} = 197°$, and $\delta_f = 31°$, and the deployment sequence is shown in Figures 5.32, 5.33, 5.34, and 5.35.

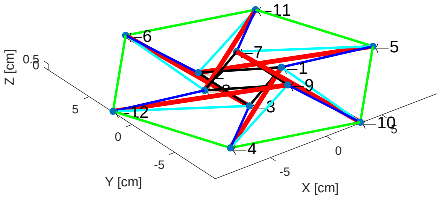

Figure 5.32: Class-1 Deployment, 1/4

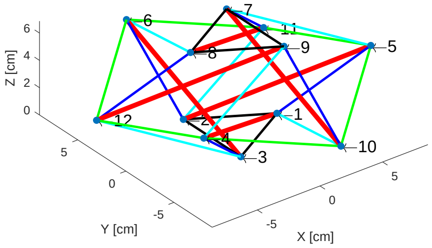

Figure 5.33: Class-1 Deployment, 2/4

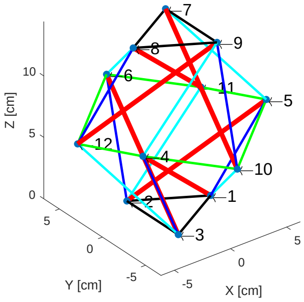

Figure 5.34: Class-1 Deployment, 3/4

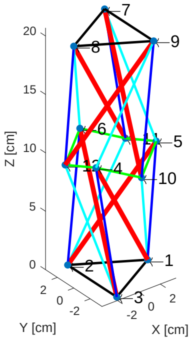

Figure 5.35: Class-1 Deployment, 4/4

Similarly, the variation of the lengths of the members and the force-densities carried by the elements are shown in Figures 5.36 and 5.37.

Nonlinear finite element analyses are conducted to compare the bending stiffness properties of the two aforementioned tensegrity booms in Figures 5.29 and 5.35. The cross sectional areas of cables and struts are chosen as 10 mm^2 and 1 cm^2, respectively. Cables and struts are assumed to be made of steel and aluminum with modulus of elasticity of 200 GPa and 70 GPa. The bottom nodes of the booms are completely fixed, and 25 N, 250 N, and 500 N of nodal forces are applied at the top nodes generating three different load cases. The loading conditions, which simulate bending around x and y axes are depicted in Figure 5.38 with dashed and solid lines, respectively.

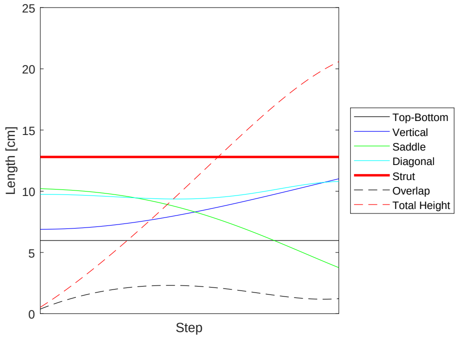

Figure 5.36: Variation of the lengths

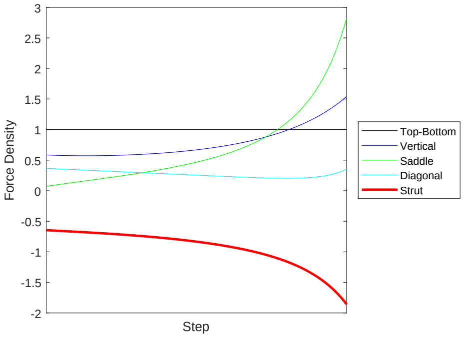

Figure 5.37: Variation of the force-densities

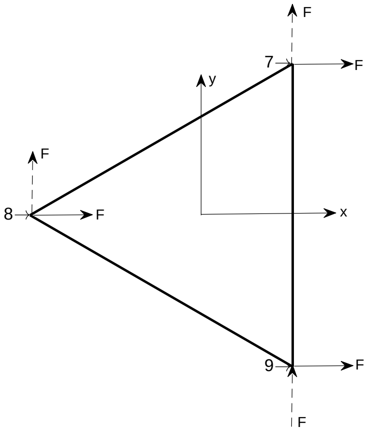

Figure 5.38: Top plane of the tensegrity booms showing the loading conditions

The normalized force-densities carried by the elements are multiplied by the pre-stress coefficient and the length of each element to determine the pre-stress force. The pre-stress coefficient is chosen in such a way that the struts carry 1 kN of pre-stress in each case. The length of each type of element and the pre-stress forces carried by them are given in Table 5.1.

The displacement of the center of the top plane in the corresponding direction, which will be referred to as tip displacement, is obtained from nonlinear finite element analyses, and the results are given in Table 5.2 for fully deployed SVD and transformed Class-2 tensegrity booms. It is revealed that for each loading condition, the tip displacement is decreased with the proposed transformation between Class-1

Table 5.1: Pre-stress in each type of element

	Fully Deployed SVD		Transformed Class-2	
Element	**Length** [cm]	**Pre-stress** [N]	**Length** [cm]	**Pre-stress** [N]
Top-Bottom Cables	5.976	242.336	5.976	241.661
Vertical Cables	11.081	712.345	11.136	636.889
Saddle Cables	3.662	447.030	5.976	483.310
Diagonal/ Reinforcing Cables	10.804	168.613	11.605	242.941
Struts	12.800	-1000.000	12.800	-1000.000

and Class-2.

The improvement in the stiffness properties of the tensegrity tower results from not only strut-to-strut contact but also the additional reinforcing cables. Even though the reinforcing cables are employed to make rotation and transition phases possible in this case, they also lock infinitesimal mechanisms and enhance stiffness properties in specific directions. The matrix analysis developed by Pellegrino and Calladine [31] indicates that the fully deployed SVD boom has one mechanism, $n_m = 1$, while the transformed Class-2 boom has none. Furthermore, in the case of longer booms with more than two stages, the number of mechanisms will be greater for Class-1 configurations.

Table 5.2: Deflection comparison of SVD and Class-2 booms

		Fully Deployed SVD	Transformed Class-2
Applied Load	**Loading Type**	**Tip Displacement** [mm]	**Tip Displacement** [mm]
F = 25 N	y Bending	0.110	0.058
	x Bending	0.110	0.058
F = 250 N	y Bending	7.345	1.218
	x Bending	8.767	1.291
F = 500 N	y Bending	12.634	2.941
	x Bending	14.860	3.129

The results given in Table 5.2 reveal the geometric nonlinearity that is present in tensegrity structures. Under the applied load of $F = 25$ N, none of the cables in either tensegrity system goes slack, and displacement values in different directions indicate symmetric behavior. On the other hand, when the applied load is increased to $F = 250$ N, some of the cables go slack and the displacements increase significantly. As the applied load reaches $F = 500$ N, the number of slack cables remains the same for the fully deployed SVD while it increases for the transformed Class-2. Therefore, the displacement values in the transformed Class-2 booms increase with an even greater rate. Additionally, regardless of the tensegrity boom type, since cable slackness occurs, the symmetric behavior disappear due to nonlinear behavior.

Initial and deflected geometries of the investigated tensegrity booms for loading cases of $F = 250$ N and $F = 500$ N are shown in Figures 5.39, 5.40, 5.41, 5.42, 5.43, 5.44, 5.45, 5.46, 5.47, and 5.48. For clarification, all cables are denoted with black lines while struts are represented with thick red lines. Under the applied load, some of the cables in the tensegrity systems became slack and their contribution to the stiffness of the whole structure was eliminated in the associated iteration. These cables are denoted with dashed black lines in the following figures.

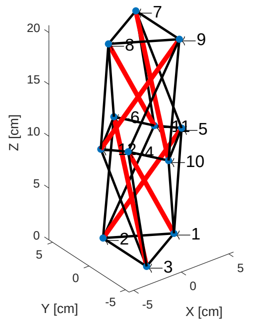

Figure 5.39: Fully Deployed SVD Initial Configuration

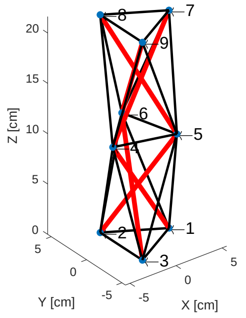

Figure 5.40: Transformed Class-2 Initial Configuration

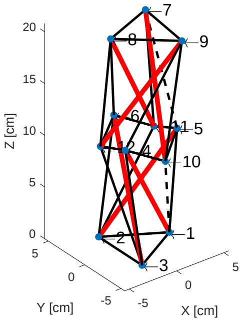

Figure 5.41: Fully Deployed SVD y Bending, 250 N

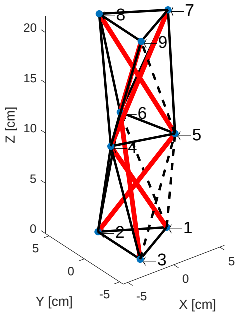

Figure 5.42: Transformed Class-2 y Bending, 250 N

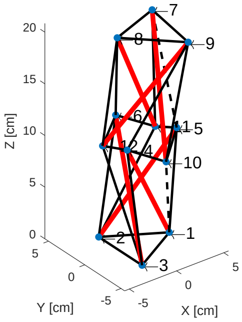

Figure 5.43: Fully Deployed SVD y Bending, 500 N

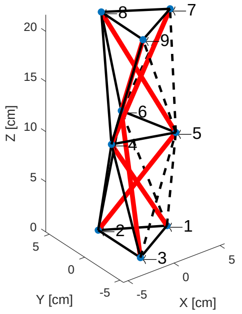

Figure 5.44: Transformed Class-2 y Bending, 500 N

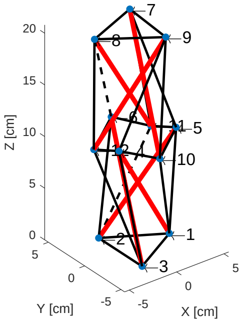

Figure 5.45: Fully Deployed SVD x Bending, 250 N

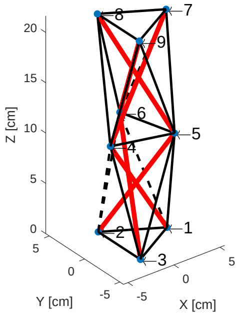

Figure 5.46: Transformed Class-2 x Bending, 250 N

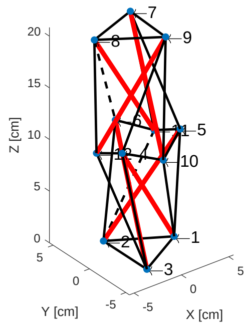

Figure 5.47: Fully Deployed SVD x Bending, 500 N

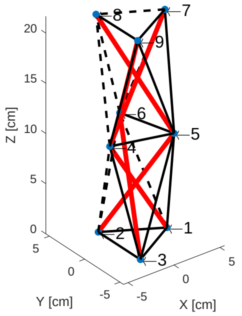

Figure 5.48: Transformed Class-2 x Bending, 500 N

In spite of having more slack cables than the fully deployed SVD boom, the transformed Class-2 boom is much stiffer. This behavior can be explained in terms of the number of mechanisms. Since no mechanisms exist in the transformed Class-2 boom, the structure does not soften as much as the fully deployed SVD boom. Additionally, examining the the values of the tip displacements reveals that the deployment strategy performed here is able to reduce the displacements in each loading case. Quantification of these reductions is tricky since each loading case gives a different ratio between tip displacements. Nevertheless, the stiffness improvement is undeniable, regardless of applied load levels.

Furthermore, the effective stiffness properties of these differently deployed tensegrity booms are evaluated as explained in Chapter 3, and the results are given in Table 5.3. The results indicate that the maximum improvement is attained in axial and torsional rigidities, which is mostly due to locking of infinitesimal mechanisms in these directions. Bending and shear rigidities in orthogonal directions are found to be the same, suggesting symmetry in the xy plane. These rigidities are also improved by 36% and 63%, respectively.

It is important to note that these effective stiffness properties are valid for the undeformed configurations. As the deformation occurs under applied loads, due to variation of the pre-stress in the members and potential cable slackness, these effective stiffness properties change, and the aforementioned symmetry disappears. Especially, cable slackness affects the stiffness properties significantly by softening the structure.

Table 5.3: Effective stiffness properties of the tensegrity booms

	Fully Deployed SVD	**Transformed Class-2**	**Percent Difference**
EA [N]	3.76×10^6	1.70×10^7	+352%
EI_x [N.cm^2]	3.21×10^7	4.38×10^7	+36%
EI_y [N.cm^2]	3.21×10^7	4.38×10^7	+36%
GA_x [N]	1.43×10^6	2.33×10^6	+63%
GA_y [N]	1.43×10^6	2.33×10^6	+63%
GJ [N.cm^2]	3.15×10^6	9.57×10^6	+204%

All the results are obtained for the example structures studied in this section, and greater improvement in stiffness properties may be obtained for structures made of different materials and with different sizing. In the next chapter, the optimization of tensegrity structures is studied in order to obtain maximum bending stiffness per mass per unit length. Additionally, the transformation path, which was selected arbitrarily in this case, is optimized considering stiffness.

Chapter 6

Optimization of Tensegrity Booms

Deployable booms for space applications need to be designed very carefully to meet the demands of the missions. The features sought in a deployable boom for space applications are typically lightweight, high stiffness and easy deployment. Tensegrity structures are shown to be lightweight and easy to deploy by many researchers [13, 14, 16, 60, 62]. Masic et al. [67] optimized tensegrity structures to obtain the maximum stiffness-to-mass ratio using nonlinear programming. The results indicate that the stiffness-to-mass ratio of tensegrity structures may be increased by three ways: increasing pre-stress, adding extra elements to lock mechanisms, and changing to a Class-2 structure. Inspired by these facts, a novel deployment strategy was presented in the previous chapter. Additionally, with proper selection of materials and geometry, stiffness of tensegrity structures can be increased even further.

Optimization of tensegrity structures was first studied by De Jager and Skelton [68] by studying the stiffness optimization problem of two dimensional tensegrity structures symbolically. Masic and Skelton [69] studied pre-stress selection for optimal LQR performance of tensegrity structures using a gradient method and attained a linear decrease in the objective function. Raja and Narayanan [70] employed a genetic algorithm for simultaneous optimization of structure and control of tensegrity structures. Genetic algorithm has also been used by Ali et al. [71] to obtain optimum design of a tensegrity footbridge satisfying static and dynamic requirements. Dalilsafaei et al. [72] investigated sizing and pre-stress optimization of tensegrity structures using a genetic algorithm and made a comparison between tensegrities and truss structures. Topology optimization of tensegrity structures has been investigated by Kanno [73, 74], Marzari [75], and more recently by Xu et al. [76]. There are also works devoted to energy optimization of deployable tensegrtiy structures by Li et al. [77] and zero energy shape modifications by Caluwaerts and Carbajal [78].

In this chapter, optimization of tensegrity structures is studied from different aspects. Considering that the deployed configuration of the tensegrity structure is defined as a Class-2, sizing and pre-stress optimization of tensegrity booms is achieved. The aim is selected to be maximizing the stiffness-to-mass ratio, and cross sectional areas of members and pre-stress level are determined. Therefore, the designed tensegrity boom can be compared to the state-of-the-art deployable booms, and its advantages and disadvantages can be concluded.

The optimization problem of tensegrity structures is a complex problem due to their nonlinear behavior. The static analyses of tensegrity structures under external loads are achieved through nonlinear finite element analyses and, therefore, employing traditional optimization techniques such as gradient methods is too computationally expensive. In order to solve optimization problems related to tensegrity structures, particle swarm optimization (PSO) is utilized. Particle swarm optimization is a stochastic optimization technique developed by Eberhart and Kennedy [79]. It is similar to genetic algorithm (GA) techniques, since it starts with a population in the search space and looks for the optimum solution by iteratively updating potential solutions based on the current best solutions. It does not require any gradient calculation and has proven to work robustly by many researchers in several applications [80–83]. A review paper by Poli [84] gives detailed information about applications of particle swarm optimization in different fields.

Furthermore, a deployment path that allows transformation between Class-1 and Class-2 tensegrity booms was discovered using parameters selected arbitrarily. Therefore, it is also possible to optimize the proposed deployment path by determining the arbitrarily selected parameters. In order to achieve the optimization of the deployment path, the final configuration obtained from sizing and pre-stress optimization of the deployed tensegrity boom is considered. Then potential paths that allow the transformation are determined, and their characteristics are investigated.

In this chapter, particle swarm optimization is explained, and an application to a structural problem is studied. Then, particle swarm optimization is applied to tensegrity booms for sizing and pre-stress optimization purposes. The obtained results are compared to the state of the art booms and discussed. Finally, using the final configuration of tensegrity booms determined by particle swarm optimization, the deployment path is optimized based on maximum stiffness properties.

6.1 Particle Swarm Optimization

Particle swarm optimization is a heuristic, global optimization tool developed by Eberhart and Kennedy [79] in 1995. It is a nature-inspired, population-based optimization technique, and the point of origin is similar to other swarm optimization techniques such as ant colony optimization [85] and artificial bee colony algorithm [86] in terms of mimicking the animal behavior. While trying to model the behavior of a bird flock searching for food, Eberhart and Kennedy ended up by developing a new optimization tool.

The algorithm randomly generates a population in the search space in which each individual is called a particle. Each particle is initially assigned a position and a velocity. For each particle, a fitness function, which is the quality measure of potential solutions, is evaluated based on the particle's position. Then, using simple mathematical expressions, each particle's position and velocity is updated with the knowledge of its best previous position and the best previous position in the swarm. The mathematical expressions for updating velocity and position of each particle are given as follows:

$$v_{i,j}^{k+1} = v_{i,j}^{k} + c_1 r_1 (xbest_{i,j}^{k} - x_{i,j}^{k}) + c_2 r_2 (xgbest_{j}^{k} - x_{i,j}^{k}) \tag{6.1}$$

$$x_{i,j}^{k+1} = x_{i,j}^{k} + v_{i,j}^{k+1} \tag{6.2}$$

where $x_{i,j}^{k}$ and $v_{i,j}^{k}$ are the i^{th} particle's position and velocity components in jth direction, respectively. k represents the iteration number while r_1 and r_2 are random numbers between $(0, 1)$. $xbest_i$ and $xgbest$ are the best positions obtained by the i^{th} particle and the whole population up to the k^{th} iteration.

The parameters c_1 and c_2 determine the velocity characteristics of particles and they were set to 2 initially by Eberhart and Kenneth. Higher values of c_1 make the particles go towards their best obtained positions while higher values of c_2 attract the particle to the best position obtained by the swarm.

Over the years, the fundamental PSO algorithm has been modified considering convergence and search efficiency. The most important modifications are considered to be maximum velocity, V_{max}, and inertia weight, w. Eberhart et al. [83] recommended the use of a maximum velocity so that the particles will not be able to leave the search space and diverge. It is also concluded by Shi and Eberhart [87] that the previous velocity of the particle can be multiplied with an inertia weight, and based on the selection, global or local minima can be sought. Eberhart and Shi [88] stated that by using a linearly decreasing inertia weight from 0.9 to 0.4, the performance of the algorithm is increased. Based on that, the modified updating rules are given as follows:

$$v_{i,j}^{k+1} = wv_{i,j}^{k} + c_1 r_1 (xbest_{i,j}^{k} - x_{i,j}^{k}) + c_2 r_2 (xgbest_{j}^{k} - x_{i,j}^{k}) \tag{6.3}$$

$$x_{i,j}^{k+1} = x_{i,j}^{k} + v_{i,j}^{k+1} \tag{6.4}$$

Based on Equations 6.3 and 6.4, movement of a particle in a two-dimensional search space can be depicted as in Figure 6.1. Red and blue nodes represent the global and local best positions. Black and green nodes indicate current and updated positions.

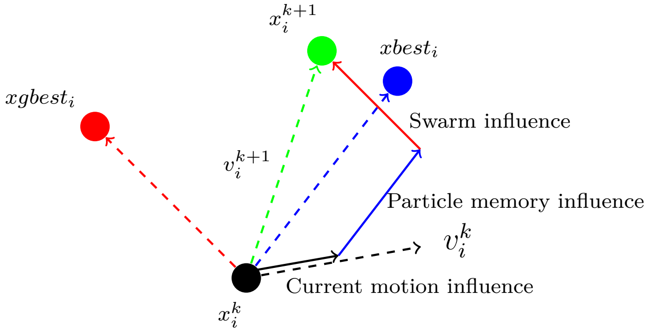

Figure 6.1: Movement of a particle in a two-dimensional search space

For constrained optimization problems, different approaches may be used with heuristic algorithms. The one taken in this dissertation is called the penalty approach. The penalty approach checks each constraint and, if any of them is violated, adds a relatively large number, called a penalty, to the fitness function value, making the solution worse compared to other potential solutions.

The algorithm of particle swarm optimization can be summarized as follows:

Algorithm

- **Initialization**
- Step 1: Initialize x_i, v_i
- Step 2: Evaluate fitness function for each particle
- Step 3: Determine $xbest_i$ for each particle and $xgbest$
- **Iteration**
- Step 4: Update velocity and position of each particle using Equations 6.3 and 6.4
- Step 5: Evaluate fitness function for each particle
- Step 6: Check if $f(x_i)$ is better than $f(xbest_i)$
  1. Yes, Update $xbest_i = x_i$
  2. No, Keep $xbest_i$
- Step 7: Check if any $f(x_i)$ is better than $f(xgbest)$
  1. Yes, Update $xgbest$ by assigning the best x_i
  2. No, Keep $xgbest$
- Step 8: Check if maximum number of iterations is reached
  1. Yes, Stop
  2. No, go to Step 4

Numerical Example

Particle swarm optimization is applied to a truss bridge design example studied by Hadidi et al. [89] using an artificial bee colony (ABC) algorithm in order to minimize the weight of the structure. The truss consists of 45 bars and is 2000 in. long. The geometry is predefined as in Figure 6.2, and sizing of the bars is studied. Nodes 1 and 20 are completely fixed, and vertical loads of 10 kips are applied at nodes 3, 5, 7, 9, 11, 13, 15, 17, and 19. The stress limit of the bars is given as ±30 ksi for all the bars. The displacements in the lateral and vertical directions are also limited to ±2 inches. The modulus of elasticity and the material density are given as 30,000 ksi and 0.283 lb/in^3. The structure is symmetric and the bars are divided into 23 groups, which are the design variables. Design variables also have a lower bound of 0.1 in^2.

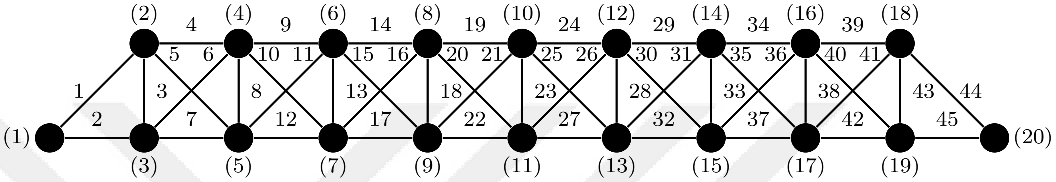

Figure 6.2: 45-bar truss bridge

A function was developed to conduct finite element analyses of the designed truss in order to determine displacements at each node and stress values in the bars. The main program calls the function to evaluate the fitness function for each potential solution. The population size was selected to be 300, and 10 different runs were performed, each consisting of 300 iterations. The optimal cross-sectional areas of the bars of each group and the weight of the overall structure are shown in Table 6.1. It also presents the results obtained from the PSO algorithm and the ones obtained from regular and modified artificial bee colony algorithms.

Table 6.1 proves the robustness of the particle swarm optimization algorithm. The minimized weight obtained by the particle swarm optimization algorithm is almost the same as the optimal solution obtained by ABC algorithms.

In the next section, particle swarm optimization is applied to tensegrity booms for sizing and pre-stress optimization in order to maximize bending stiffness per unit mass.

6.2 Sizing and Pre-stress Optimization of Deployed Tensegrity Booms

In order to design a tensegrity boom for space applications, particle swarm optimization is utilized in this section. Since bending stiffness of a deployable boom for space applications is stated to be one of the most important parameters [91], the

Table 6.1: Optimal cross sectional areas (in^2) for the truss design example

Design Variables	**Members**	**ABC** [89]	**MABC** [89]	**SOPT** [90]	**PSO**
G1	1, 44	5.4746	4.5996	4.6279	4.5850
G2	2, 45	4.5989	3.7966	3.6981	3.6963
G3	3, 43	4.1703	3.0497	3.202	3.1711
G4	4, 39	3.7872	3.2841	3.3323	3.2694
G5	5, 41	0.1000	0.1069	0.1003	0.1000
G6	6, 40	4.1735	3.9279	3.9324	3.9518
G7	7, 42	0.9497	0.9649	0.9287	0.9153
G8	8, 38	1.5902	1.2133	1.2041	1.1925
G9	9, 34	6.2656	7.6553	7.6821	7.7047
G10	10, 36	2.2039	2.1993	2.2417	2.3316
G11	11, 35	1.3925	1.1929	1.1930	1.1685
G12	12, 37	0.1000	0.1001	0.1004	0.1000
G13	13, 33	0.1000	0.1008	0.1000	0.1000
G14	14, 29	9.0689	9.5360	9.3600	9.4470
G15	15, 31	1.5310	1.2173	1.2055	1.2678
G16	16, 30	1.6245	1.4190	1.3068	1.3541
G17	17, 32	2.9146	2.5513	2.5968	2.5859
G18	18, 28	0.1000	0.1000	0.1001	0.1000
G19	19, 24	9.0685	11.5439	11.7376	11.5595
G20	20, 26	1.6352	1.2807	1.2362	1.2402
G21	21, 25	0.1000	0.1010	0.1000	0.1000
G22	22,27	4.4798	3.7598	3.7531	3.7386
G23	23	0.1000	0.1017	0.1020	0.1000
Weight (lb)		8267.21	7968.95	7968.59	7969.03

objective function is selected to be bending stiffness per unit mass. The aim is to design a tensegrity boom with high bending stiffness to mass ratio. The constraints are determined to be unilateral element behavior (no cable slackness), stress limits for cables, and strut buckling.

The cables are assumed to be made of Kevlar 49 resin impregnated strands since it provides a great tensile strength of $\sigma_Y = 3,600$ MPa. The modulus of elasticity of Kevlar 49 is given as $E = 124$ GPa, and the density is $\rho = 1440\ \text{kg/m}^3$. Unidirectional Mitsubishi K13C2U UHN /epoxy (60% fiber volume fraction) is chosen for struts due to its low density and high modulus of elasticity [72, 91]. The modulus of elasticity, Poisson's ratio, and the density are $E = 536$ GPa, $\nu = 0.39$, and $\rho = 1840$ kg/m^3.

The Canister Astromast [92] is selected as an example deployable boom for comparison. It is 14 meters long and has a radius of the cross-section of 0.254 m. Specific information about external loads acting on Cannister Astromast is not available to the public and it also depends on the mission. Garrett and Pike [93] note that typically, the amplitude of disturbance forces acting on a spacecraft due to operating equipment is between 0.001 and 10 N. Therefore, the following example loading case is considered: Lateral loads of 20 N in the x direction are applied at the nodes on the top plane, and the nodes on bottom plane are fixed.

The tensegrity boom is chosen to consist of three strut per stage since it has the least number of mechanisms (soft modes) [17]. The optimization problem is applied to the transformed Class-2 configuration since it is the final operational form of the structure. Struts are assumed to be hollow-tubes while cables have solid circular cross-sections. Then, the design variables are chosen as follows: the radii of different groups of cables; the inner and outer radii of struts; pre-stress coefficient; twist angle; and number of bays, for a total of nine design variables.

The unilateral element behavior constraint is treated by ensuring that cables and struts are always in tension and compression, respectively. The stress limit constraint for cables is considered by

$$\sigma_{c_i} \leq \sigma_Y \tag{6.5}$$

where σ_{c_i} is the axial stress value in the i^{th} cable. For the strut buckling constraint, both global (Euler buckling) and local (wall) buckling cases are considered. The global buckling of individual struts can be represented as

$$T_{st,i} \leq P_{eu} \tag{6.6}$$

where $T_{st,i}$ is the compression force in the i^{th} strut and P_{eu} is the Euler buckling load for a simply supported - simply supported column:

$$P_{eu} = \frac{\pi^2 EI}{L^2} \tag{6.7}$$

The local buckling constraint for thin-walled tubular columns can be written as

$$\sigma_{st,i} \leq \sigma_{cr} \tag{6.8}$$

where $\sigma_{st,i}$ is the axial stress value in the i^{th} strut. σ_{cr} is the critical stress for wall buckling [94]:

$$\sigma_{cr} = \frac{\gamma E}{\sqrt{3(1-\nu^2)}} \frac{r_o - r_i}{r_o} \tag{6.9}$$

where γ is a correlation coefficient as follows:

$$\gamma = 1 - 0.901(1 - e^{-\phi}) \tag{6.10}$$

$$\phi = \frac{1}{16}\sqrt{\frac{r_o}{r_o - r_i}} \tag{6.11}$$

where r_o and r_i are the outer and inner radii, respectively.

Then, the main MATLAB program calls a function that carries out nonlinear finite element analyses under applied external loads and evaluates the effective stiffness properties of the boom. The lower and upper bounds for radii of cables, inner and outer radii of struts, and the pre-stress coefficient are selected as 2 and 10 mm, 1 and 30 mm, and, 0.1 and 20 N/mm, respectively. Bounds of the twist angle are determined to be 62° and 88° since struts collide at 60° and vertical cables are slack at 90°. For the constrained optimization problem, a penalty approach is employed for constraint handling as explained in the previous section. The optimization problem can be stated as follows:

$$\begin{aligned} \underset{X}{\text{minimize}} \quad & -EI(X)/M(X) \\ \text{subject to} \quad & -\mathbf{q}(i) < 0, \ \text{for cable} \\ & \sigma_{c,i} \le \sigma_Y, \ \text{for cable} \\ & \mathbf{q}(i) < 0, \ \text{for strut} \\ & T_{st} \le P_{eu}, \ \text{for strut} \\ & \sigma_{st} \le \sigma_{cr}, \ \text{for strut} \end{aligned} \tag{6.12}$$

Initial results reveal that the maximum bending stiffness is obtained with the smallest number of bays that requires longer struts. However, longer struts mean wider volume for the undeployed configuration to account for strut lengths. Considering the available space during launch, an increased number of bays seems to be more convenient. Therefore, in order to get a better understanding of how the number of bays affects the bending stiffness of the structure, optimization analyses are conducted for fixed numbers of bays.

Fixing the number of bays reduces the design variables by one, and optimization analyses are conducted with number of bays between 2 and 50. The population size is selected as 200, and three analyses with 100 iterations are conducted for each case. Figures 6.3, 6.4, 6.5, 6.6, 6.7, and 6.8 show the variations of bending stiffness, bending stiffness per unit mass, torsional stiffness, torsional stiffness per unit mass, mass, and tip deflection, respectively. The results are also shown in Table 6.2.

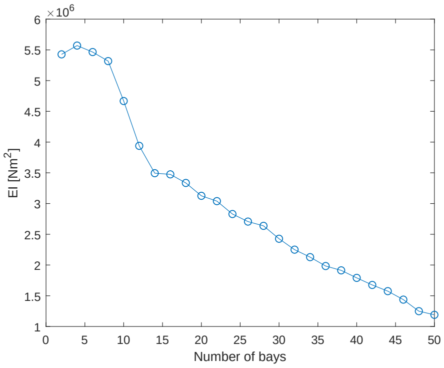

Figure 6.3: Variation of bending stiffness

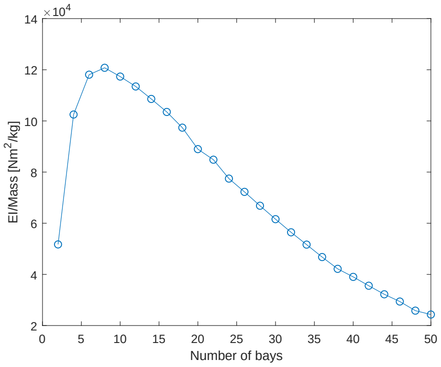

Figure 6.4: Variation of bending stiffness per unit mass

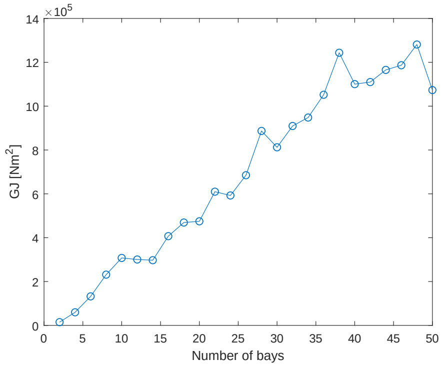

Figure 6.5: Variation of torsional stiffness

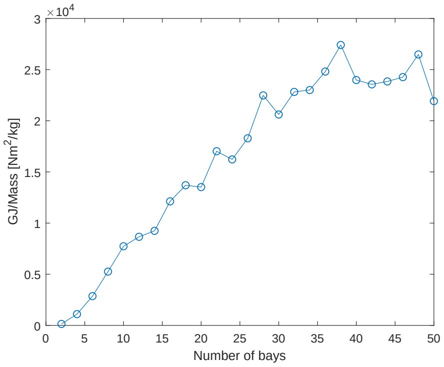

Figure 6.6: Variation of torsional stiffness per unit mass

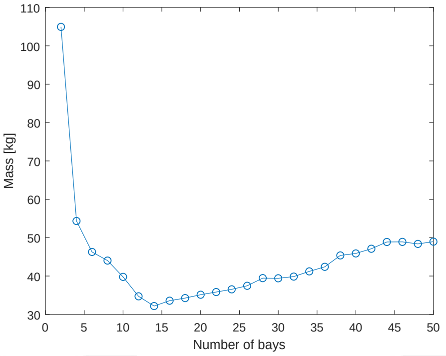

Figure 6.7: Variation of mass

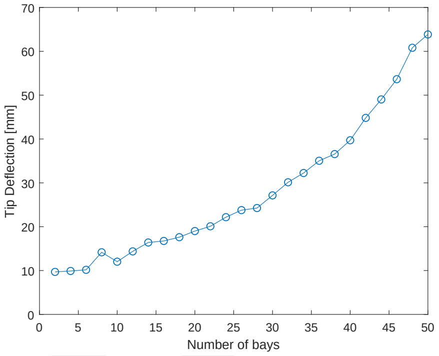

Figure 6.8: Variation of tip deflection

Additionally, decreases in lengths of struts with increasing number of bays is shown in Figure 6.9. The results indicate that strut lengths decrease substantially with increased number of bays for small number of bays; however, this decrease slows down for greater numbers of bays while the decrease in bending stiffness per unit mass is linear. Therefore, the number of bays should be selected carefully based on the requirements of the mission. One might compromise the bending stiffness for the torsional stiffness, which can be accomplished by increasing the number of bays with a slight increase in the mass.

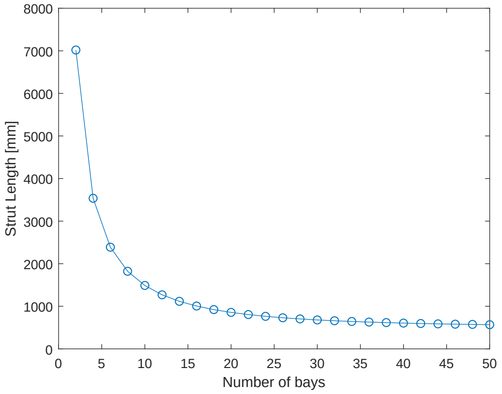

Figure 6.9: Variation of length of struts

Table 6.2: Bending and torsional stiffnesses of optimized booms

Number of bays	Number of struts	EI [Nm^2]	GJ [Nm^2]	Mass [kg]	EI/Mass	GJ/Mass
2	6	5.43×10^{6}	1.48×10^{4}	104.938	5.17×10^{4}	1.41×10^{2}
4	12	5.57×10^{6}	5.97×10^{4}	54.340	1.03×10^{5}	1.10×10^{3}
6	18	5.44×10^{6}	1.32×10^{5}	46.076	1.18×10^{5}	2.86×10^{3}
8	24	5.32×10^{6}	2.31×10^{5}	44.026	1.21×10^{5}	5.26×10^{3}
10	30	4.67×10^{6}	3.08×10^{5}	39.779	1.17×10^{5}	7.73×10^{3}
12	36	3.94×10^{6}	3.01×10^{5}	34.710	1.13×10^{5}	8.86×10^{3}
14	42	3.49×10^{6}	2.97×10^{5}	32.175	1.09×10^{5}	9.24×10^{3}
16	48	3.47×10^{6}	4.07×10^{5}	33.572	1.04×10^{5}	1.21×10^{4}
18	54	3.34×10^{6}	4.69×10^{5}	34.251	9.74×10^{4}	1.37×10^{4}
20	60	3.13×10^{6}	4.75×10^{5}	35.129	8.90×10^{4}	1.35×10^{4}
22	66	3.04×10^{6}	6.10×10^{5}	35.826	8.48×10^{4}	1.70×10^{4}
24	72	2.83×10^{6}	5.93×10^{5}	36.532	7.75×10^{4}	1.62×10^{4}
26	78	2.71×10^{6}	6.85×10^{5}	37.455	7.23×10^{4}	1.83×10^{4}
28	84	2.64×10^{6}	8.87×10^{5}	39.453	6.68×10^{4}	2.25×10^{4}
30	90	2.43×10^{6}	8.12×10^{5}	39.412	6.16×10^{4}	2.06×10^{4}
32	96	2.25×10^{6}	9.09×10^{5}	39.854	5.65×10^{4}	2.28×10^{4}
34	102	2.13×10^{6}	9.48×10^{5}	41.211	5.16×10^{4}	2.30×10^{4}
36	108	1.98×10^{6}	1.05×10^{6}	42.401	4.68×10^{4}	2.48×10^{4}
38	114	1.91×10^{6}	1.24×10^{6}	45.371	4.22×10^{4}	2.74×10^{4}
40	120	1.79×10^{6}	1.10×10^{6}	45.888	3.90×10^{4}	2.40×10^{4}
42	126	1.68×10^{6}	1.11×10^{6}	47.112	3.56×10^{4}	2.36×10^{4}
44	132	1.58×10^{6}	1.17×10^{6}	48.878	3.22×10^{4}	2.38×10^{4}
46	138	1.44×10^{6}	1.19×10^{6}	48.901	2.94×10^{4}	2.43×10^{4}
48	144	1.25×10^{6}	1.28×10^{6}	48.374	2.58×10^{4}	2.65×10^{4}
50	150	1.19×10^{6}	1.07×10^{6}	48.962	2.43×10^{4}	2.19×10^{4}

The optimization results reveal that the maximum bending stiffness per unit mass is obtained when the number of bays is 8. Furthermore, bending stiffness and bending stiffness per unit mass decrease as the number of bays increases, as shown in Figures 6.3 and 6.4. This is mostly due to the increased number of ball joints for the connection of struts. Design variables of each optimized case are also given in Table 6.3.

Table 6.3: Optimized design variables for tensegrity booms

Number of bays	Radius of top and bottom cables [mm]	Radius of vertical cables [mm]	Radius of saddle cables [mm]	Radius of reinforcing cables [mm]	Outer radius of struts [mm]	Inner radius of struts [mm]	Pre-stress Coefficient [N/mm]	Twist Angle [degree]
2	2.000	9.616	7.249	10.000	30.000	24.914	0.122	62.000
4	3.498	10.000	3.697	10.000	30.000	28.903	0.295	62.000
6	4.543	10.000	4.221	10.000	30.000	29.510	0.461	62.000
8	5.605	9.999	4.726	10.000	30.000	29.714	0.624	62.000
10	6.166	8.934	4.844	10.000	30.000	29.783	0.892	69.829
12	6.266	7.188	4.406	10.000	30.000	29.774	1.592	80.875
14	6.593	6.114	4.265	10.000	30.000	29.783	2.310	84.317
16	7.874	6.481	4.636	9.986	30.000	29.815	2.710	84.281
18	7.967	6.354	4.880	10.000	30.000	29.806	3.724	85.639
20	8.009	5.868	4.934	9.999	30.000	29.724	6.756	87.680
22	9.259	6.272	5.133	10.000	30.000	29.811	5.505	86.527
24	9.721	5.799	5.019	10.000	30.000	29.740	8.986	87.943
26	10.000	5.965	5.124	10.000	30.000	29.765	9.274	87.785
28	10.000	6.545	5.779	10.000	30.000	29.846	6.709	86.237
30	10.000	6.016	5.565	10.000	30.000	29.792	10.184	87.641
32	10.000	6.160	5.561	10.000	30.000	29.831	8.933	86.991
34	10.000	6.134	5.710	10.000	30.000	29.820	10.346	87.266
36	10.000	6.301	5.866	10.000	30.000	29.847	9.302	86.648
38	10.000	6.227	6.273	10.000	30.000	29.762	15.585	88.000
40	9.999	6.273	6.106	10.000	30.000	29.804	13.454	87.458
42	10.000	6.231	5.809	9.996	30.000	29.756	17.726	87.998
44	10.000	6.323	5.795	10.000	30.000	29.740	19.683	88.000
46	10.000	6.289	5.932	10.000	30.000	29.790	16.375	87.559
48	9.947	6.372	6.123	9.849	30.000	29.860	10.978	85.960
50	10.000	5.910	6.163	9.445	30.000	29.761	19.983	87.877

Furthermore, the stowed configuration of deployable tensegrity booms is another concern. The initial, undeployed configuration of a tensegrity boom in a self-stress state is quite wide and not really practicable. Therefore, a stowing approach for optimization purposes is proposed here. The struts can be packed into a cylinder, positioned vertically. Since they are hollow-tubes, the cables can be placed inside the struts and other volume that remain empty inside the cylinder. The package areas can be minimized by employing optimum packaging solutions of circles in a larger circle. Based on the number of struts, the solutions to optimum packaging problem are provided by many researchers [95–100]. Then, for the proposed stowing approach, required volumes are calculated for each case, and the results are given in Table 6.4.

In Table 6.4, the radius ratio represents the ratio between the outer radii of struts and the radius of the cylinder. These numbers are optimum values for the given number of struts and were obtained from several studies [95–100]. The results reveal that package radius, area, and volume all increase with the increasing number of struts.

Starting from a stowed configuration, the tensegrity boom can be put into its initial, undeployed configuration using some sort of mechanism. The tensegrity boom can be attached to a moving base plate, which can be used to bring the boom out of the circular package or canister, and cables can be tightened to apply self-stress. Then, the deployment can be achieved by cable actuation as described in the previous chapters.

The next section deals with the optimization of the deployment/transformation path. The transformation example studied in the previous chapter was achieved with arbitrarily selected parameters which are feasible for the problem. The selection of these parameters is studied in the next section to optimize the deployment/transformation path.

6.3 Optimization of Deployment/Transformation Path

The optimization of deployment/transformation path can be achieved by different means based on the requirements. The aforementioned deployment strategy that involves a transformation from Class-1 to Class-2 consists of five phases. Out of these five phases, three can be stated as autonomous or predefined, which means

Table 6.4: Packaging properties of optimized booms

Number of struts	Radius Ratio	Strut Length [mm]	Strut Radius [mm]	Package Radius [mm]	Package Area [mm^2]	Package Volume [mm^3]
6	0.33333	7018.40	30	9.00×10^{1}	2.54×10^{4}	1.79×10^{8}
12	0.24816	3536.70	30	1.21×10^{2}	4.59×10^{4}	1.62×10^{8}
18	0.20560	2388.00	30	1.46×10^{2}	6.69×10^{4}	1.60×10^{8}
24	0.17694	1822.20	30	1.70×10^{2}	9.03×10^{4}	1.65×10^{8}
30	0.16135	1488.70	30	1.86×10^{2}	1.09×10^{5}	1.62×10^{8}
36	0.14822	1269.10	30	2.02×10^{2}	1.29×10^{5}	1.63×10^{8}
42	0.13611	1116.50	30	2.20×10^{2}	1.53×10^{5}	1.70×10^{8}
48	0.12835	1006.10	30	2.34×10^{2}	1.72×10^{5}	1.73×10^{8}
54	0.12189	922.12	30	2.46×10^{2}	1.90×10^{5}	1.75×10^{8}
60	0.11566	856.33	30	2.59×10^{2}	2.11×10^{5}	1.81×10^{8}
66	0.10994	805.88	30	2.73×10^{2}	2.34×10^{5}	1.89×10^{8}
72	0.10555	763.74	30	2.84×10^{2}	2.54×10^{5}	1.94×10^{8}
78	0.10144	730.16	30	2.96×10^{2}	2.75×10^{5}	2.01×10^{8}
84	0.09853	703.40	30	3.04×10^{2}	2.91×10^{5}	2.05×10^{8}
90	0.09482	679.05	30	3.16×10^{2}	3.14×10^{5}	2.14×10^{8}
96	0.09188	659.86	30	3.26×10^{2}	3.35×10^{5}	2.21×10^{8}
102	0.08931	642.87	30	3.36×10^{2}	3.54×10^{5}	2.28×10^{8}
108	0.08677	628.96	30	3.46×10^{2}	3.75×10^{5}	2.36×10^{8}
114	0.08478	616.85	30	3.54×10^{2}	3.93×10^{5}	2.43×10^{8}
120	0.08275	605.00	30	3.63×10^{2}	4.13×10^{5}	2.50×10^{8}
126	0.08053	595.04	30	3.73×10^{2}	4.36×10^{5}	2.59×10^{8}
132	0.07882	586.69	30	3.81×10^{2}	4.55×10^{5}	2.67×10^{8}
138	0.07714	579.70	30	3.89×10^{2}	4.75×10^{5}	2.75×10^{8}
144	0.07548	574.56	30	3.97×10^{2}	4.96×10^{5}	2.85×10^{8}
150	0.07429	567.00	30	4.04×10^{2}	5.12×10^{5}	2.90×10^{8}

no arbitrary selection of parameters. The phases that can be optimized are the initial deployment phase and the rotation phase. Activation of reinforcing cables, transformation, and the final deployment phases are predetermined even though they are affected by the other two phases. In this dissertation, the deployment/-transformation path is optimized to maximize bending stiffness during deployment, considering any possible dynamic disturbances.

The initial deployment phase is governed by the equilibrium surface, and feasible pairs of azimuth and declination angles generate a self-equilibrated tensegrity structure. On this equilibrium surface, the points that allow a transformation without experiencing a slack cable can be determined. After determination of these points on the equilibrium surface, effective stiffness properties can be evaluated, and the final point of the initial deployment that provides the maximum bending stiffness can be selected, accomplishing the first step of deployment/transformation path optimization.

After the initial deployment is achieved, the reinforcing cables can be activated, and the rotation phase can be started. Since the final configuration of the transformed Class-2 is optimized, the twist angle is known. Therefore, the rotation phase ends when the optimized twist angle is achieved, completing the optimization of the deployment/transformation path.

As the rotation phase is completed, the transformation from Class-1 to Class-2 takes place. Finally, the transformed Class-2 tensegrity boom can be deployed even further until the boom has a uniform cross-section.

Azimuth and declination angle pairs that allow a transformation from Class-1 to Class-2 can be determined by running several deployment simulations. For each point on the equilibrium surface, deployment simulations can be conducted, and the force finding method can be applied in order to track force-densities. If any of the cables carry compression during deployment, the simulations stop and mark the point as infeasible. Furthermore, during the rotation, total height of the structure may decrease. If, as a result of this decrease, any nodes other than the bottom ones fall below the bottom plane, the corresponding point on the equilibrium surface is also marked as infeasible. All of the remaining pairs are *candidate* feasible points, allowing a transformation from Class-1 to Class-2.

A selection can be made based on the effective stiffness properties to determine the optimum initial deployment path, assuming linear variation of azimuth and declination angles. However, deployment simulations need to be conducted with these remaining candidate points, and careful visual inspection is required to detect any cable entanglements or element collisions. Any of these problems makes the deployment unrealistic. Therefore, starting from the candidate point that yields the maximum bending stiffness, deployment simulations are conducted, unrealistic cases are determined, and these points are eliminated. From the final feasible set of points, the one which possesses the maximum minimum bending stiffness along the deployment path is selected.

For demonstration purposes, the case from the sizing optimization example in which the package diameter and height are almost equal to each other is selected. In this way, the shape of the package resembles a cube, which may be useful while placing it into the launch vehicle. The selected case is a tensegrity boom with 32 bays and the length of struts is 659.86 mm with a package diameter of 653 mm. The equilibrium surfaces with respect to overlap and height are shown in Figures 6.10 and 6.11.

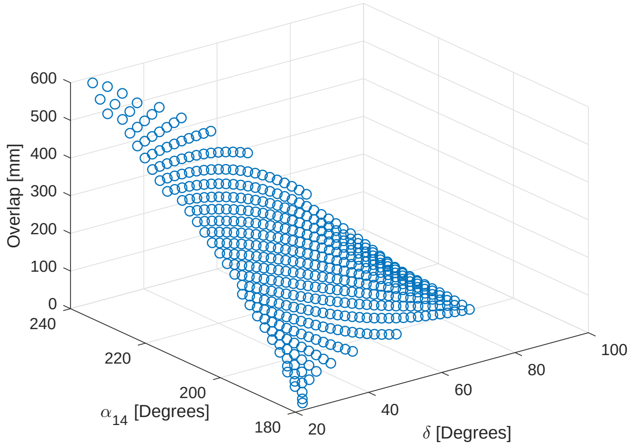

Figure 6.10: Equilibrium surface with respect to overlap

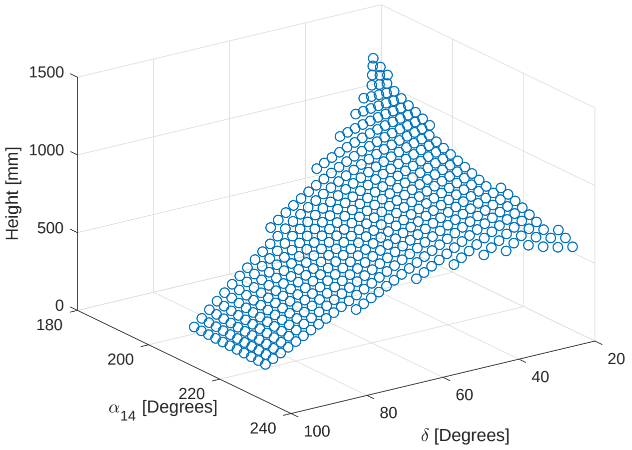

Figure 6.11: Equilibrium surface with respect to height

Then, after several deployment simulations, the candidate feasible pairs of azimuth and declination angles are identified. These pairs are shown in Figures 6.12 and 6.13 with filled green circles.

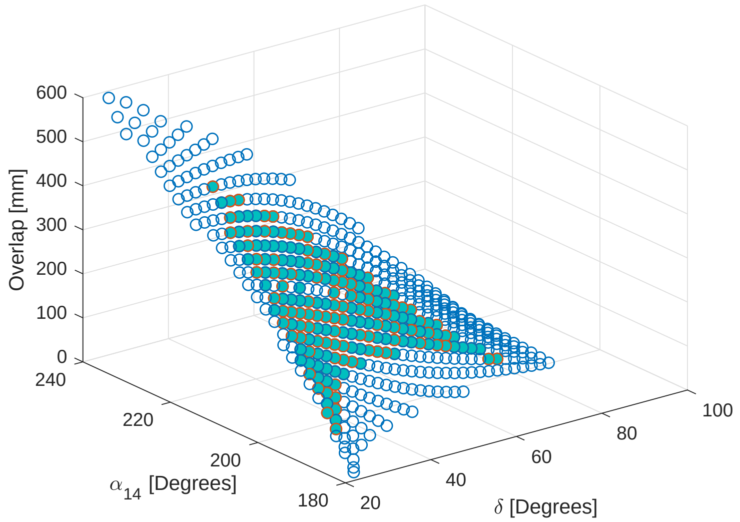

Figure 6.12: Feasible points on equilibrium surface with respect to overlap

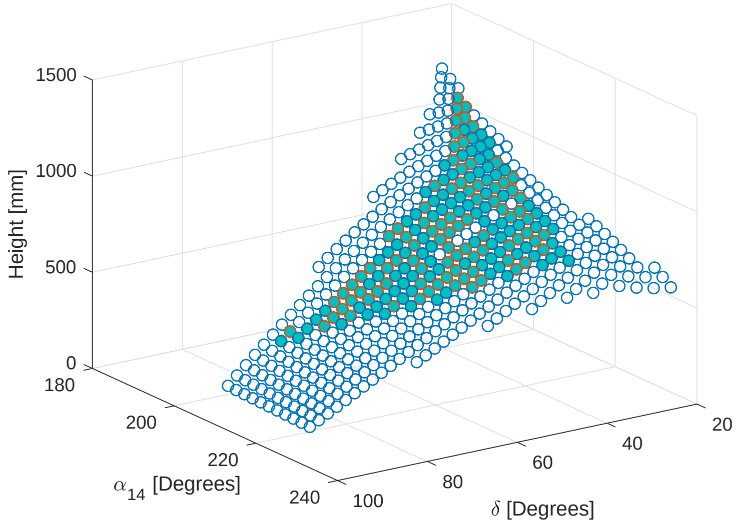

Figure 6.13: Feasible points on equilibrium surface with respect to height

After the feasible points are determined for the transformation, effective stiffness properties are evaluated on the equilibrium surface. The equilibrium surfaces with respect to axial, bending, shear, and torsional rigidities are shown in Figures 6.14, 6.15, 6.16, and 6.17, respectively.

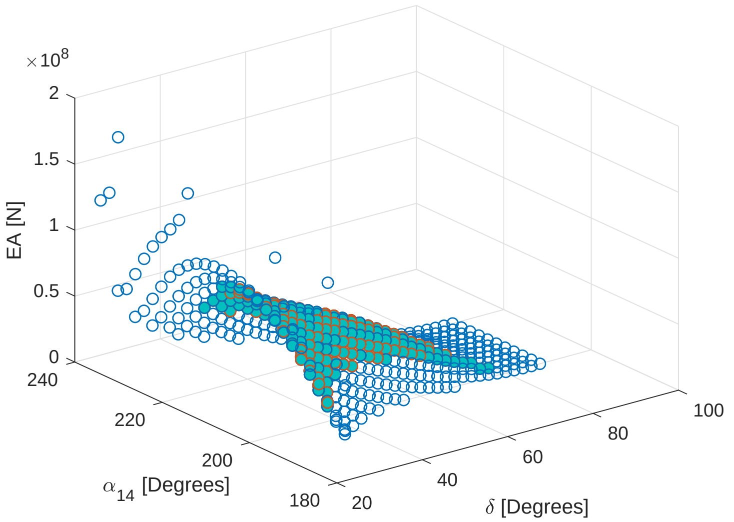

Figure 6.14: Equilibrium surface with respect to axial rigidity

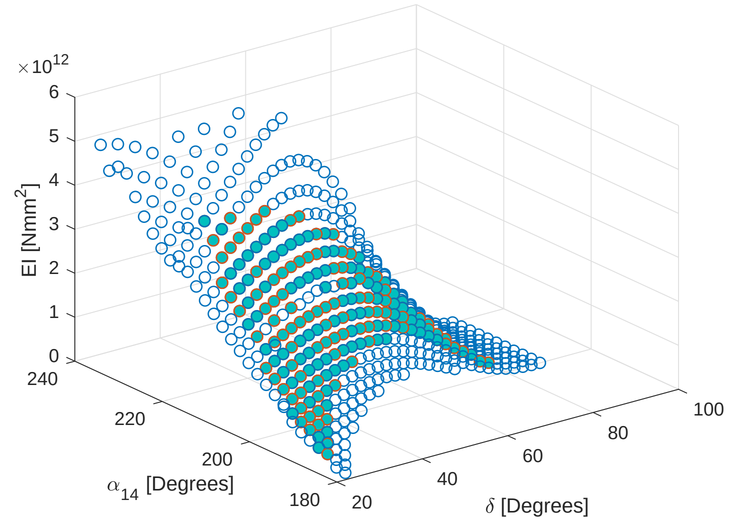

Figure 6.15: Equilibrium surface with respect to bending rigidity

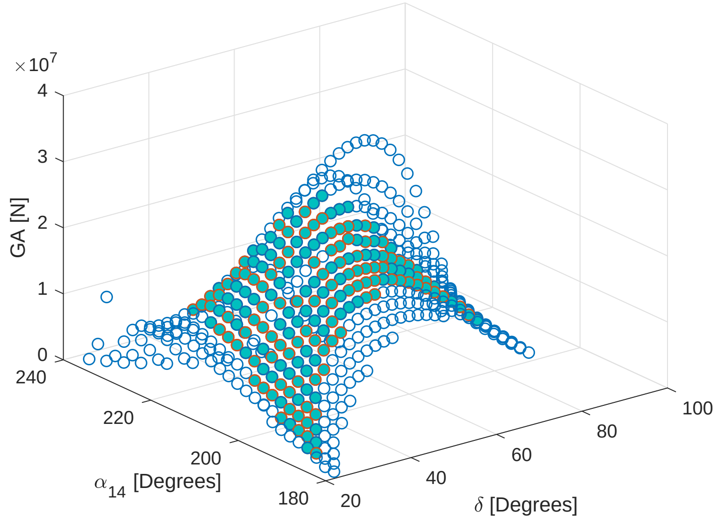

Figure 6.16: Equilibrium surface with respect to shear rigidity

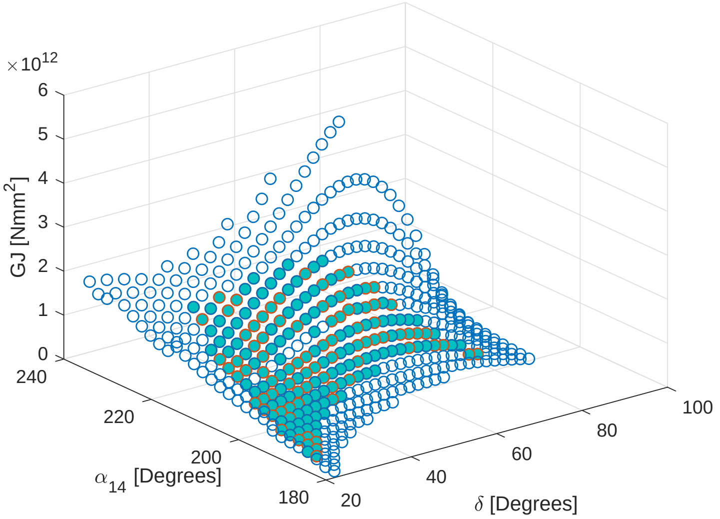

Figure 6.17: Equilibrium surface with respect to torsional rigidity

Figure 6.14 shows that the axial rigidity has some sort of symmetry around $\alpha_{14} = 210°$. It increases with decreasing declination angle, δ. Figure 6.15 reveals that the bending rigidity is superior for higher azimuth angle, α_{14}. Figure 6.16 indicates that the shear rigidity is maximum when the azimuth angle is high and the declination angle is moderate, and it decreases as declination angle decreases.

Figure 6.17 reveals that the torsional rigidity shows a similar behavior to bending rigidity. It is greater for higher azimuth angles, α_{14}.

From Figure 6.15, the azimuth and declination angles pair that yields the maximum bending rigidity is identified as $\alpha_{14} = 220°$ and $\delta = 44°$. However, after simulating the deployment with this pair, during deployment, cable entanglements occur, making this point infeasible. After running several deployment simulations, the feasible point which yields the maximum bending rigidity is found as $\alpha_{14} = 214°$ and $\delta = 56°$.

On the other hand, From Figure 6.11, the initial point is determined to be $\alpha_{14} = 218°$ and $\delta = 88°$, since it provides a very compact height. Then, assuming a linear variation between these start and end points, the deployment is achieved. Figure 6.18 illustrates the optimized deployment path for the initial deployment. Figures 6.19, 6.20, 6.21, and 6.22 show the optimized initial deployment sequence.

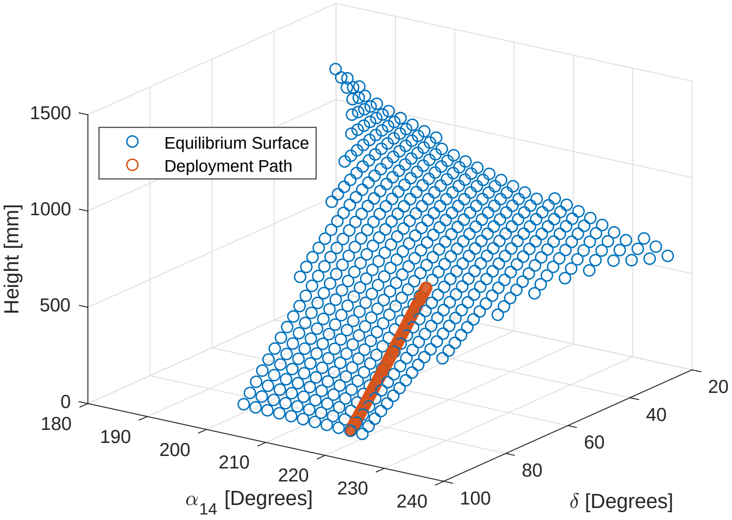

Figure 6.18: Optimized deployment path

Variation of the lengths of the elements and the force-densities are shown in Figures 6.23 and 6.24. The results show that unilateral element behavior is preserved. The saddle and diagonal cables are shortened, and the vertical cables are lengthened while the top and bottom cables, and struts maintain their lengths.

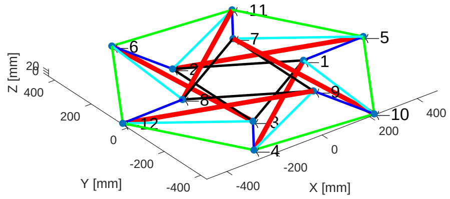

Figure 6.19: Initial deployment, 1/4

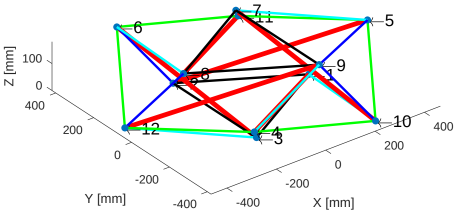

Figure 6.20: Initial deployment, 2/4

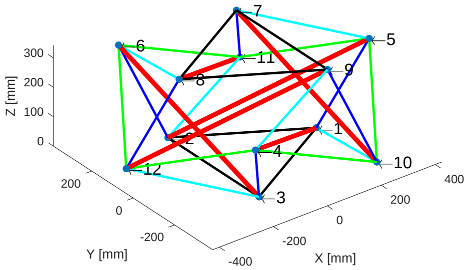

Figure 6.21: Initial deployment, 3/4

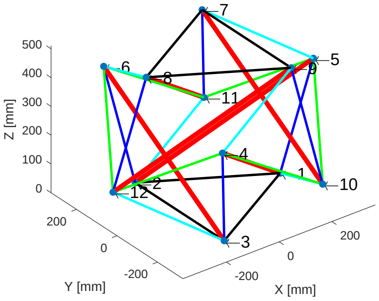

Figure 6.22: Initial deployment, 4/4

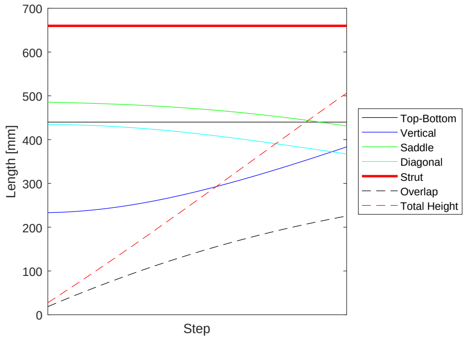

Figure 6.23: Variation of the lengths

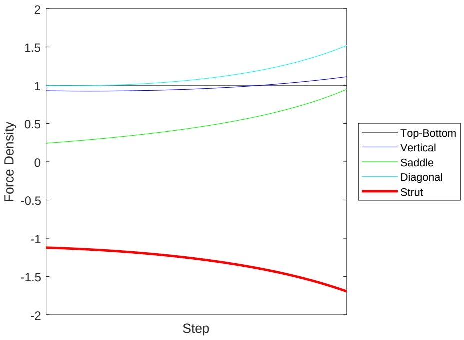

Figure 6.24: Variation of the force-densities

After the initial deployment is achieved, reinforcing cables (in orange) are activated in order to suppress dependence on the equilibrium surface. Activation of the reinforcing cables is shown in Figure 6.25.

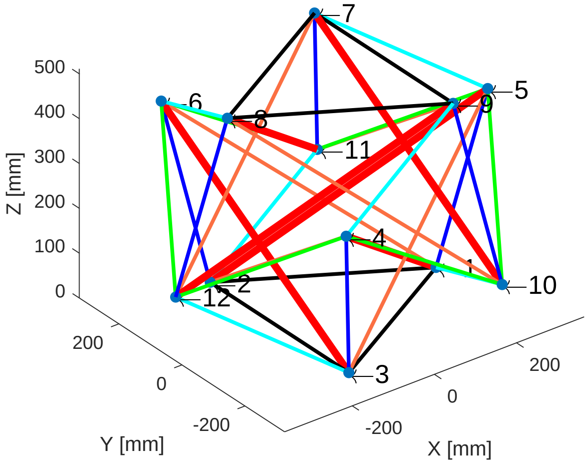

Figure 6.25: Activation of reinforcing cables

Then, the rotation phase starts, and continues until the twist angle α reaches 87.9°, which is obtained from the sizing and pre-stress optimization problem. The rotation phase is illustrated in Figures 6.26, 6.27, 6.28, and 6.29.

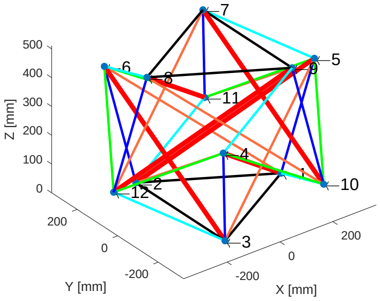

Figure 6.26: Rotation Phase, 1/4

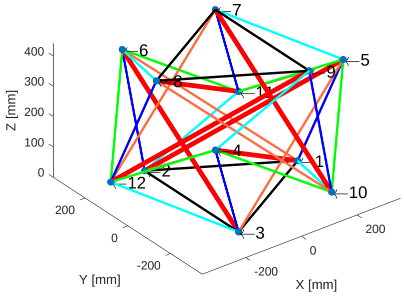

Figure 6.27: Rotation Phase, 2/4

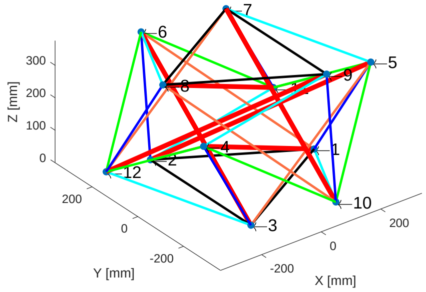

Figure 6.28: Rotation Phase, 3/4

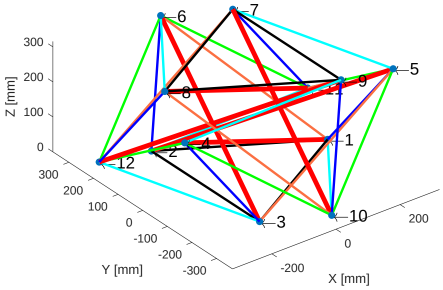

Figure 6.29: Rotation Phase, 4/4

Similarly, the variation of the lengths of the members and the force-densities are shown in Figures 6.30 and 6.31.

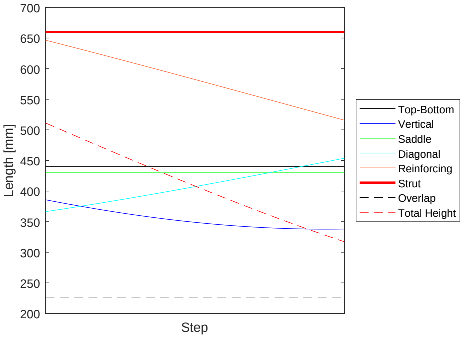

Figure 6.30: Variation of the lengths

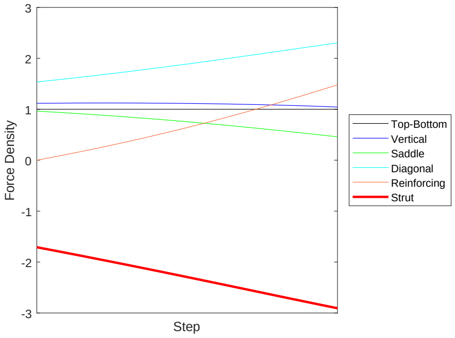

Figure 6.31: Variation of the force-densities

When the rotation sequence is completed, transformation from Class-1 to Class-2 begins. Nodes 10, 11, and 12 approach nodes 4, 5, and 6, respectively. As a result, three saddle cables are shortened to zero length, allowing a strut-to-strut contact at the nodes. The transformation sequence is shown in Figures 6.32, 6.33, 6.34, and 6.35.

During the transformation phase, as noted before, some of the elements in different stages act differently, and symmetry is partially lost. The variation of the lengths of the members and the force-densities are shown in Figures 6.36 and 6.37, respectively.

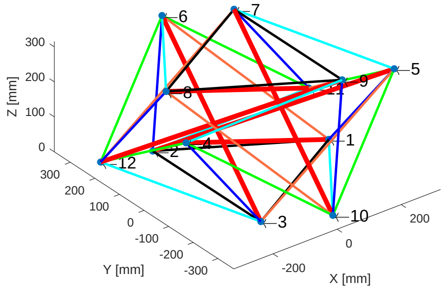

Figure 6.32: Transformation Phase, 1/4

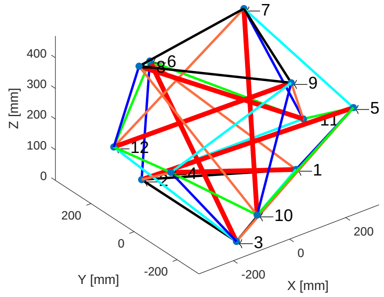

Figure 6.33: Transformation Phase, 2/4

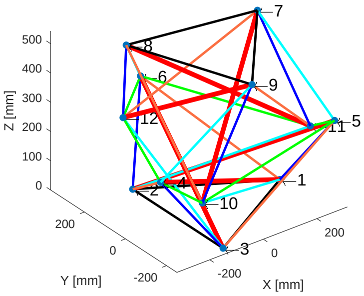

Figure 6.34: Transformation Phase, 3/4

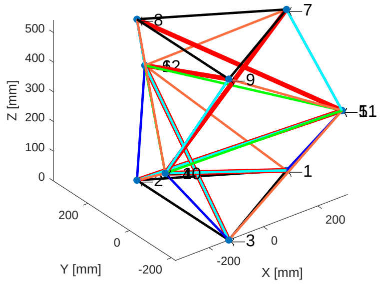

Figure 6.35: Transformation Phase, 4/4

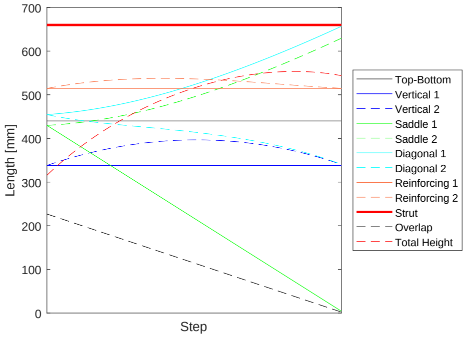

Figure 6.36: Variation of the lengths

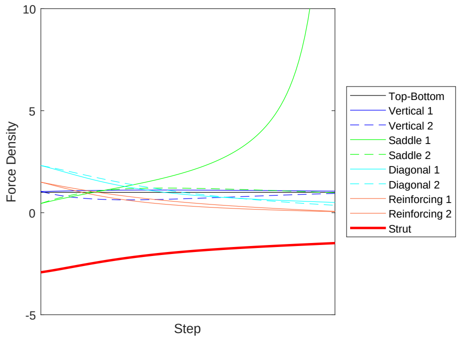

Figure 6.37: Variation of the force-densities

Figure 6.36 shows that diagonal cables overlap with the vertical cables in the top stage and struts in bottom stage. Therefore, they may be slackened just before the transformation phase is completed. Vertical and reinforcing cables also act differently in the transformation phase; however, at the end of the transformation phase, symmetry becomes clear again. Additionally, Figure 6.37 indicates that force-densities in one group of saddle cables increase substantially. However, this is due to the fact that they are shortened to zero length. Careful investigation shows that the forces in these cables are of the same order of magnitude of the forces in other cables.

As the struts touch each other, they are locked, and the tensegrity boom becomes a Class-2 configuration as shown in Figure 6.38.

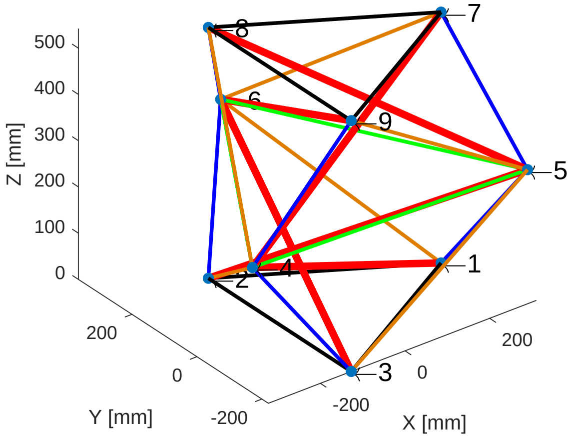

Figure 6.38: Transformed Class-2 tensegrity boom

Then, final deployment is executed until the uniform cross-section of the tensegrity boom is satisfied. The final deployment sequence is shown in Figures 6.39, 6.40, 6.41, and 6.42.

The variation of the lengths of the elements and the force-densities are shown in Figures 6.43 and 6.44, respectively.

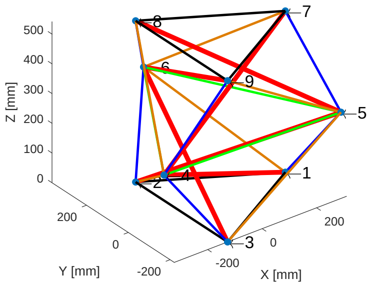

Figure 6.39: Final Deployment, 1/4

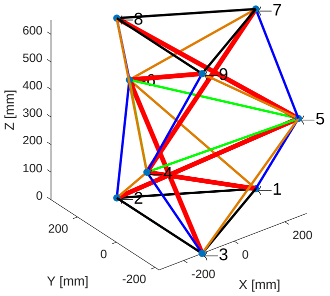

Figure 6.40: Final Deployment, 2/4

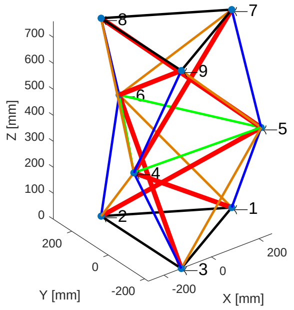

Figure 6.41: Final Deployment, 3/4

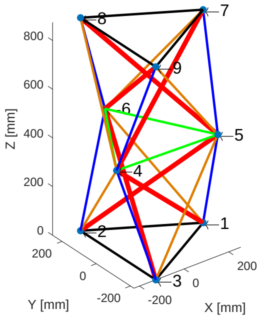

Figure 6.42: Final Deployment, 4/4

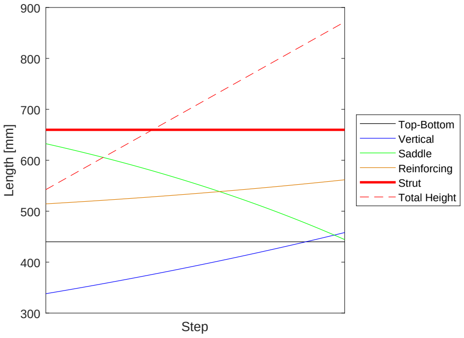

Figure 6.43: Variation of the lengths

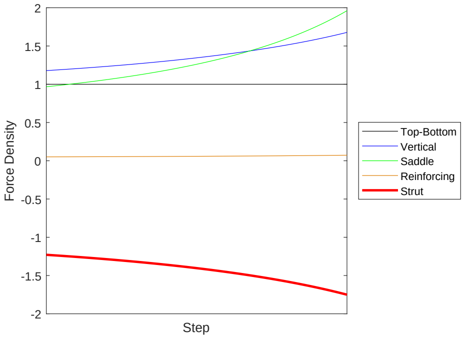

Figure 6.44: Variation of the force-densities

The same deployment strategy can be achieved in the remaining 30 bays, either sequentially or simultaneously. As a result, the final configuration of the structure is 14 m long with a radius of cross-section of 254 mm. It has a bending rigidity of

2.25×10^6 Nm^2 and a torsional rigidity of 9.09×10^5 Nm^2.

The maximum lengths of the cables are tracked during deployment, and the total mass of the designed boom is calculated. Additionally, starting with the pre-stress coefficient obtained from sizing and pre-stress optimization, the maximum forces in each type of element is also obtained and, based on that information, cross-sectional areas of diagonal cables are determined, considering stress limits for cables. The maximum lengths of the elements, their contribution to the total mass, and the maximum force, and stress they encounter during deployment are given in Table 6.5.

Table 6.5: Maximum length, force, stress and total mass data

Element Type	Total Number	Maximum Length [mm]	Mass [kg]	Maximum Force [N]	Maximum Stress [MPa]
Top and Bottom Cables	6	439.94	1.194	3.93×10^3	12.51
Vertical Cables	96	459.58	7.574	6.93×10^3	58.13
Saddle Cables	93	646.50	8.410	7.83×10^3	80.61
Diagonal Cables	96	659.86	*	9.39×10^3	*
Reinforcing Cables	96	632.59	27.473	6.89×10^3	21.93
Struts	96	659.86	3.698	-1.72×10^4	-542.09

The maximum force experienced by the struts is found to be -1.72×10^4 N during the transformation phase, creating a stress value greater than the critical stress associated with local buckling. In order to avoid that, the overall pre-stress levels can be reduced during transformation in order to prevent any failure.

Since the cross-sectional areas of the diagonal cables are not determined by the sizing and pre-stress optimization problem, in Table 6.5, their contribution to the total mass and the maximum stress are denoted with *.

The results show that the mass of the structure, excluding the diagonal cables which are not considered in the final configuration, is 48.350 kg, which is different than the one obtained from sizing and pre-stress optimization. Sizing and pre-stress optimization does not take into account the length changes during deployment, and the total mass of the structure is calculated as 39.854 kg by considering only the lengths of members in the final configuration.

In order to determine the cross-sectional areas of the diagonal cables and their contribution to the total mass of the structure, the tensile strength of the cables is taken into account. The tensile strength of the material which the cables are made of is 3,600 MPa. The stress limit can hardly be exceeded with very low cross-sectional area values and, therefore, the radius of the diagonal cables is selected as the lower limit of design variables, 2 mm, which results in 186.8 MPa. Then, its contribution to the total mass of the structure is calculated as 1.146 kg, summing to 49.496 kg.

The bending stiffness to mass ratio of the designed tensegrity boom is found to be 4.55×10^4 Nm^2/kg, which is 36 times greater than the Canister Astromast's. In order to observe how the designed tensegrity boom compares with the state of the art deployable boom concepts (whose data are provided by Murphey [91]), comparison of bending stiffness to mass per unit length ratio is made. The results are shown in Table 6.6.

Table 6.6: Comparsion of different deployable boom concepts

Deployable Boom	**EI** [Nm^2]	**w** [kg/m]	**EI/w** [Nm^3/kg]	**R** [m]	**EI/w/R^2** [Nm/kg]
S-2 Coilable	1.00×10^5	0.42	2.38×10^5	0.68	5.15×10^5
ATK-ABLE GR1	8.14×10^4	0.07	1.16×10^6	0.197	3.00×10^7
ATK-ABLE GR2	1.12×10^4	0.032	3.49×10^5	0.12	2.43×10^7
Ultra Boom 1	1.17×10^4	0.1445	8.12×10^4	0.09	1.00×10^7
Ultra Boom 2	6.51×10^3	0.0655	9.93×10^4	0.09	1.23×10^7
FMI Isogrid	5.84×10^3	0.023	2.54×10^5	0.159	1.00×10^7
FMI Slit Tape Truss	3.67×10^4	0.0577	6.63×10^5	0.2	1.59×10^7
AFRL DECSMAR	9.20×10^4	0.157	5.86×10^5	0.1476	2.69×10^7
ATK-COI TriLok	1.20×10^6	0.14	8.59×10^6	0.5	3.43×10^7
L'Garde SSP Truss	1.54×10^6	0.7	2.19×10^6	0.68	4.76×10^6
Canister Astromast	2.10×10^4	1.2	1.75×10^4	0.254	2.71×10^5
Transformed Tensegrity n=32	2.25×10^6	3.5354	6.36×10^5	0.254	9.86×10^6
Transformed Tensegrity n=8	5.32×10^6	3.3752	1.58×10^6	0.254	2.44×10^7
ATK-ABLE SRTM	1.58×10^7	5.232	3.02×10^6	0.56	9.63×10^6
Transformed Tensegrity n=6	2.54×10^7	3.9443	6.44×10^6	0.56	2.05×10^7

The table shows that the designed tensegrity boom performs well by comparison to state of the art deployable boom concepts. Greater bending stiffness-to-mass ratio value can be obtained when the number of bays is selected as 8. Optimizing the deployment path and considering the diagonal cables and maximum lengths of elements, bending stiffness to mass per unit length ratio is shown in Table 6.6. The optimization of the deployment path results are also given in Appendix A. However, the radii of the selected deployable booms have a direct influence on the bending rigidity values [91]. Therefore, in order to make a fair comparison, for each of the given deployable boom concepts' dimensions, pre-stress and sizing optimization, and optimization of deployment path should be repeated for tensegrity booms. For example, the radius of ATK-ABLE SRTM from Table 6.6 is 0.560 m, which is more than double the radius of the tensegrity boom considered. In order to approximate the influence of the radii of the deployable booms on bending stiffness, $EI/w/R^2$ parameter is also evaluated for the booms.

Furthermore, Table 6.6 includes information for different deployable boom categories mentioned in Chapter 1. All of these deployable boom concepts excel for different reasons in specific applications. Tensegrity structures fall into the category of articulated booms and, therefore, their stiffness is found to be greater compared to the other ones given in Table 6.6 except ATK-ABLE SRTM.

The ATK-ABLE SRTM boom is selected as the second example, and its radius is used to optimize a 20-meter long tensegrity boom. The sizing and pre-stress optimization and the optimization of the deployment path are repeated, and the results are provided in Appendix B. The results show that maximum bending stiffness-to-mass per unit length ratio is obtained with 6 bays. The results in Table 6.6 show that the transformed tensegrity boom with 6 bays has a bending stiffness-to-mass per unit length ratio more than 2 times greater than ATK-ABLE SRTM's.

In summary, a novel multi-stage deployment strategy is proposed for cylindrical tensegrity booms. The structure starts in Class-1 configuration and, as the deployment occurs, the configuration is transformed into a Class-2 one, increasing stiffness. Sizing and pre-stress optimization is conducted for a predefined connectivity using a Particle Swarm Optimization algorithm, and the effect of the number of bays on several parameters is investigated. Finally, the deployment path is optimized to maximize bending stiffness during deployment.

Chapter 7
Conclusions and Future Work

In this dissertation, deployable booms for space applications were reviewed briefly in four different categories. Their deployment techniques, advantages, and disadvantages were explained. A relatively new structural concept, called tensegrity, is introduced, and its unique features were presented. The applications in aerospace engineering field were discussed with a focus given to deployable tensegrity boom designs for space missions.

Tensegrity structures are pre-stressed and pin-jointed and are in self-equilibrium with no external forces or constraints applied. They consist solely of axial load-carrying members, cables, and struts. For large deployable space structures, tensegrity structures offer the potential of high packaging efficiency and good structural performance. These deployable, stiff tensegrity structures could be excellent candidates for space structures where high stiffness-to-mass ratio and ease of deployment are important.

The mechanics of tensegrity structures were addressed in detail, starting with the derivation of equilibrium equations. Necessary rank conditions for generating a self-equilibrated tensegrity structure were described, and static and kinematic indeterminacies were explained with Maxwell's rule. One of the most important steps in the mechanics of tensegrity structures, the form-finding problem, was addressed, and recent solution techniques were investigated. Another method called force finding, in which force densities in each element of the structure are determined with given connectivity and nodal coordinates, was described.

Static and dynamic analyses of tensegrity structures were investigated next. Geometric nonlinearity in tensegrity structures due to pre-stress was explained, and its stiffening effect on the behavior of tensegrity structures was discussed. A nonlinear finite element model was described to account for geometric nonlinearity, and an incremental iterative solution method was employed in order to take any possible slack cables into account. The solution method was explained in detail, and a numerical example of a tensegrity unit under external loads was investigated. The results indicate that tensegrity structures respond differently to applied forces in opposite directions, which is called “anisotropic” behavior. Using the finite element model, the free vibration problem was studied, and natural frequencies were obtained. For kinematically indeterminate tensegrity structures, natural frequencies of vibration modes associated with infinitesimal mechanisms are found to be very low compared to those of other vibration modes. Additionally, the results reveal that corresponding natural frequencies increase proportionally with the square root of the pre-stress levels. Furthermore, long tensegrity booms were modeled as a three-dimensional beam, and their effective stiffness properties were calculated. For this purpose, the energy equivalency method was described, and a modified version was developed to reduce the complexity in its implementation. Nonlinear finite element analyses were also used for validation purposes, and their application procedure was explained. Excellent agreement in axial and torsional rigidities are obtained while bending and shear rigidities are good.

Then, deployment actuation methods of tensegrity structures, namely cable-mode and strut-mode deployment, were discussed, and their advantages and disadvantages were described. Cable-mode deployment was investigated further, and two deployable tensegrity booms with three struts in each stage, Class-1 SVD tensegrity boom and Class-2 tensegrity boom, were examined with their deployment mechanisms. The deployment simulations were carried out, and the aforementioned force-finding method was utilized to track force-densities in the elements to check unilateral element behavior (cables carry tension and struts carry compression). Generalization procedures were devised for deployment of n-strut Class-1 and Class-2 tensegrity booms.

In order to improve stiffness of tensegrity booms, an attempt was taken which aims not only to design structurally efficient tensegrity booms for space applications but also to deploy them. Exploiting the resemblance between Class-1 and Class-2 tensegrity booms, a deployment/transformation path has been discovered. The transformation from Class-1 to Class-2 tensegrity booms promises increased stiffness due to strut-to-strut contact and additional reinforcing cables. An example was studied, and the results were provided, showing increased stiffness. Additionally, since the initial tensegrity configuration is a Class-1, high packaging density is not discarded. The resulting structure becomes an adaptive tensegrity boom that exhibits high packaging density and high stiffness when deployed.

Finally, particle swarm optimization was employed to optimize the bending stiffness-to-mass ratio of tensegrity booms. A 14-meter long tensegrity boom was designed and optimized to obtain maximum stiffness-to-mass ratio. The design variables were selected as cross-sectional areas of individual groups of elements, prestress coefficient, and twist angle between two modules. The results show that the transformed tensegrity booms can easily compete with the state of the art deployable booms in terms of stiffness-to-mass ratio. Additionally, the transformation path was also optimized in order to maximize bending stiffness during the deployment and transformation.

Overall, the proposed transformation from Class-1 to Class-2 tensegrity configurations promises significant improvements in the structural efficiency of deployable tensegrity booms. This deployment strategy has the potential to increase the claims on tensegrity structures to be one of the best candidates for deployable structures. Alongside parallel advances in cable actuation and development of a locking mechanism, tensegrity structures can replace the conventional deployable structures in real space missions.

7.1 Future Work

In this dissertation, it was shown that stiffness-to-mass ratio of tensegrity structures can be better than those of conventional deployable booms. Nevertheless, there are some questions that need to be answered. These questions can be addressed in two different groups.

Performance Related

In order to design structurally more efficient tensegrity booms specialized for a space mission, design variables and their lower and upper bounds can be selected more meticulously. Furthermore, fairer comparison between tensegrity booms and conventional deployable boom concepts should be achievable by conducting sizing and pre-stress optimization for each boom's geometry. The radius of a boom has a direct effect on its bending stiffness and, therefore, in general, comparing different booms which have different radii is not quite correct.

One of the constraints selected for sizing and pre-stress optimization is unilateral element behavior to avoid any cable slackness. However, cable slackness may be allowed for sizing optimization to see its influence on the bending stiffness-to-mass ratio.

On the other hand, packaging efficiency may require some improvements so that tensegrity booms can be stowed more compactly into smaller volumes. Since the deployment mode is selected as cable actuation, initial configurations of tensegrity booms require wide volumes, which may not be provided by the launch vehicle. Therefore, a combination of cable-mode and strut-mode deployment may be considered.

Implementation Related

In order to achieve transformation perfectly, a locking mechanism is required to lock the struts while serving as a ball joint when struts touch each other at nodes. Rather complex designs will be required if the transformation is planned with more than three struts per stage in order to host several elements at nodes.

Another concern is the active control of the cables for reconfiguration and deployment. Advances in cable actuation techniques may be required to achieve thorough control over the structure. Work should be devoted to optimal placement of small motors on the structure to alleviate possible difficulties and increase control performance. In order to reduce the number of actuators found in the structure, some of the cables can be clustered in such a way that they run through more than two nodes. Since symmetric deployment is employed, the total number of actuators may be reduced with a well-designed control strategy. Other potential challenges of implementation of tensegrity booms on a satellite may arise due to coupling with attitude control systems and, therefore, more comprehensive designs may be required, considering vibration characteristics during deployment.

Tape spring hinges can also be introduced to struts to fold them, reducing the stowed volume. The best way to stow and deploy tensegrity booms seems to be starting with a "pile of sticks and strings" and, with the help of additional mechanisms putting them into self-equilibrated configuration, sequentially deploying and transforming them. However, this idea is complex, and additional advances and designs are needed.

Appendix A

Optimization of Deployment Path for 8 bays, R=0.254 m

In this Appendix, the optimization of deployment path results for the tensegrity boom with 8 bays are given. The length of struts is 1822.2 mm, and the equilibrium surfaces with respect to overlap and height are shown in Figures A.1 and A.2, respectively.

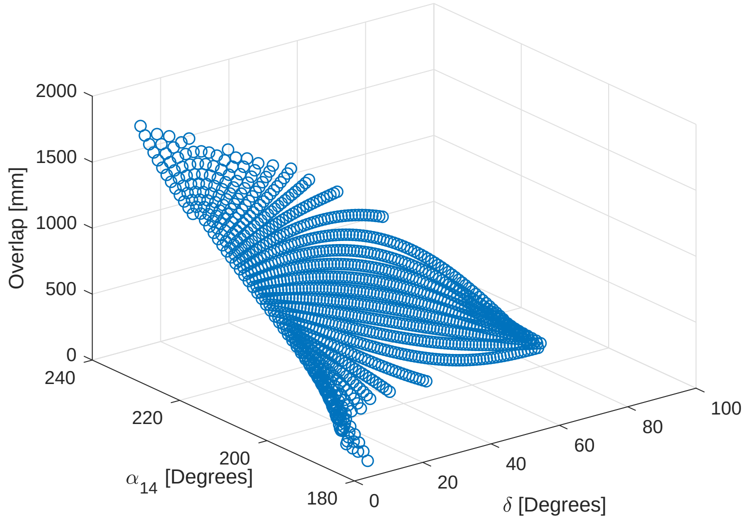

Figure A.1: Equilibrium surface with respect to overlap

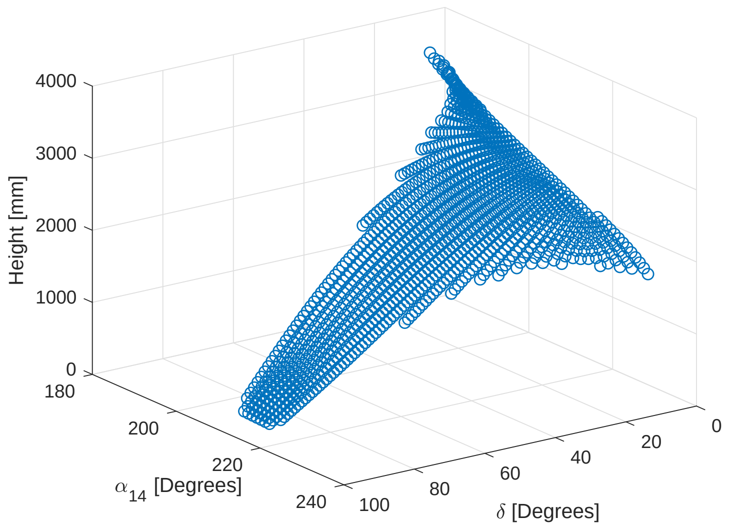

Figure A.2: Equilibrium surface with respect to height

Then, after several deployment simulations, the candidate feasible pairs of azimuth and declination angles are identified. These pairs are shown in Figures A.3 and A.4 with filled green circles.

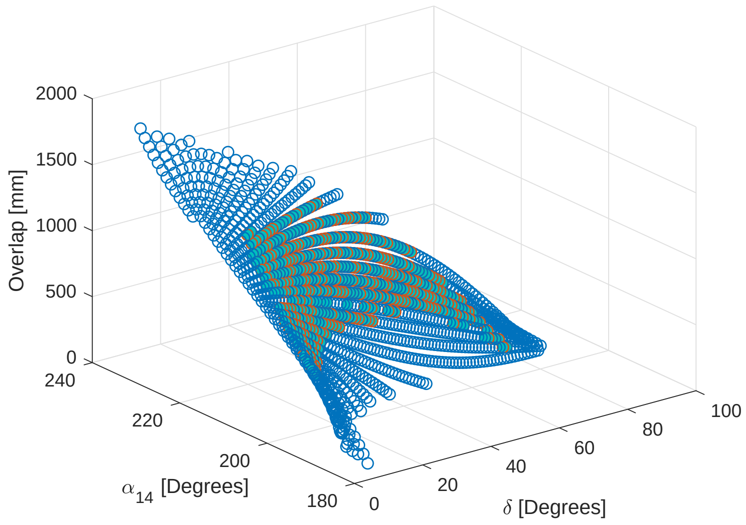

Figure A.3: Feasible points on equilibrium surface with respect to overlap

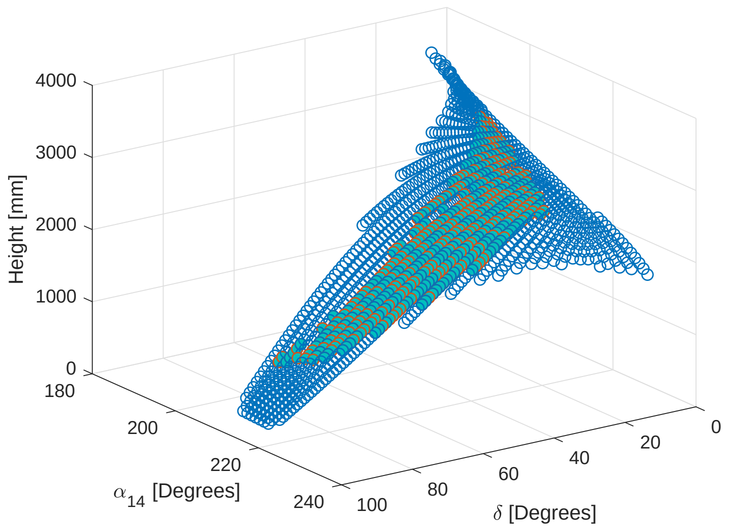

Figure A.4: Feasible points on equilibrium surface with respect to height

After the feasible points are determined for the transformation, effective stiffness properties are evaluated on the equilibrium surface. The equilibrium surfaces with respect to axial, bending, shear, and torsional rigidities are shown in Figures A.5, A.6, A.7, and A.8, respectively.

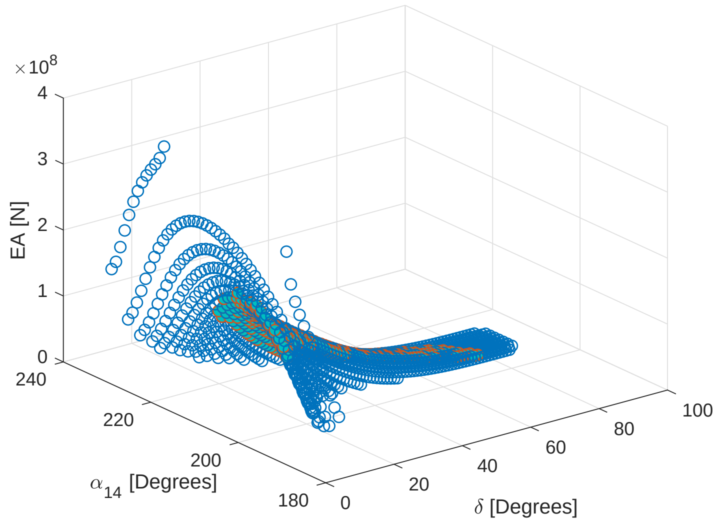

Figure A.5: Equilibrium surface with respect to axial rigidity

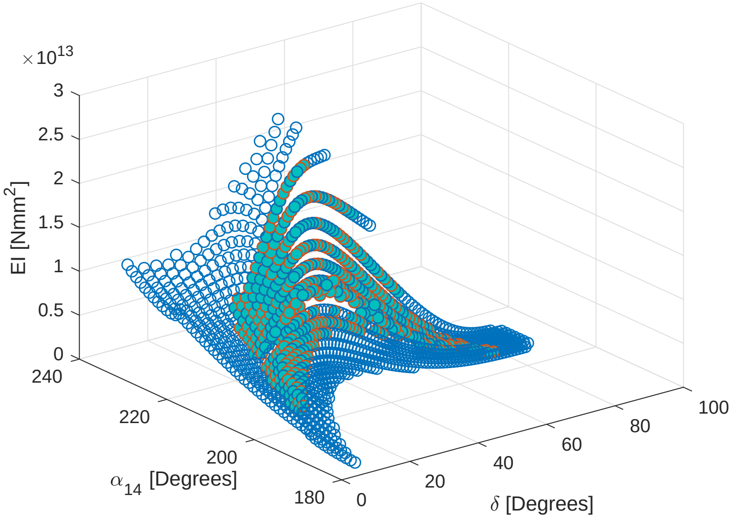

Figure A.6: Equilibrium surface with respect to bending rigidity

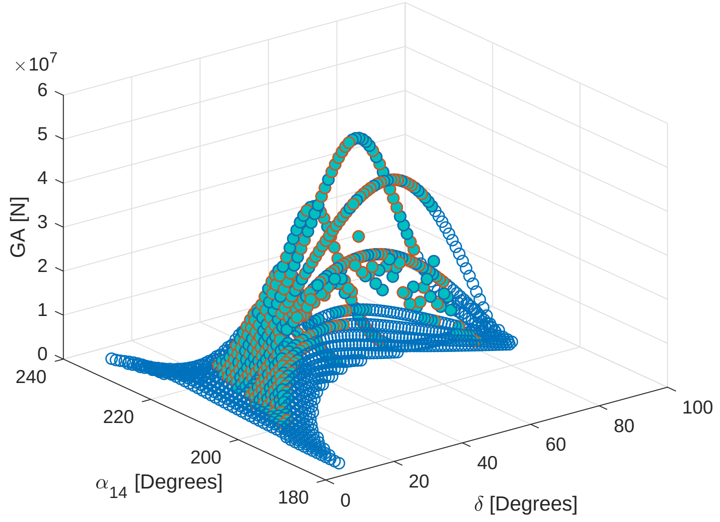

Figure A.7: Equilibrium surface with respect to shear rigidity

From Figure A.6, the point that yields the maximum bending stiffness without any element collision is identified as $\alpha_{14} = 216°$ and $\delta = 35°$. This point is used to optimize the initial deployment step, and the twist angle, $\alpha = 62°$ obtained from sizing and pre-stress optimization is used to optimize the rotation of the intermediate plane step.

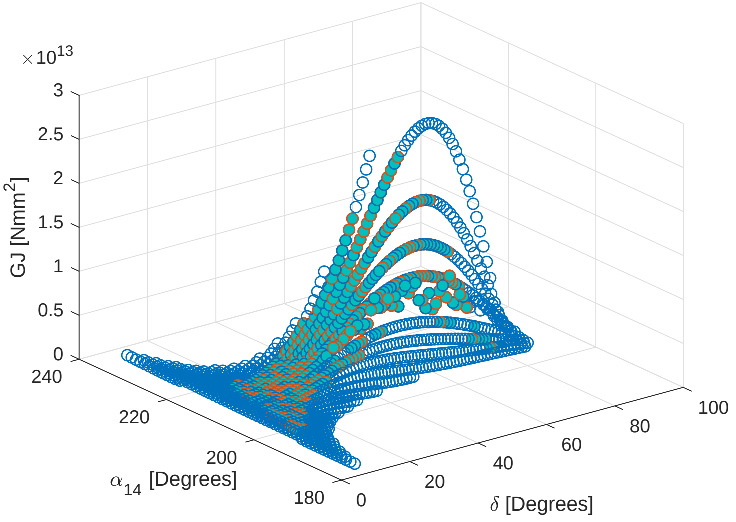

Figure A.8: Equilibrium surface with respect to torsional rigidity

The maximum lengths of the cables are tracked during deployment, and the total mass of the designed boom is calculated. Additionally, starting with the pre-stress coefficient obtained from sizing and pre-stress optimization, the maximum forces in each type of element is also obtained and, based on that information, cross-sectional areas of diagonal cables are determined, considering stress limits for cables. The maximum lengths of the elements, their contribution to the total mass, and the maximum force, and stress they encounter during deployment are given in Table A.1.

Table A.1: Maximum length, force, stress and total mass data

Element Type	Total Number	Maximum Length [mm]	Mass [kg]	Maximum Force [N]	Maximum Stress [MPa]
Top and Bottom Cables	6	439.94	0.375	2.74×10^2	2.78
Vertical Cables	24	1767.20	19.187	1.17×10^3	3.72
Saddle Cables	21	1574.90	3.341	5.49×10^2	7.83
Diagonal Cables	24	1822.20	*	1.84×10^2	*
Reinforcing Cables	24	1772.00	19.239	1.04×10^3	3.30
Struts	24	1822.20	4.319	-2.27×10^3	-42.37

The results show that the mass of the structure, excluding the diagonal cables which are not considered in the final configuration, is 46.462 kg. The minimum possible cross-sectional areas of diagonal cables that yield a stress value lower than the stress limit are selected, their mass contribution is calculated, and the total mass of the structure is obtained as 47.253 kg.

Then bending stiffness-to-mass ratio of the designed tensegrity boom and bending stiffness-to-mass per unit length ratio are found to be 1.13×10^{5} $\mathrm{Nm^{2}/kg}$ and 1.58×10^{6} $\mathrm{Nm^{3}/kg}$, respectively.

Appendix B

Optimization Results, R=0.56 m

In this Appendix, the optimization results for the second example are given. The radius of the ATK-ABLE SRTM boom, which is $R = 0.56$ m, is selected, and sizing and pre-stress optimization results are obtained. Figures B.1, B.2, B.3, B.4, B.5, and B.6 show the variations of bending stiffness, bending stiffness-to-mass, torsional stiffness, torsional stiffness-to-mass, mass, and tip deflection, respectively. Additionally, variation of lengths of struts is shown in Figure B.7. The results are also tabulated in Table B.1. The design variables of each optimized case is also given in Table B.2.

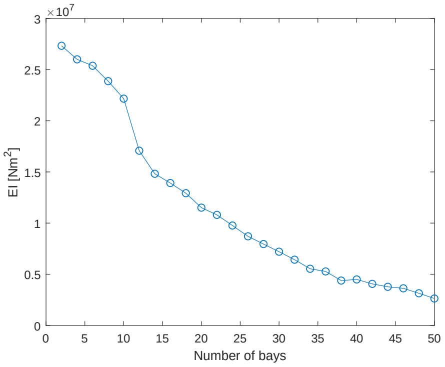

Figure B.1: Variation of bending stiffness

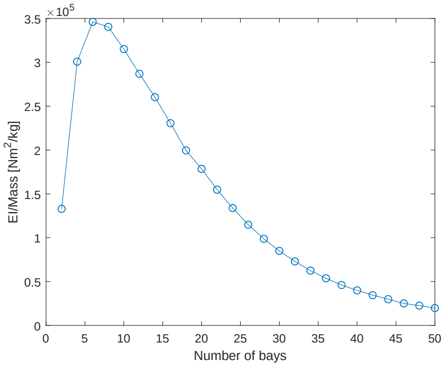

Figure B.2: Variation of bending stiffness per unit mass

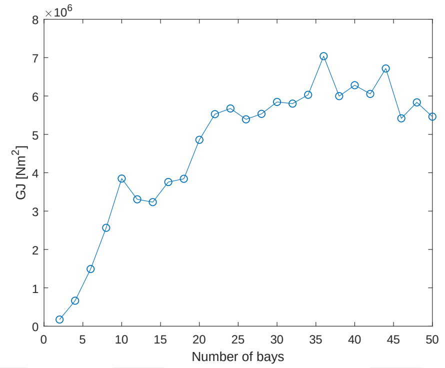

Figure B.3: Variation of torsional stiffness

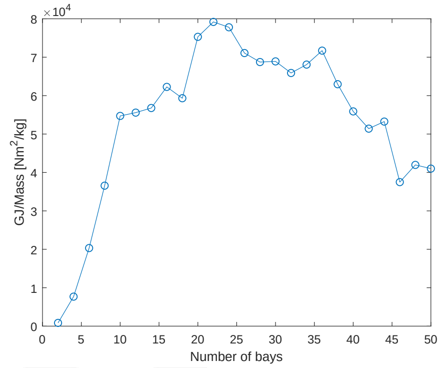

Figure B.4: Variation of torsional stiffness per unit mass

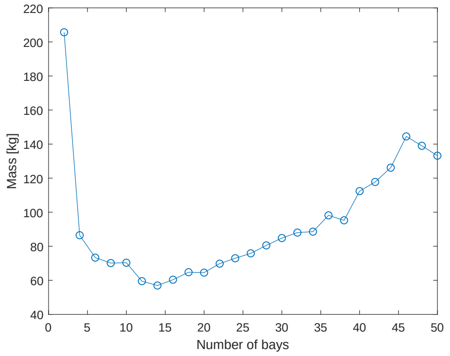

Figure B.5: Variation of mass

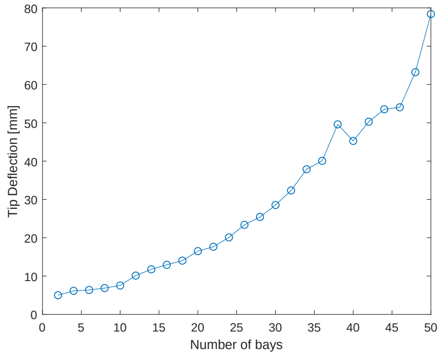

Figure B.6: Variation of tip deflection

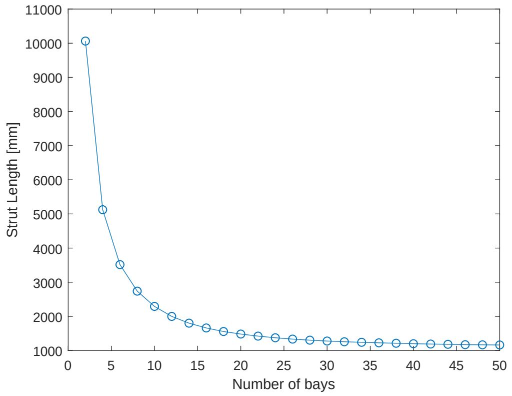

Figure B.7: Variation of length of struts

Table B.1: Bending and torsional stiffnesses of optimized booms

Number of bays	Number of struts	EI [Nm^2]	GJ [Nm^2]	Mass [kg]	EI/Mass	GJ/Mass
2	6	2.73×10^{7}	1.74×10^{5}	205.671	1.33×10^{5}	8.44×10^{2}
4	12	2.60×10^{7}	6.64×10^{5}	86.474	3.01×10^{5}	7.68×10^{3}
6	18	2.54×10^{7}	1.49×10^{6}	73.331	3.46×10^{5}	2.03×10^{4}
8	24	2.39×10^{7}	2.56×10^{6}	70.131	3.40×10^{5}	3.66×10^{4}
10	30	2.22×10^{7}	3.85×10^{6}	70.333	3.15×10^{5}	5.47×10^{4}
12	36	1.71×10^{7}	3.31×10^{6}	59.504	2.87×10^{5}	5.56×10^{4}
14	42	1.48×10^{7}	3.23×10^{6}	56.949	2.60×10^{5}	5.68×10^{4}
16	48	1.39×10^{7}	3.76×10^{6}	60.353	2.31×10^{5}	6.23×10^{4}
18	54	1.29×10^{7}	3.84×10^{6}	64.761	2.00×10^{5}	5.93×10^{4}
20	60	1.15×10^{7}	4.86×10^{6}	64.511	1.78×10^{5}	7.53×10^{4}
22	66	1.08×10^{7}	5.53×10^{6}	69.798	1.55×10^{5}	7.92×10^{4}
24	72	9.76×10^{6}	5.67×10^{6}	72.950	1.34×10^{5}	7.78×10^{4}
26	78	8.71×10^{6}	5.39×10^{6}	75.851	1.15×10^{5}	7.11×10^{4}
28	84	7.95×10^{6}	5.53×10^{6}	80.513	9.88×10^{4}	6.87×10^{4}
30	90	7.20×10^{6}	5.85×10^{6}	84.820	8.49×10^{4}	6.89×10^{4}
32	96	6.42×10^{6}	5.80×10^{5}	88.042	7.30×10^{4}	6.59×10^{4}
34	102	5.54×10^{6}	6.03×10^{6}	88.588	6.25×10^{4}	6.81×10^{4}
36	108	5.27×10^{6}	7.04×10^{6}	98.151	5.37×10^{4}	7.17×10^{4}
38	114	4.38×10^{6}	6.00×10^{6}	95.227	4.60×10^{4}	6.30×10^{4}
40	120	4.49×10^{6}	6.28×10^{6}	112.379	4.00×10^{4}	5.59×10^{4}
42	126	4.06×10^{6}	6.05×10^{6}	117.768	3.45×10^{4}	5.14×10^{4}
44	132	3.77×10^{6}	6.72×10^{6}	126.157	2.99×10^{4}	5.32×10^{4}
46	138	3.63×10^{6}	5.42×10^{6}	144.505	2.51×10^{4}	3.75×10^{4}
48	144	3.14×10^{6}	5.83×10^{6}	139.004	2.26×10^{4}	4.20×10^{4}
50	150	2.63×10^{6}	5.46×10^{6}	133.178	1.98×10^{4}	4.10×10^{4}

Table B.2: Optimized design variables for tensegrity booms

Number of bays	Radius of top and bottom cables [mm]	Radius of vertical cables [mm]	Radius of saddle cables [mm]	Radius of reinforcing cables [mm]	Outer radius of struts [mm]	Inner radius of struts [mm]	Pre-stress Coefficient [N/mm]	Twist Angle [degree]
2	10.000	10.000	5.086	10.000	30.000	21.794	0.057	62.000
4	4.449	9.792	4.710	10.000	30.000	28.481	0.130	62.000
6	5.797	10.000	5.321	10.000	30.000	29.284	0.206	62.000
8	7.129	10.000	5.763	10.000	30.000	29.554	0.277	62.000
10	8.346	10.000	6.170	10.000	30.000	29.679	0.343	62.000
12	10.000	7.457	5.388	10.000	30.000	29.663	0.581	79.486
14	8.703	6.482	5.515	9.999	30.000	29.658	0.834	83.055
16	9.644	6.443	5.646	10.000	30.000	29.624	1.185	84.709
18	9.978	6.085	6.085	10.000	30.000	29.538	1.812	86.492
20	10.000	6.425	6.048	10.000	30.000	29.673	1.435	84.372
22	10.000	6.604	6.523	10.000	30.000	29.659	1.7085	84.799
24	9.983	6.477	6.523	10.000	30.000	29.624	2.095	85.445
26	10.000	6.152	6.382	10.000	30.000	29.558	2.713	86.294
28	9.999	6.108	6.774	10.000	30.000	29.551	2.960	86.378
30	10.000	6.204	7.132	10.000	30.000	29.529	3.305	86.524
32	10.000	6.076	7.018	9.999	30.000	29.546	3.321	86.210
34	10.000	6.093	7.106	9.798	30.000	29.596	3.030	85.377
36	10.000	6.581	7.359	9.993	30.000	29.583	3.225	85.215
38	10.000	5.993	7.092	9.785	30.000	29.576	3.369	85.112
40	10.000	6.246	8.072	10.000	30.000	29.504	4.163	86.199
42	10.000	6.138	8.155	10.000	30.000	29.456	4.748	86.748
44	10.000	6.484	8.743	9.999	30.000	29.495	4.410	85.946
46	10.000	5.938	8.937	10.000	30.000	29.250	6.877	87.521
48	10.000	6.103	8.847	10.000	30.000	29.439	5.133	86.407
50	10.000	5.844	8.389	9.953	30.000	29.495	4.611	85.643

The selected case is a tensegrity boom with 6 bays and the length of struts is 3516.4 mm. The equilibrium surfaces with respect to overlap and height are shown in Figures B.8 and B.9, respectively.

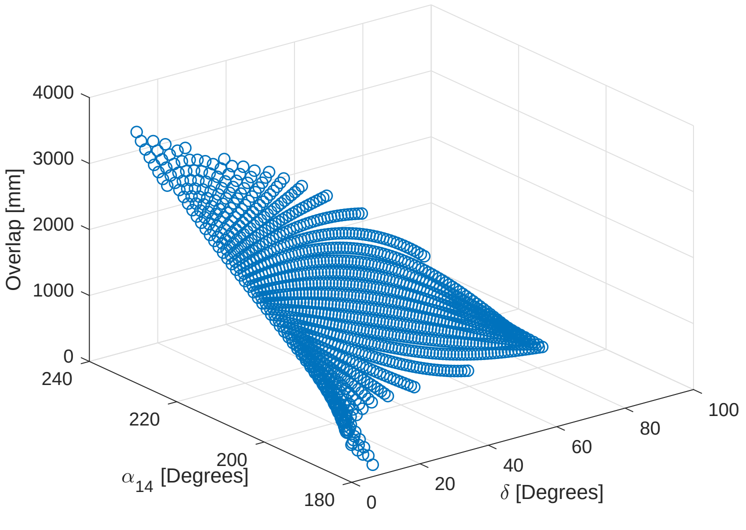

Figure B.8: Equilibrium surface with respect to overlap

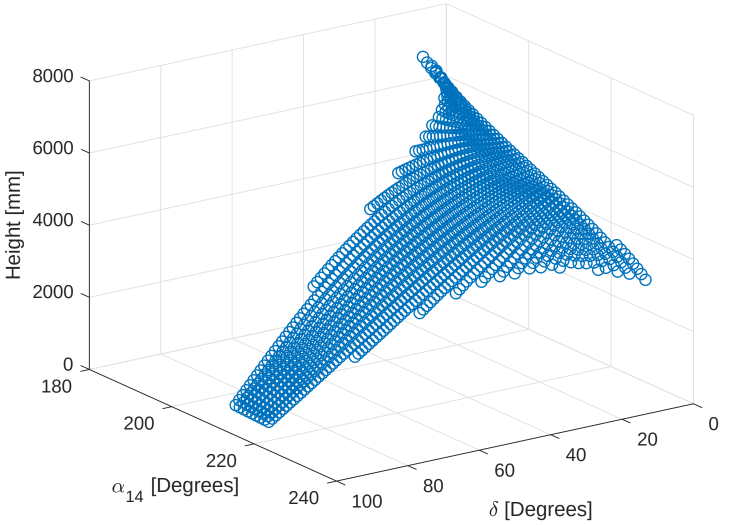

Figure B.9: Equilibrium surface with respect to height

Then, after several deployment simulations, the candidate feasible pairs of azimuth and declination angles are identified. These pairs are shown in Figures B.10 and B.11 with filled green circles.

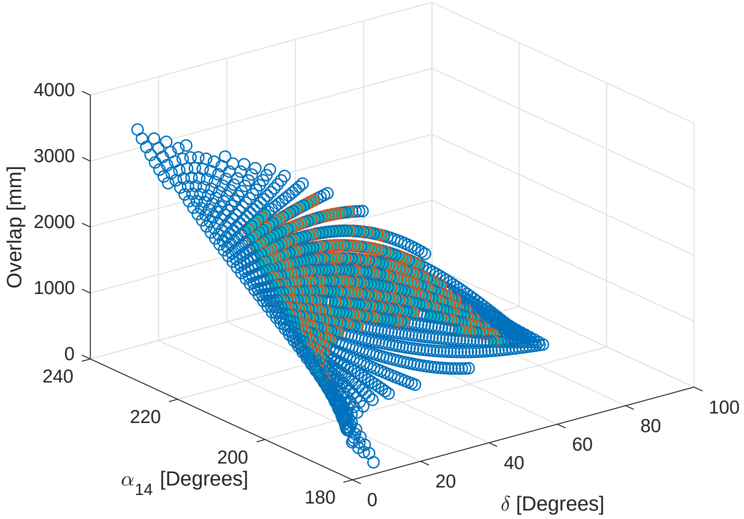

Figure B.10: Feasible points on equilibrium surface with respect to overlap

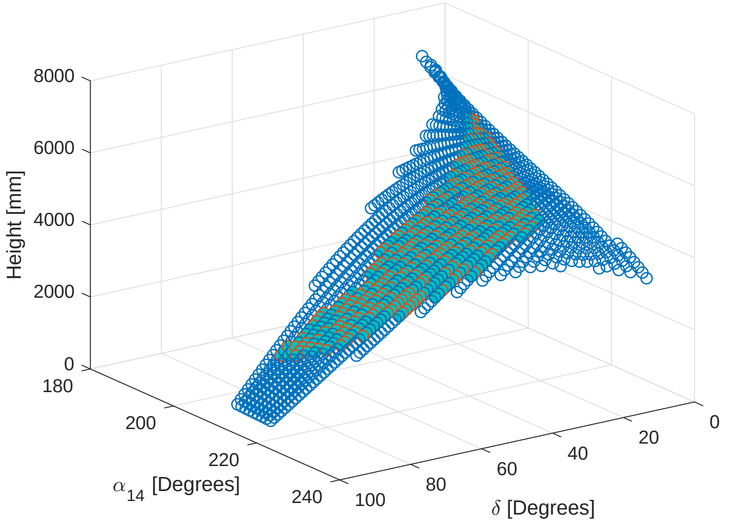

Figure B.11: Feasible points on equilibrium surface with respect to height

After the feasible points are determined for the transformation, effective stiffness properties are evaluated on the equilibrium surface. The equilibrium surfaces with respect to axial, bending, shear, and torsional rigidities are shown in Figures B.12, B.13, B.14, and B.15, respectively.

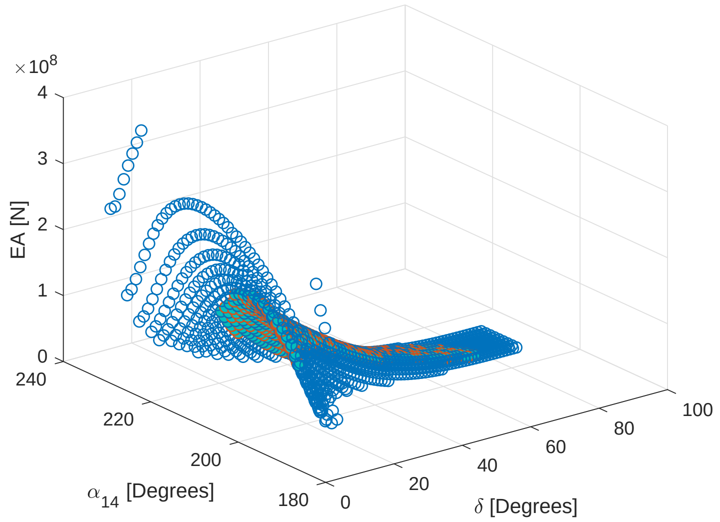

Figure B.12: Equilibrium surface with respect to axial rigidity

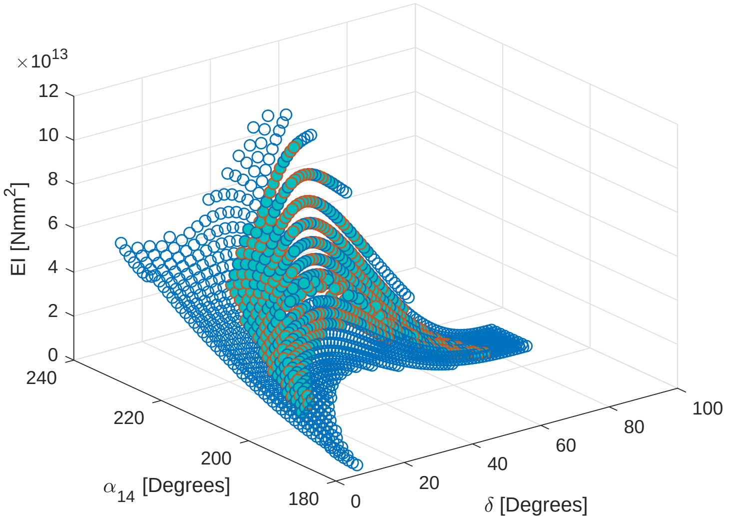

Figure B.13: Equilibrium surface with respect to bending rigidity

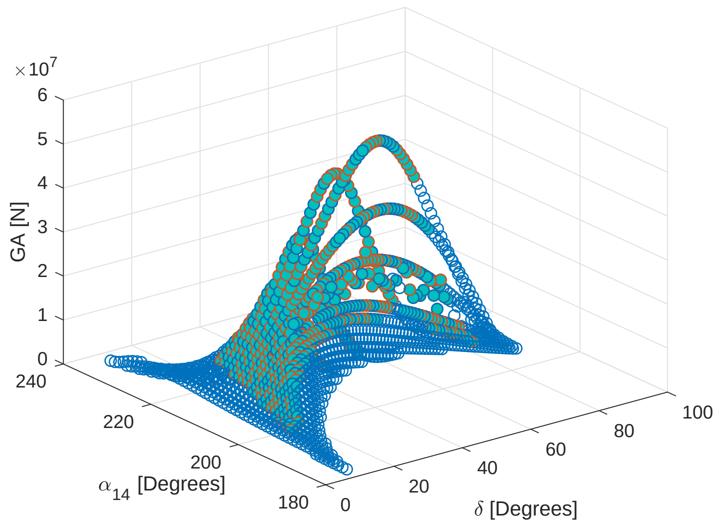

Figure B.14: Equilibrium surface with respect to shear rigidity

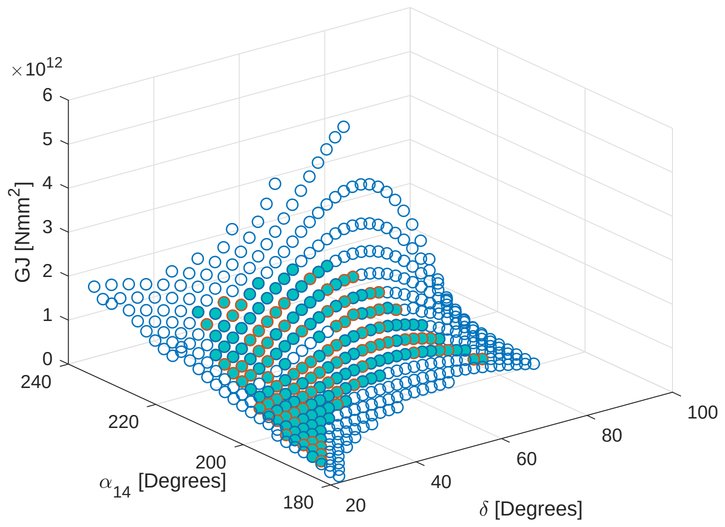

Figure B.15: Equilibrium surface with respect to torsional rigidity

From Figure B.13, the point that yields the maximum bending stiffness without any element collision is identified as $\alpha_{14} = 217°$ and $\delta = 36°$. This point is used to optimize the initial deployment step, and the twist angle, $\alpha = 62°$ obtained from sizing and pre-stress optimization is used to optimize the rotation of the intermediate plane step.

The maximum lengths of the cables are tracked during deployment, and the total mass of the designed boom is calculated. Additionally, starting with the pre-stress coefficient obtained from sizing and pre-stress optimization, the maximum forces in each type of element is also obtained and, based on that information, cross-sectional areas of diagonal cables are determined, considering stress limits for cables. The maximum lengths of the elements, their contribution to the total mass, and the maximum force, and stress they encounter during deployment are given in Table B.3.

Table B.3: Maximum length, force, stress and total mass data

Element Type	Total Number	Maximum Length [mm]	Mass [kg]	Maximum Force [N]	Maximum Stress [MPa]
Top and Bottom Cables	6	969.95	0.885	$1.99{\times}10^2$	1.89
Vertical Cables	18	3377.30	27.501	$7.36{\times}10^2$	2.34
Saddle Cables	15	3083.60	5.925	$3.99{\times}10^2$	4.48
Diagonal Cables	18	3516.40	*	$1.59{\times}10^2$	*
Reinforcing Cables	18	3426.30	27.900	$6.53{\times}10^2$	2.08
Struts	18	3516.40	15.530	$-1.45{\times}10^3$	-10.84

The results show that the mass of the structure, excluding the diagonal cables which are not considered in the final configuration, is 77.741 kg. The minimum possible cross-sectional areas of diagonal cables that yield a stress value lower than the stress limit are selected, their mass contribution is calculated, and the total mass of the structure is obtained as 78.886 kg.

Then bending stiffness-to-mass ratio of the designed tensegrity boom and bending stiffness-to-mass per unit length ratio are found to be $3.22{\times}10^5$ Nm^2/kg and $6.44{\times}10^6$ Nm^3/kg, respectively.

Appendix C

MATLAB Codes

Fundamental MATLAB codes developed for tensegrity deployment simulations, deflection analysis and free vibration problem can be found in the following link:

- http://www.datacommons.psu.edu/commonswizard/MetadataDisplay.aspx?Dataset=6166

The MATLAB codes can be cited using the following DOI number:

- doi:10.18113/D3BH3T

Bibliography

[1] Tibert, G. (2002) *Deployable tensegrity structures for space applications*, Ph.D. thesis, KTH.

[2] Pellegrino, S. (2014) *Deployable structures*, vol. 412, Springer.

[3] ——— (1995) “Large retractable appendages in spacecraft,” *Journal of Spacecraft and Rockets*, **32**(6), pp. 1006–1014.

[4] Mikulas, M. M. (1993) “State-of-the-art and technology needs for large space structures,” *ASME Monograph on Flight-Vehicle Materials, Structures, and Dynamics Technologies*.

[5] Jensen, F. and S. Pellegrino (2001) *Arm development review of existing technologies*, *Tech. rep.*, Cambridge Univ.(United Kingdom). Dept. of Engineering.

[6] Rimrott, F. and G. Fritzsche (2000) “Fundamentals of stem mechanics,” in *IUTAM-IASS Symposium on Deployable Structures: Theory and Applications*, Springer, pp. 321–333.

[7] Mauch, H. R. (1969), “Deployable lattice column,” US Patent 3,486,279.

[8] Buckminster, F. R. (1962), “Tensile-integrity structures,” US Patent 3,063,521.

[9] Emmerich, D. G. (1996) “Emmerich on self-tensioning structures,” *International Journal of Space Structures*, **11**(1-2), pp. 29–36.

[10] Sadao, S. (1996) “Fuller on tensegrity,” *International Journal of Space Structures*, **11**(1-2), pp. 37–42.

[11] Snelson, K. (1996) “Snelson on the tensegrity invention,” *International Journal of Space Structures*, **11**(1-2), pp. 43–48.

[12] “ArtStack,” [Online; accessed 18-June-2018]. URL `https://theartstack.com/artist/kenneth-snelson/early-x-piece-1948`

[13] Motro, R. (2003) *Tensegrity: structural systems for the future*, Elsevier.

[14] Furuya, H. (1992) “Concept of deployable tensegrity structures in space application,” *International Journal of Space Structures*, **7**(2), pp. 143–151.

[15] Hanaor, A. (1993) “Double-layer tensegrity grids as deployable structures,” *International Journal of Space Structures*, **8**(1-2), pp. 135–143.

[16] Sultan, C. and R. T. Skelton (1998) “Tendon control deployment of tensegrity structures,” in *Smart Structures and Materials 1998: Mathematics and Control in Smart Structures*, vol. 3323, International Society for Optics and Photonics, pp. 455–467.

[17] Tibert, G. and S. Pellegrino (2003) “Deployable tensegrity masts,” in *44th AIAA/ASME/ASCE/AHS/ASC Structures, Structural Dynamics, and Materials Conference*, p. 1978.

[18] Pinaud, J.-P., S. Solari, and R. E. Skelton (2004) “Deployment of a class 2 tensegrity boom,” in *Smart Structures and Materials 2004: Smart Structures and Integrated Systems*, vol. 5390, International Society for Optics and Photonics, pp. 155–163.

[19] Murata, S., D. Jodoi, H. Furuya, Y. Terada, and K. Takadama (2005) “Inflatable Tensegrity Module for a Large-Scale Space Structure and its Construction Scinario,” in *The 56th International Astronautical Congress (IAC05)*.

[20] Russell, C. and G. Tibert (2008) “Deployment simulations of inflatable tensegrity structures,” *International Journal of Space Structures*, **23**(2), pp. 63–77.

[21] Skelton, R. E. and M. C. de Oliveira (2009) *Tensegrity systems*, vol. 1, Springer.

[22] Wang, B. (2014) *Free-standing tension structures: from tensegrity systems to cable-strut systems*, CRC Press.

[23] Schek, H.-J. (1974) “The force density method for form finding and computation of general networks,” *Computer methods in applied mechanics and engineering*, **3**(1), pp. 115–134.

[24] Estrada, G. G., H.-J. Bungartz, and C. Mohrdieck (2006) “Numerical form-finding of tensegrity structures,” *International Journal of Solids and Structures*, **43**(22-23), pp. 6855–6868.

[25] Zhang, J. and M. Ohsaki (2006) “Adaptive force density method for form-finding problem of tensegrity structures,” *International Journal of Solids and Structures*, **43**(18-19), pp. 5658–5673.

[26] Tibert, A. and S. Pellegrino (2011) “Review of form-finding methods for tensegrity structures,” *International Journal of Space Structures*, **26**(3), pp. 241–255.

[27] Vassart, N. and R. Motro (1999) “Multiparametered formfinding method: application to tensegrity systems,” *International Journal of Space Structures*, **14**(2), pp. 147–154.

[28] Connelly, R. (2002) “Tensegrity structures: why are they stable?” in *Rigidity theory and applications*, Springer, pp. 47–54.

[29] Tran, H. C. and J. Lee (2010) “Advanced form-finding of tensegrity structures,” *Computers & structures*, **88**(3-4), pp. 237–246.

[30] Calladine, C. (1978) “Buckminster Fuller’s âĂIJtensegrityâĂİ structures and Clerk Maxwell’s rules for the construction of stiff frames,” *International Journal of Solids and Structures*, **14**(2), pp. 161–172.

[31] Pellegrino, S. and C. R. Calladine (1986) “Matrix analysis of statically and kinematically indeterminate frameworks,” *International Journal of Solids and Structures*, **22**(4), pp. 409–428.

[32] Connelly, R. and M. Terrell (1995) “Globally rigid symmetric tensegrities,” *Structural Topology 1995 núm 21.*

[33] Sultan, C., M. Corless, and R. Skelton (1999) “Reduced prestressability conditions for tensegrity structures,” in *40th Structures, Structural Dynamics, and Materials Conference and Exhibit*, p. 1478.

[34] Masic, M., R. E. Skelton, and P. E. Gill (2005) “Algebraic tensegrity form-finding,” *International Journal of Solids and Structures*, **42**(16-17), pp. 4833–4858.

[35] Tran, H. C. and J. Lee (2013) “Form-finding of tensegrity structures using double singular value decomposition,” *Engineering with Computers*, **29**(1), pp. 71–86.

[36] ——— (2010) “Initial self-stress design of tensegrity grid structures,” *Computers & structures*, **88**(9-10), pp. 558–566.

[37] Motro, R. and M. Bounderbala (1996) “Mobile Tensegrity Systems,” *WIT Transactions on The Built Environment*, **24**.

[38] Kebiche, K., M. Kazi-Aoual, and R. Motro (1999) "Geometrical nonlinear analysis of tensegrity systems," *Engineering structures*, **21**(9), pp. 864–876.

[39] Argyris, J. H. and D. W. Scharpf (1972) "Large deflection analysis of prestressed networks," *Journal of the Structural Division*, **98**(3), pp. 633–654.

[40] Motro, R. (1983) *Formes et forces dans les systemes constructifs: cas des systemes réticulés spatiaux autocontraints*, Ph.D. thesis.

[41] Bathe, K.-J., E. Ramm, and E. L. Wilson (1975) "Finite element formulations for large deformation dynamic analysis," *International Journal for Numerical Methods in Engineering*, **9**(2), pp. 353–386.

[42] Tran, H. C. and J. Lee (2011) "Geometric and material nonlinear analysis of tensegrity structures," *Acta Mechanica Sinica*, **27**(6), pp. 938–949.

[43] Nuhoglu, A. and K. A. Korkmaz (2011) "A practical approach for nonlinear analysis of tensegrity systems," *Engineering with Computers*, **27**(4), pp. 337–345.

[44] Faroughi, S. and J. Lee (2014) "Geometrical nonlinear analysis of tensegrity based on a co-rotational method," *Advances in Structural Engineering*, **17**(1), pp. 41–51.

[45] Noor, A. K., M. S. Anderson, and W. H. Greene (1978) "Continuum models for beam-and platelike lattice structures," *AIAA Journal*, **16**(12), pp. 1219–1228.

[46] Noor, A. K. and C. Andersen (1979) "Analysis of beam-like lattice trusses," *Computer Methods in Applied Mechanics and Engineering*, **20**(1), pp. 53–70.

[47] Noor, A. K. and W. C. Russell (1986) "Anisotropic continuum models for beamlike lattice trusses," *Computer methods in applied mechanics and engineering*, **57**(3), pp. 257–277.

[48] Noor, A. K. and M. M. Mikulas (1988) "Continuum modeling of large lattice structures: Status and projections," in *Large Space Structures: Dynamics and Control*, Springer, pp. 1–34.

[49] Dow, J. O., Z. Su, C. Feng, and C. Bodley (1985) "Equivalent continuum representation of structures composed of repeated elements," *AIAA journal*, **23**(10), pp. 1564–1569.

[50] KEBICHE, K., M. K. AOUAL, and R. MOTRO (2008) “Continuum Models for Systems in a Selfstress State,” *International Journal of Space Structures*, **23**(2), pp. 103–115.

[51] LEE, U. (1998) “Equivalent continuum representation of lattice beams: spectral element approach,” *Engineering Structures*, **20**(7), pp. 587–592.

[52] MCCALLEN, D. B. and K. ROMSTAD (1988) “A continuum model for the nonlinear analysis of beam-like lattice structures,” *Computers & structures*, **29**(2), pp. 177–197.

[53] NISHIMURA, Y. (2000) *Static and dynamic analyses of tensegrity structures.*

[54] MURAKAMI, H. (2001) “Static and dynamic analyses of tensegrity structures. Part 1. Nonlinear equations of motion,” *International Journal of Solids and Structures*, **38**(20), pp. 3599–3613.

[55] PRZEMIENIECKI, J. S. (1985) *Theory of matrix structural analysis*, Courier Corporation.

[56] PAZ, M. (2012) *Structural dynamics: theory and computation*, Springer Science & Business Media.

[57] YILDIZ, K. and G. A. LESIEUTRE (2018) “Effective Stiffness Properties of Cylindrical Tensegrity Towers,” in *2018 AIAA Spacecraft Structures Conference*, p. 0692.

[58] SUN, C., B. KIM, and J. BOGDANOFF (1981) “On the derivation of equivalent simple models for beam-and plate-like structures in dynamic analysis,” in *Dynamics Specialists Conference*, p. 624.

[59] KAHLA, N. B. (1995) “Equivalent beam-column analysis of guyed towers,” *Computers & structures*, **55**(4), pp. 631–645.

[60] SKELTON, R. T. and C. SULTAN (1997) “Controllable tensegrity: a new class of smart structures,” in *Smart Structures and Materials 1997: Mathematics and Control in Smart Structures*, vol. 3039, International Society for Optics and Photonics, pp. 166–178.

[61] SULTAN, C. (1999) *Modeling, design, and control of tensegrity structures with applications.*

[62] SULTAN, C. and R. SKELTON (2003) “Deployment of tensegrity structures,” *International Journal of Solids and Structures*, **40**(18), pp. 4637–4657.

[63] Rhode-Barbarigos, L., N. B. H. Ali, R. Motro, and I. F. Smith (2010) "Designing tensegrity modules for pedestrian bridges," *Engineering Structures*, **32**(4), pp. 1158–1167.

[64] Veuve, N., S. D. Safaei, and I. F. Smith (2015) "Deployment of a tensegrity footbridge," *Journal of Structural Engineering*, **141**(11), p. 04015021.

[65] ——— (2016) "Active control for mid-span connection of a deployable tensegrity footbridge," *Engineering Structures*, **112**, pp. 245–255.

[66] Sultan, C., M. Corless, and R. E. Skelton (2001) "The prestressability problem of tensegrity structures: some analytical solutions," *International Journal of Solids and Structures*, **38**(30-31), pp. 5223–5252.

[67] Masic, M., R. E. Skelton, and P. E. Gill (2006) "Optimization of tensegrity structures," *International Journal of Solids and Structures*, **43**(16), pp. 4687–4703.

[68] De Jager, B. and R. E. Skelton (2004) "Symbolic stiffness optimization of planar tensegrity structures," *Journal of intelligent material systems and structures*, **15**(3), pp. 181–193.

[69] Masic, M. and R. E. Skelton (2006) "Selection of prestress for optimal dynamic/control performance of tensegrity structures," *International Journal of Solids and Structures*, **43**(7-8), pp. 2110–2125.

[70] Raja, M. G. and S. Narayanan (2009) "Simultaneous optimization of structure and control of smart tensegrity structures," *Journal of Intelligent Material Systems and Structures*, **20**(1), pp. 109–117.

[71] Ali, N. B. H., L. Rhode-Barbarigos, A. A. P. Albi, and I. F. Smith (2010) "Design optimization and dynamic analysis of a tensegrity-based footbridge," *Engineering Structures*, **32**(11), pp. 3650–3659.

[72] Dalilsafaei, S., A. Eriksson, and G. Tibert (2012) "Improving bending stiffness of tensegrity booms," *International Journal of Space Structures*, **27**(2-3), pp. 117–129.

[73] Kanno, Y. (2012) "Topology optimization of tensegrity structures under self-weight loads," *Journal of the Operations Research Society of Japan*, **55**(2), pp. 125–145.

[74] ——— (2013) "Topology optimization of tensegrity structures under compliance constraint: a mixed integer linear programming approach," *Optimization and Engineering*, **14**(1), pp. 61–96.

[75] Marzari, Q. (2014) *Optimization of tensegrity structures*, Master's thesis, Massachusetts Institute of Technology.

[76] Xu, X., Y. Wang, and Y. Luo (2018) "An improved multi-objective topology optimization approach for tensegrity structures," *Advances in Structural Engineering*, **21**(1), pp. 59–70.

[77] Li, Q., R. E. Skelton, and J. Yan (2011) "Energy optimization of deployable tensegrity structure," in *Control Conference (CCC), 2011 30th Chinese*, IEEE, pp. 2146–2151.

[78] Caluwaerts, K. and J. P. Carbajal (2015) "Energy conserving constant shape optimization of tensegrity structures," *International Journal of Solids and Structures*, **58**, pp. 117–127.

[79] Eberhart, R. and J. Kennedy (1995) "A new optimizer using particle swarm theory," in *Micro Machine and Human Science, 1995. MHS'95., Proceedings of the Sixth International Symposium on*, IEEE, pp. 39–43.

[80] Eberhart, R. C. and X. Hu (1999) "Human tremor analysis using particle swarm optimization," in *Evolutionary Computation, 1999. CEC 99. Proceedings of the 1999 Congress on*, vol. 3, IEEE, pp. 1927–1930.

[81] Tandon, V. (2000) "Closing the gap between CAD/CAM and optimized CNC end milling," *Master thesis, Purdue School of Engineering and Technology, Indiana University Purdue University Indianapolis.*

[82] Fukuyama, Y. and Y. Nakanishi (1999) "A particle swarm optimization for reactive power and voltage control considering voltage stability," in *Proc. 11th IEEE Int. Conf. Intell. Syst. Appl. Power Syst*, pp. 117–121.

[83] Eberhart, R., P. Simpson, and R. Dobbins (1996) *Computational intelligence PC tools*, Academic Press Professional, Inc.

[84] Poli, R. (2008) "Analysis of the publications on the applications of particle swarm optimisation," *Journal of Artificial Evolution and Applications*, **2008**.

[85] Dorigo, M. and M. Birattari (2011) "Ant colony optimization," in *Encyclopedia of machine learning*, Springer, pp. 36–39.

[86] Karaboga, D. and B. Basturk (2007) "A powerful and efficient algorithm for numerical function optimization: artificial bee colony (ABC) algorithm," *Journal of global optimization*, **39**(3), pp. 459–471.

[87] Shi, Y. and R. Eberhart (1998) "A modified particle swarm optimizer," in *Evolutionary Computation Proceedings, 1998. IEEE World Congress on Computational Intelligence., The 1998 IEEE International Conference on*, IEEE, pp. 69–73.

[88] Eberhart, R. C. and Y. Shi (2000) "Comparing inertia weights and constriction factors in particle swarm optimization," in *Evolutionary Computation, 2000. Proceedings of the 2000 Congress on*, vol. 1, IEEE, pp. 84–88.

[89] Hadidi, A., S. K. Azad, and S. K. Azad (2010) "Structural optimization using artificial bee colony algorithm," .

[90] Hasancebi, O., S. Kazemzadeh Azad, and S. Kazemzadeh Azad (2013) "Automated Sizing of Truss Structures Using a Computationally Improved SOPT Algorithm," **3**, pp. 209–221.

[91] Murphey, T., Booms, and Trusses (2006) "Recent advances in gossamer spacecraft (Progress in Astronautics and Aeronautics)," *AIAA*, **212**.

[92] "Northrop Grumman AstroMast," [Online; accessed 11-May-2018]. URL `http://www.northropgrumman.com/BusinessVentures/AstroAerospace/Products/Pages/AstroMast.aspx`

[93] Garrett, H. B. and C. P. Pike (1980) *Space systems and their interactions with Earth's space environment*, vol. 71, American Institute of Aeronautics and Astronautics.

[94] Greschik, G. (2007) "Global Imperfection-Based Column Stability Analysis," in *48th AIAA/ASME/ASCE/AHS/ASC Structures, Structural Dynamics, and Materials Conference*, p. 2225.

[95] Kravitz, S. (1967) "Packing cylinders into cylindrical containers," *Mathematics magazine*, **40**(2), pp. 65–71.

[96] Reis, G. E. (1975) "Dense packing of equal circles within a circle," *Mathematics Magazine*, **48**(1), pp. 33–37.

[97] Graham, R. L., B. D. Lubachevsky, K. J. Nurmela, and P. R. Östergård (1998) "Dense packings of congruent circles in a circle," *Discrete Mathematics*, **181**(1-3), pp. 139–154.

[98] Lubachevsky, B. D. and R. L. Graham (1997) "Curved hexagonal packings of equal disks in a circle," *Discrete & Computational Geometry*, **18**(2), pp. 179–194.

[99] Grosso, A., A. Jamali, M. Locatelli, and F. Schoen (2010) "Solving the problem of packing equal and unequal circles in a circular container," *Journal of Global Optimization*, **47**(1), pp. 63–81.

[100] Eckard Specht (2014), "The best known packings of equal circles in a circle," [Online; accessed 11-May-2018].
URL `http://hydra.nat.uni-magdeburg.de/packing/cci/cci.html`

Vita

Kaan Yildiz

Kaan Yildiz was born in 1991, in Istanbul, Turkey. He received his Bachelor's degree in Aeronautical Engineering from Istanbul Technical University in 2013. He continued his studies at Istanbul Technical University and attained his Master's degree in Aeronautical and Astronautical Engineering in 2015. In 2015, he started his Ph.D. degree in The Pennsylvania State University Aerospace Engineering Department under the supervision of Dr. George A. Lesieutre and completed in 2018. His research interests are in the areas of tensegrity structures, active vibration control and spacecraft structures.